Hamidreza Zarei

Experimental and numerical investigation of crash structures using aluminum alloys

Cuvillier Verlag Göttingen

Experimental and numerical investigation of crash structures using aluminum alloys

Von der Fakultät für Maschinenbau

der Gottfried Wilhelm Leibniz Universität Hannover

zur Erlangung des akademischen Grades

Doktor-Ingenieur

genehmigte

Dissertation

von

M.Sc. Hamidreza Zarei

geboren am 28.01.1976 in Shahre Rey

2008

Bibliografische Information der Deutschen Nationalbibliothek
Die Deutsche Nationalbibliothek verzeichnet diese Publikation in der Deutschen Nationalbibliografie; detaillierte bibliografische Daten sind im Internet über http://dnb.ddb.de abrufbar.
1. Aufl. - Göttingen : Cuvillier, 2008
Zugl.: Hannover, Univ., Diss., 2008

978-3-86727-542-2

Hauptreferent: Prof. Dr.-Ing. Jörg Wallaschek

Korreferent: Prof. Dr.-Ing. Bernd-Arno Behrens

Vorsitzender: Prof. Dr.-Ing Gerhard Poll

Tag der Promotion: 20.02.2008

© CUVILLIER VERLAG, Göttingen 2008
Nonnenstieg 8, 37075 Göttingen
Telefon: 0551-54724-0
Telefax: 0551-54724-21
www.cuvillier.de

Alle Rechte vorbehalten. Ohne ausdrückliche Genehmigung des Verlages ist es nicht gestattet, das Buch oder Teile daraus auf fotomechanischem Weg (Fotokopie, Mikrokopie) zu vervielfältigen.
1. Auflage, 2008
Gedruckt auf säurefreiem Papier

978-3-86727-542-2

Acknowledgments

The present work has been raised during my occupation as a research assistant at the Institute of Dynamics and Vibrations Research of the Leibniz University of Hanover.

My special thanks to Prof. Dr.-Ing. Karl Popp who was very interested in my research work and accompanied and promoted me in every respect. He passed away after severe diseases in April 2005.

For the opportunity for scientific work, for his technical and personal support and his interest on this issue is my special thanks to my supervisor, Prof. Dr.-Ing. J. Wallaschek.

I would like to thank my second examiner Prof. Dr.-Ing. Bernd-Arno Behrens and the chairman of the exam's committee Prof. Dr.-Ing Gerhard Poll for their interest in my thesis.

I would like to acknowledge the advice and help given by Dr. Matthias Kröger. Without his sense of collaboration and enthusiasm, this study would not have been possible.

I would like to acknowledge the Iranian Ministry of Science, Research and Technology for their financial support for my life and study in Germany.

Special thanks to my industry partner Dr. Henrik Albertsen and the staff of the Jacob Composite GmbH for their good cooperation and suggestions and also for providing the composite crash boxes for me.

I would like to thank the institute's workshop, specially Mr. Jürgen Anton, for the good cooperation. Also my thanks to all my colleagues for the very good working climate at the institute and their suggestions and discussions. Especially, I would like to thank Mrs. Crohn for her administrative skills and helps. I should also thank Mr. Wolfgang Baldermann for his friendly helps in several situations. He helped me to learn the German language permanently.

My thanks to my family, my mother and grandmother, for their support both direct and indirect over the 4 years of this PhD and earlier.

My very special thanks to my wife Mahin, for her understanding and encouragement during my research activity. It is in her memory that this work is dedicated.

Hamidreza Zarei Hannover, February 2005

Contents

Symbols

The following symbols are used in the text.

Latin Notation

A_H	Cross sectional area of the honeycomb cell
A_{iN}	Parameters of non-axisymetric lobe
A_0	Overall area of the section
A_S	Tributary area of the basic folding element
a	Large side of the rectangular tube
a_c	Occupant chest acceleration
a_i	Accelerations of the vehicle in the different crush phases
a_h	Occupant head acceleration
a_x	Occupant body acceleration
b	Small side of the rectangular tube
C	Rectangular tube parameter
C_{avg}	Foam interaction constant
CM	Crush mode
C_{fi}, C^*_{f1}	Foam material constants
C_i	Tube material constant
CSI	Chest severity index
CSI_0	Critical chest severity index
D_i	Anisotropic damage function
D_H	Minor diameter of the honeycomb cell
D_{max}	Maximum crush distance
D_0	Critical crush distance
d	Width of square tube / diameter of circular tube
d_e	Effective tube width
d_f	Foam width
d_H	Width of the honeycomb cell wall
E	Energy absorption
E_a	Young's modulus in the fiber direction
E_b	Young's modulus in the matrix direction
E_f	Young's modulus of the foam density
E_{goal}	Target energy absorption
E_{ii}	Young's modulus of the honeycomb
E_s	Young's modulus of the base material
E_t	Young's modulus of the tube material
e_c	Compressive fiber failure parameter
e_d	Compressive matrix failure parameter
e_f	Tensile fiber failure parameter

e_m	Tensile matrix failure parameter
$f(X)$	Optimization function
$f(x)$	Fitness of chromosome
G_{ii}	Shear modulus of the honeycomb
$g(x)$	Inequality optimization constraint
H	Half plastic wavelength
HIC	Head injury criterion
HIC_0	Critical head injury criterion
$h(x)$	Equality optimization constraint
K_1	Buckling coefficient
k	Number of design variables
l	Tube length
l_f	Effective filling length
L_H	Ribbon direction of the honeycomb
M	Vehicle mass
M_f	Ultimate bending moment of the foam-filled section
M_{max}	Maximum bending moment
M_0	Full Plastic bending moment
M_p	Plastic moment
M_u	Bending moment of the empty beam
M_{uf}	Bending moment of the filled beam
m	Number of optimization object
m_s	Eccentricity factor
N	Number of the experimental points
N_d	Number of non-symmetric lobes
N_l	Number of layers
N_p	Number of experimental points in factorial design method
N_q	Number of experimental points in D-optimality design method
N_s	Number of symmetric lobes
NVH	Noise vibration and harshness
n	Number of half-sine waves along the tube length
n_c	Number of chromosomes
n_d	Number of design variables
P	Number of inequality optimization constraints
P_{chest}	Occupant’s chest probability of severe injury
P_{head}	Occupant’s head probability of severe injury
P_m	Mean crush load
P_{ma}	Allowable mean crush load
P_{max}	Maximum crush load
P_{total}	Total occupant probability of severe injury

$P(\delta)$	Instantaneous load
P_{60}	Mean crush load at 60 mm crush displacement
q	Number of equality optimization constraints
R	Radius of the circular tube
RSM	Response surface method
r	Impactor radius
S_c	Shear strength
S_E	Stroke efficiency
SEA	Specific energy absorption
S_{max}	Final crush displacement
T	Total duration of the impact load
t	Tube thickness
t_f	Thickness of the foam cell wall
t_i	Different point of time in the crush process
t_H	Thickness of the honeycomb cell wall
V	Impact velocity
V_H	Relative volume of honeycomb
V_{HD}	Relative volume of honeycomb at full densification
v_p	Plastic coefficient of contraction
W	Tube imperfection
W_H	Transverse direction of the honeycomb
W_i	Weight facture
W_0	Amplitude of the tube imperfection
X_c	Compressive strength in the fiber direction
X_t	Tensile strength in the fiber direction
x_i	Optimization parameters
Y	Yield strength
Y_c	Compressive strength in the matrix direction
Y_t	Tensile strength in the matrix direction
y_i	Surface approximation

Greek symbols

α_f	Defines the shape of the foam yield surface
α_2	Foam material parameter
β	Foam material parameter
β_i	Response surface constant
β_H	Honeycomb material parameter
δ	Instantaneous shortening of the tube
$\hat{\varepsilon}$	Equivalent strain
ε_{cr}	Critical strain

ε_D	Densification strain
ε_i	Bias and random errors
ε_{ij}	Principal shell strains
ε_p	Plastic strain
$\varepsilon^p_{failure}$	Tensional fracture strain
$\varepsilon^p_{rupture\ e}$	Rupture strain
η	Crush load efficiency
η_e	Structural effectiveness
η_f	Bending moment ratio
θ	Impact angle
θ_c	Critical bending rotation angle
θ_{cf}	Critical bending rotation angle of the foam-filled section
μ	Coefficient of friction
υ	Poisson's ratio
υ_{ab}	In plane Poisson's ratio
ρ_f	Foam density
ρ_s	Density of the base material
$\hat{\sigma}$	Equivalent stress
σ_{cr}	Critical stress
σ_e	Effective von Mises stress
σ_f	Plastic collapse strength of the foam
σ_{fail}	Tensile strength of the adhesive material
σ_h	Plastic collapse strength of the honeycomb
σ_{ij}	Principal shell stresses
σ_m	Mean stress
σ_n	Normal stress
σ_0	Flow stress of aluminum material
σ_{0f}	Flow stress of foam material
σ_{0h}	Flow stress of honeycomb material
σ_p	Plateau stress
σ_s	Shear stress
σ_u	Ultimate stress
σ_v	Viscous stress of the aluminum material
σ_{ys}	Yield stress of the base material
$\sigma_{0.2}$	Proportional limit
τ_{fail}	Shear strength of the adhesive material
Φ	Relative density
Φ_f	Volume fraction of the solid in the foam cell edges
φ	Foam yield function
ω	Damage variable

Abstract

Concerns have been raised for many years about the quality and safety of the vehicles as well as their contribution to the air pollution that endangers public health. Several vehicle safety standards have been developed for different crash scenarios. To improve air quality and reduce vehicle's emissions, there are high interests to amend vehicle fuel consumption through producing light weight vehicles. These improvements should not menace vehicle safety. Vehicle designers achieve safety and fuel economy advances through using lightweight materials like aluminum alloys, high strength steels, tailored beams and composite materials in the vehicle's structures.

In this research, finite element crash simulation of a vehicle model is considered to characterize the energy absorption capacity of the vehicle's frontal structure. Crashworthiness optimization technique is implemented to reduce the weight of selected frontal elements while vehicle safety performance is improved. Crush performance of the two most effective vehicle's frontal crash elements, namely, crash box and bumper beam is investigated by a comprehensive experimental and numerical study in axial, oblique and bending crush conditions. The energy absorption mechanisms of these elements are characterized briefly and multi design optimization *MDO* technique is implemented to maximize their energy absorptions and reduce their weights.

The crush behavior of low density materials like aluminum honeycomb and foam is studied. The concept of filling crash box and bumper beam with these materials is investigated experimentally and numerically. The same *MDO* procedure which is used for empty aluminum crash box is implemented to maximize the energy absorption capacities of the filled structures and minimizing their weights.

Experimental and numerical research is performed to investigate the crush behavior of thermoplastic composite crash boxes. The energy absorption mechanisms of composite materials and its differences to aluminum alloys are studied. The effort is conducted to characterize the energy absorption of the foam-filled composite crash box. The *MDO* procedure is used to maximize energy absorption capacity of the composite crash box and minimize its weight. Finally the optimum composite crash box is compared with the optimum aluminum crash box. In the above mentioned optimization procedures, practical and safety requirements are considered as optimization constraints.

The theoretical methods of predicting the crush behavior of empty and filled crash box and bumper beam are sammaried. The experimental results are used to calibrate these formulations. The calibrated expressions can be used in the primary phase of the vehicle's structural design.

Keywords: vehicle crash structure, energy absorption, optimization, crash efficiency

Zusammenfassung

Der Zielkonflikt bei der Entwicklung von Leichtbaukonzepten besteht in der möglichst weitgehenden Reduktion des Gewichtes bei gleichzeitiger Einhaltung einschlägiger Sicherheitsstandards, die für verschiedene Crash-Szenarien definiert wurden. Die Entwicklung und Validierung von Modellen zur Simulation des Crash-Verhaltens von Fahrzeug Crashstrukturen ist dabei eine wichtige Aufgabe.

Die vorliegende Arbeit beschäftigt sich mit einer Crashsimulation von Fahrzeugen mit Hilfe der Finiten Elemente Methode, in dem die effektivsten Absorberelemente der Fahrzeugfrontalstruktur bestimmt werden. Mit Hilfe einer Optimierungstechnik wird eine Gewichtsreduzierung ausgewählter Crashelemente im Vorderwagen bei gleichzeitiger Verbesserung der Fahrzeugsicherheit erreicht. Die Gefährdung der Insassen während der Kollission wird durch zwei wesentliche Kriterien beschrieben: das Kopfverletzungskriterium *HIC*, mit dem die auf den Kopf einwirkende Beschleunigung, und der Brust Gefährdungsindex *CSI*, mit dem die auf den Brustraum einwirkende Beschleunigung erfasst wird. Die neun Crashelemente der Vorderwagenstruktur, die den größten Einfluss auf die Fahrzeugsenergieabsorption haben, wurden ermittelt. Die Optimierungstechnik wurde zur Verringerung des Gewichts der ausgewählten Elemente genutzt bei gleichzeitiger Verbesserung des Kopfverletzungskriteriums, *HIC*, und des Brust Gefährdungsindexes, *CSI,* und Reduzierung der maximalen Verformung D_{max}. Die Ergebnisse zeigen, dass nach mehreren Optimierungsschritten die gesamten Masse der Komponenten sich um ca. 9% verringert, während die Fahrzeugsicherheit verbessert wird.

Die Wirkung der beiden effektivsten Fahrzeug-Frontalcrashelemente, Crashbox und Stoßstangenquerträger werden durch experimentelle und numerische Studien bei axialen sowie schrägen Belastungen und unter Biegung untersucht. Die Mehrgrößen-Optimierunsgtechnik, *MDO,* wird zur Maximierung der Energieabsorption bei gleichzeitiger Gewichtsreduktion eingesetzt.

Das Crashverhalten von Materialen mit geringer Dichte, wie Aluminiumwaben und Schäume werden untersucht. Das Konzept, die Crashbox und den Stoßstangenquerträger mit diesen Materialien auszufüllen, wird numerisch und experimentell untersucht. Das gleiche *MDO* Verfahren, das auch für leere Aluminium Crashboxen angewendet wurde, wird verwendet, um die Energieabsorbierung der gefüllten Strukturen bei einer gleichzeitigen Gewichtsreduktion zu maximieren. Das Ergebnis der Crashbox Optimierung zeigt, dass eine mit Schaum gefüllte Crashbox bei gleicher Energieaufnahme, wie die optimale leere Crashbox, mehr als 19 Prozent weniger Gewicht besitzt. Die gleiche Optimierung des Stoßstangenquerträgers zeigt, dass der optimal gefüllte Stoßfängerstangenquerträger bei gleicher Energieaufnahme, wie der optimale leere Stoßstangenquerträger, mehr als 28 Prozent weniger Gewicht hat.

Experimentelle und numerische Untersuchungen werden durchgeführt um das Crashverhalten von Crashboxen, die aus thermoplastischen Verbundstoffen aufgebaut sind, zu erforschen. Die Mechanismen der Energieabsorption von Verbundwerkstoffen und Aluminiumlegierungen werden verglichen. Hier wird die Energieaufnahme der mit Schaum gefüllten Crashboxen aus Verbundwerkstoffen charakterisiert. Ebenfalls wird mit Hilfe des *MDO*-Verfahrens die Energieaufnahme der Verbundwerkstoff Crashboxen maximiert bei gleichzeitiger Reduzierung des Gewichts. Abschließend werden die optimierten Verbundwerkstoff- und Aluminium-Crashboxen verglichen. Als Ergebnis zeigte sich, dass die optimale Verbundwerkstoff Crashbox rund 17 Prozent mehr Energie als die Aluminium-Crashbox absorbiert, während sie rund 27 Prozent weniger Gewicht hat.

Verschiedene analytische Methoden zur Vorhersage des Crashverhaltens der leeren und gefüllten Crashboxen, sowie des Stoßstangenquerträgers werden bewertet. Die experimentellen Ergebnisse werden hierzu herangezogen. Die in dieser Arbeit erarbeiteten Ergebnisse sind besonders für konzeptionelle Arbeiten in der ersten Entwurfsphase von (großer) Bedeutung.

Schlagwoete: Fahrzeug-Crashstruktur, Energyabsorption, Optimierung, Crasheffizienz

1. Introduction

Despite all improvements in vehicle crashworthiness, official information shows that the total number of road fatalities in the EU countries is more than 41000 each year. The lowest and highest values are corresponded to Malta and Latvia, 4 and 22 per 100000 inhabitants, respectively. Denmark has the lowest non-fatal road accidents and the highest value is in the Slovenia [107]. The information also indicates that from different types of road users, about 45% of the fatal accidents are caused by the vehicles; see Figure 1.1 [48].

Generally, for the purpose of vehicle body design, safety experts classify vehicle collisions as frontal, side, rear and rollover crashes. Based on the statistical investigations, the frontal impact followed by side impact are the two most frequent causes for fatalities [76]; see Figure 1.2 left. In the frontal impact, the vehicle frontal structure should absorb most of the crash energy by plastic deformation and prevent intrusion into the occupant compartment, especially in the case of offset crashes and collisions with narrow objects such as trees. Figure 1.2 right shows the probabilities of impact directions in the frontal collisions. Here, it can be seen that the collisions angle α is mostly less than 15 degree.

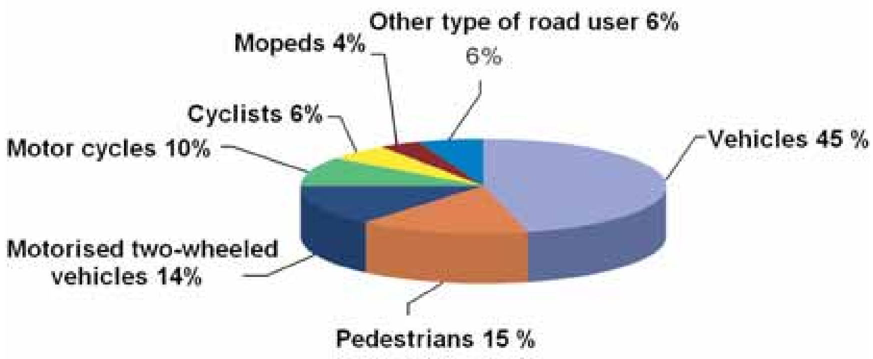

Figure 1.1: Percentage of accidents by different types of road users

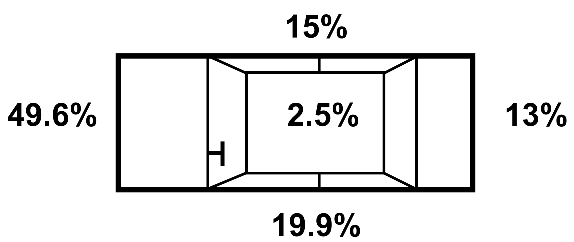

$0° < \alpha < 15°$	64%
$15° < \alpha < 45°$	32%
$45° < \alpha < 90°$	4%

Figure 1.2: Probability of the different accidents scenarios (left), percentage of the impact angle in the case of frontal collisions (right)

The four parameters; traveling needs, quality of vehicles and roads, trauma care and finally human behavior can influence the traffic safety. Despite the fact that the four mentioned parameters are important, but special efforts have been done to improve the quality of vehicles and roads in the last decades. There are two fundamentally different approaches for safety evaluation of the vehicles. The first one uses the accident statistics to determine the occupant protection capacity. A vehicle type related data base which links injuries to the crash specifications indicates weak spots in a design. Since several years are needed to collect a representative amount of accident data, design improvements can only be applied to the later vehicle versions. To overcome this problem, a new approach namely predictive design is used. This method is based on accident standard tests under well defined circumstances. The collision tests spectrums are representative for the real situation on the road. Also it should consider several parameters like: the occupant's biomechanics, the impact location, speed and direction and the crash opponent.

Assessment of vehicle structural crashworthiness performance is originated in the United States of America before World War II. During the 1950's similar investigations started in Europe. The ultimate goal of these researches in both the USA and Europe was, to develop a test procedure that ensures occupant's safety in their own vehicles as well as those in partner vehicles in the event of a collision. These, however, should not ignore the significant number of real life collisions involving single vehicles striking objects such as trees, bridge abutments, roadside structures and buildings.

Today, as a result of more than 50 years investigations for vehicle's safety, several government mandated safety requirements must be fulfilled for different collision scenarios by the vehicles before coming to the market. Safety engineers must run barrier test to ensure vehicle structural integrity and compliance with regulations. In a typical full scale barrier test, a guided vehicle is driven into a barrier at a predetermined initial velocity. For example, based on the United States Federal Motors Vehicle Safety Standard FMVSS 208 a fully instrumented vehicle with numerous load cells, accelerometers and instrumented dummy (or dummies) in the driver (and passenger) seat(s) must impact a rigid barrier at zero degrees, as well as plus 30 degrees and minus 30 degrees, respectively, from an initial velocity of 48.2 km/h (30 mph). Several load cells in the barrier face monitor the impact data history. The unrestrained dummies in the driver and right front passenger must score injury assessment values below those established for human injury thresholds for the head, chest, and legs, for compliance with FMVSS 208. In 1979, the USA National Highway Traffic Safety Administration NHTSA started the New Car Assessment Program NCAP, where cars are tested in frontal impact at the higher impact speed of 56.3 km/h (35 mph). Much later, an NCAP program was started in Australia and one was being developed for Japan. In this test procedure, in addition to the supplemental restraint air bag, the dummy has to be restrained by three-point lap/shoulder belt system. These test procedures which include vehicle impact into a rigid barrier provide a method to assess the effectiveness of the restraint system, as it typically subjects the structure to high deceleration loads.

The European New Car Assessment Program Euro-NCAP is established in 1997 and now backed by five European Governments, the European Commission and motoring and consumer organizations in every EU country. In Germany the German motor club, (Allgemeiner Deutscher Automobil-Club, ADAC) supports this procedure. Based on this test program, the vehicle is impacted on deformable barrier with 40% overlap and velocity of 64 km/h (40 mph). Frontal offset impact with 40 to 50 percent overlap procedure is another type of testing which evaluates the structural integrity of the vehicle in the frontal offset impact condition. The impact target may be rigid or deformable. More deformations and intrusion and relatively less severe deceleration than full frontal impact are seen in this type of tests.

The FMVSS 208 is most effective in preventing head, femur and chest injuries and fatalities. However, it does not directly address lower limb and neck injuries and it does not produce the vehicle intrusion observed in many real life crashes. The EU directive 96/79 EC introduces frontal impact test requirements, including biomechanical criteria, to ensure a high level of protection in the event of a frontal impact. This Directive has additional test dummy injury response criteria, namely, head performance, neck injury, neck bending moment, thorax compression, femur force, tibia compression and movement of sliding knee joints. A fully equipped vehicle with hybrid III dummies which are installed in the each seats, is impacted on a deformable barrier with the velocity of 56.3 km/h (35 mph) and 40% overlap. The orientation of the barrier is such that the first contact of the vehicle with the barrier is on the steering-column side, where there is a choice between carrying out the test with a right-hand or left-hand drive vehicle.

There are similar full-scale tests for side impact. Based on the FMVSS 214 a deformable barrier of a particular mass and stiffness is thrust into the left or right side of the vehicle from some initial speed and certain angle. In this test, side impact dummies (“SID” for the USA and “EURO SID1” for Europe) are used in the driver and outboard rear seat locations. In order to assess the integrity of the fuel tank, the full-scale tests are conducted on the vehicle rear structure either by a deformable barrier or by a bullet car. To evaluate roof strength according to FMVSS 216, engineers apply a quasi-static load on the “greenhouse” and ensure that the roof deformation falls below a certain level for the applied load. A general summary of the current test requirements in the USA is given in Table 1.1 and for the European Union in Table 1.2. Also additional more severely requirements of the USA National Highway Traffic Safety Administration NHTSA’s and New Car Assessment Program NCAP are mentioned.

Increasing vehicle use contributes to air pollution that endangers public health. The reduction of the vehicle weight will improve the vehicle fuel efficiency. Vehicle designers achieve safety and fuel economy advances through using lightweight materials like aluminum, high strength steels, tailored beams and composite materials in the vehicle structures. It is obvious that the vehicle weight reduction must not menace vehicle safety. Normally crashworthiness optimization methods are used more and more in the design phase of the vehicles and even to redesign the vehicle's structures that already are in the market. The crashworthiness optimization procedure helps the vehicle designers to produce great performing vehicles or to redesign some parts of existing vehicles with outstanding fuel economy, while still maintaining the highest possible safety standards.

Table 1.1: Frontal crash test requirement in the USA

Requirement	FMVSS 208
Impact speed	48 km/h (NCAP 56 km/h)
Impact object (obstacle)	Fixed rigid barrier
Vehicle place and directions	Full frontal perpendicular and (not for NCAP) angles of +/- 30 degrees
Dummy type and conditions	Unrestrained and belt restrained (NCAP), 50th percentile Hybrid III adult male
Injury criteria	Head injury criterion 1000 Chest deceleration 60 g Chest deflection 50 mm Femur force 10000 N

Table 1.2: Frontal crash test requirement in the European Union

Requirement	74/297 EC	96/79 EC
Impact speed	50 km/h	56 km/h (Euro-NCAP 64 km/h)
Impact object (obstacle	Fixed rigid barrier	Fixed deformable barrier
Vehicle place and directions	Full frontal perpendicular	40% overlap of the vehicle width directly in line with barrier face
Dummy type and conditions	No dummies	Belt restrained (NCAP), 50th percentile Hybrid III adult male
Injury criteria or structural criteria	Steering wheel intrusion horizontal and vertical direction 127 mm	Head injury criterion 1000 Chest deceleration 60 g Chest deflection 50 mm Femur force 10000 N Additional criteria on chest (viscous), the neck, the knee, lower leg bending, foot/ankle compression and intrusion of the compartment

The goal of this research

In order to reduce design's time and cost, high efficient finite element software are used in the optimization process to find vehicles reaction in impacts with other vehicles or objects at varying speeds, conditions and locations including frontal, side, pole and rear impacts. Normally optimization procedures are used to design vehicle structure or redesign some parts of it for optimal performance across a variety of situations and reduce its weight.

Although today some success has been achieved in the crashworthiness improvement and fuel consumption reduction of the vehicles, but the number of road fatalities and global climate warming as a result of high CO_2 emission highlight the need for significant improvement in vehicle crashworthiness and fuel consumption reduction. This research leads to a design of low weight vehicle frontal crash elements, which absorb the highest energy and ensure deceleration levels which are tolerable for drivers and passengers. Therefore, the general goals of this study are as follows:

- To use a vehicle finite element model to find detail information about crush performance of vehicle frontal crash elements in a full frontal crash based on NCAP test procedures and specially to introduce the most effective vehicle's frontal crash elements.
- To use crashworthiness optimization procedure to reduce vehicle's weight in such a way that the vehicle's structure meets and exceeds safety standards without sacrificing affordability.
- To investigate experimentally and numerically the crush performance of some important vehicle's frontal crash elements like bumper beam and crash box and use multi design optimization *MDO* to find the optimum crash elements which absorb the most energy while have minimum weight.
- To investigate the crush performance of the low density materials like aluminum honeycomb and foam and to study experimentally and numerically the strengthening effects of them in the filled crash box and bumper beam.
- To use *MDO* procedure to optimize geometry and material properties of the filled crash box and bumper beam. The optimum crash box and bumper beam should have maximum specific energy absorption and absorb the same energy as optimum empty crash box and bumper beam.
- To review analytical formulations which predict the crush behavior of the empty and filled bumper beams and crash boxes. To use experimental crash data to calibrate these expressions. This calibrated formulation can be used in the primary stage of the vehicle's design.

- To investigate the crush performance of the empty and foam-filled composite crash boxes experimentally and numerically and to find optimum composite crash box. Finally to compare the optimum composite and aluminum crash boxes.

The second chapter of this study deals with the crashworthiness investigation of vehicles in a frontal impact. The crush performance of the vehicle's frontal crash elements is determined and the optimization procedure is used to minimize the weight of selected frontal crash elements while safety standards are met. In chapter three the crush behavior of the aluminum tubes which are used as crash box is investigated experimentally and numerically. The existing analytical expressions which describe the crush performance of the metallic tubes are summarized and calibrated. The multi objective optimization procedure is used to maximize the energy absorption and specific energy absorption of the aluminum crash boxes. The strengthening effect of aluminum honeycomb and foam in the filled crash box is determined experimentally and numerically in chapter four. An optimization procedure is used to maximize the specific energy absorption of the foam-filled crash box while it absorbs the same energy as optimum empty crash box. The analytical formulas to describe the crush performance of the filled crash boxes are presented and calibrated. The bending behavior of the aluminum empty and foam-filled beams which are used as vehicle bumper beams are investigated experimentally and numerically in chapter five. The analytical methods which are developed to determine the crush performance of empty and filled beams are reviewed and calibrated. Similar to aluminum crash box, optimization procedure is used to optimize the crush behavior of empty and foam-filled aluminum beams.

Finally the crush responses of empty and foam-filled composite crash boxes are determined experimentally and numerically in chapter six. As well as aluminum crash boxes, the optimization procedure is used to find optimum composite crash box. The crush performance of optimum composite crash box is compared with optimum aluminum one.

2. Vehicle crashworthiness investigation and optimization

2.1 Introduction to the vehicle crashworthiness investigation

The ability of the vehicle's structure and any of its components to plastically deform and maintain a sufficient survival space for its occupants in crashes involving reasonable deceleration loads, is known as crashworthiness. Progressive crush zones are designed in the modern vehicle's structure to absorb the collision kinetic energy by plastic deformations in frontal, rear and side crashes. The occupant compartment should remain undeformed in frontal crashes to protect the driver and passenger's space and the crush deceleration pulse which acts upon the passengers should be as low as possible. In order to prevent to injure occupants, the steering column, dashboard, roof pillars, pedals and floor panels should not be pushed excessively inwards. The doors should remain closed during a crush and should be able to be opened afterwards to assist in quick rescue. The extra protection in rollover crashes is expected from strong roof pillars. Increased side door strength, internal padding and better seats can improve protection in side impact crashes. Most new cars have side intrusion beams or other protection within the door structure. Some cars also have padding on the inside door panels. Increasingly, car manufacturers are installing side airbags that provide protection from severe injury. Head-protecting side airbags, such as curtain air bags, are a more recent development and are highly effective in side impact and rollover crashes. A properly worn seatbelt provides good protection but does not always prevent injuries. Three point lap/slash seatbelts offer superior protection compare to two point seatbelts and should be installed in all seating positions. Head rests are important safety features and should be fitted to all seats-front and back. Head rest position is critical for preventing whiplash in rear impact crashes. Whiplash is caused by the head extending backward from the torso in the initial stage of rear impact, then being thrown forward. To prevent whiplash the head rest should be at least as high as the head's centre of gravity (eye level and higher) and as close to the back of the head as possible. Since the frontal impact is the most common collision scenario in the real word, see Figure 1.2 left, here, the crush behavior of the vehicle at this crash condition is investigated briefly.

2.2 Frontal vehicle crash investigation

The earliest crashworthiness research has focused on frontal vehicle crashes because this type of collision is the most common. The vehicle front structure is designed to manage the impact energy dissipation and protect its occupants as well as its partner vehicles'occupants.

Todays, to reduce the number of required standard crash tests, the computational crash analysis of the vehicle has become a powerful and efficient tool in reducing the cost and development time for a new product which meets government crash safety requirements. Nonlinear finite element crash analysis codes successfully simulate many laboratory vehicle crash tests, and can help to design vehicles that meet safety guidelines for crashworthiness.

A full vehicle finite element model is used here to explore the crash response of a vehicle in a frontal crash. For early evaluation of the crashworthiness of a vehicle, the most important responses are the passenger compartment acceleration, velocity and deformation. Figure 2.1 shows the final crush pattern of an impacted vehicle to a rigid wall. Figure 2.2 left shows the velocity of the vehicle passenger compartment as a function of time. This curve can approximately be split into three piecewise linear parts, i.e. response phases, see Figure 2.2 right.

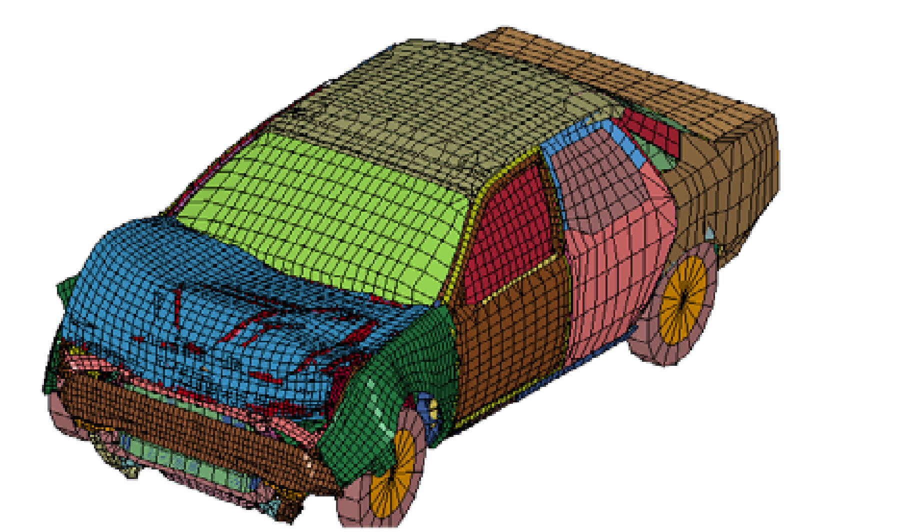

FE model form US national crash analysis center [121], [122]

Figure 2.1: Frontal crush model of Ford Taurus

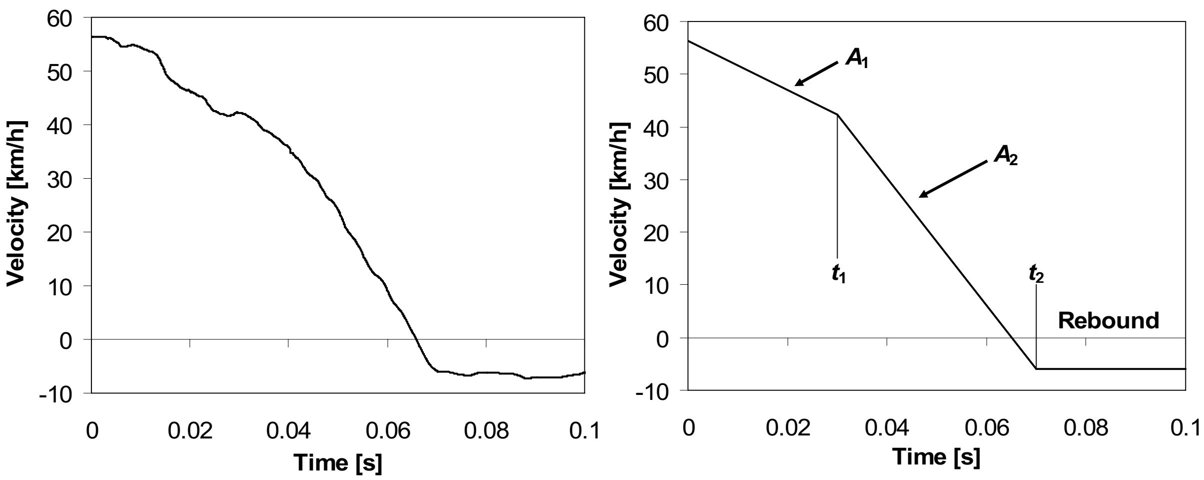

Figure 2.2: Velocity-time diagram from a frontal vehicle impact (left) and typical velocity response of a vehicle during frontal vehicle impact (right)

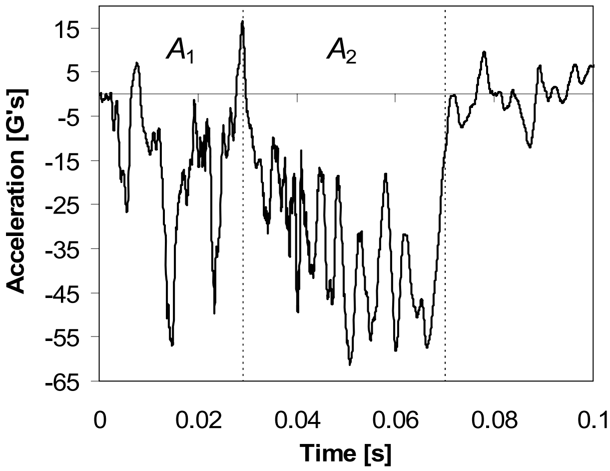

Figure 2.3: Acceleration-time diagram from frontal vehicle impact

The slopes of the curves at the phases are related to different major accelerations. Initial acceleration phase A_1 is the acceleration of the vehicle, prior to the time when the obstacle hits the engine. During this phase of the impact, the bumper, the crash boxes and frontal parts of the vehicle deform plastically and absorb kinetic energy. The second acceleration phase A_2 corresponds to the time when the wall or another obstacles hit the engine, the acceleration is rapidly increased and the velocity decreased. The last phase, rebound phase, occurs when the elastic deformation is recovered and the vehicle rebounds. These impact phases also can be found in the acceleration curve from Figure 2.3. In this figure the acceleration was filtered with an SAE 60 Hz low-pass filter. The acceleration amplitude is small up to about 0.03 second and has large peaks between 0.03 and 0.07 second and then it decreases in third phase.

Gadd (1966) [32] provided an analytical description of impacts and introduced the severity index (SI) as follow

$$SI = \int_0^{t_1} a_x \, dt, \tag{2-1}$$

Where a_x can be acceleration of any part of occupant's body and t_1 is impact duration. The significant response of occupants during collisions is determined by the deceleration profiles of each occupant's head and chest. Deceleration profiles for the occupant head and chest body segments can be determined from the occupant crash simulations. In 1971, Versace [109] modified Gadd's equation for handling long impact duration and presented a new equation which is known as the head injury criterion *HIC*. Therefore, two standard injury measures namely head injury criterion *HIC* and chest severity index *CSI* which are used to characterize the reaction of the occupant head and chest during the impact are defined as

$$HIC = \left[\left(\frac{1}{t_2 - t_1} \int_{t_1}^{t_2} a_h \, dt \right)^{2.5} (t_2 - t_1) \right]_{\max} \tag{2-2}$$

$$CSI = \left(\int_{t_1}^{t_2} a_c dt \right)^{2.5} . \qquad (2\text{-}3)$$

Where a_h and a_c are head and chest accelerations, respectively. For *HIC*, t_1 and t_2 expressed in second and measured during impact and (t_2 -t_1) is within 36 ms. For *CSI*, t_1 and t_2 are the initial and final times of the collision, respectively. These measures have shown to provide a consistently accurate summary of occupant response for the purpose of determining the extent and severity of injuries resulting from frontal impacts. The United States Federal Motors Vehicle Safety Standard FMVSS 208 allows a maximum *HIC* of 1000 in full frontal collisions at an impact velocity of 48 km/h. Additional requirements are maximum chest deceleration of 60 g. For example, at the *HIC*=1000, an occupant has an 80% chance of surviving. Clearly, the probability will vary greatly with occupant age and weight. Another new safety criterion is the New Car Assessment Program NCAP star-rating criterion. The NCAP star-rating criterion is derived from the total injury probability criteria combining the occupant *HIC* and Chest *G* numbers. The total occupant probability of severe injury is given by

$$P_{total} = 1 - (1 - P_{head})(1 - P_{chest}), \qquad (2\text{-}4)$$

Where

$$P_{head} = \frac{1}{1 + e^{(5.02 - 0.0693 headG)}}, \qquad (2\text{-}5)$$

$$P_{chest} = \frac{1}{1 + e^{(5.55) - 0.0693 cheastG}}. \qquad (2\text{-}6)$$

If occupant P_{total} is less than 10%, it is graded as 5-star in the NCAP star-rating system.

The real challenge in designing of the vehicles is to reduce their weight in such a way that the thrir structure meets safety requirements without sacrificing affordability. A complex function of initial conditions, geometric characteristics and material properties of both the vehicles and the occupants determine the severity of the injury acquired in vehicle crashes. Small changes in these inputs can cause significant changes in the output (i.e. occupant injury) depending on the timing and geometry of the load paths that are created and destroyed within the vehicle during the deformation process. A meaningful effort is to find main vehicle's and occupant's parameters which have the most influence on the occupant injury.

Although crashworthiness optimization study of the vehicle structure is not young, computational resources have speeded up its development. As an illustration of this trend, consider the fact that early crashworthiness simulation studies of the mid 1980's were followed by response surface based design optimization studies by Etman and Etman et al. in the 1990's for occupant safety [22], [23], component-level optimization by Marklund in year 1999 [71], Akkerman et al. (2000) [7] and Marklund et al. (2001) [72] and airbag-related parameter identification by Stander (2000) [105] and for a full-vehicle simulation Schramm and Thomas (1998) [95], Gu (2001) [34] and Yang et al. (2001) [116]. These studies focused on only single discipline in the optimization procedure. However, later, Yang et al. (2001) [117] extended the single discipline crashworthiness design optimization scenario to also include noise, vibration and harshness *NVH*.

For crashworthiness optimization, the objective functions, the criterion which should be minimized and constraints have mostly been related to occupant safety. The head injury criterion is often used as an objective (Etman (1997) [22], Etman et al. (1996) [23], Yang et al. (2001) [117]), along with the maximum knee force or a femur force-related criterion (Akkerman et al. (2000) [7]). Criteria related to other body parts namely the rib deflection criterion or viscous criterion, the abdomen protection criterion and pelvis performance criterion are implemented by Marklund (1999) [71]. Other objectives or constraints related to structural integrity are intrusion kinematics (displacement, velocity or acceleration) and the crash history, e.g. in a multi stage form of the acceleration versus displacement history, cp. Craig et al. (2002) [18]. The selection of the optimization parameters and criteria depends on the design criteria and type of crash, e.g., side impact, full and partially offset frontal impact or roof crash. An obvious choice of objective function is the total vehicle mass or the mass of the parts being designed, as it impacts positively on material and operating cost as well as fuel consumption. The criterion listed above would then enter the optimization problem as constraints to ensure a safe and lightweight vehicle. Design variables for crashworthiness design have mainly been geometrical in nature. Etman et al. (1997) [22] used airbag and seat belt variables, while Akkerman et al. (2000) [7] optimized the gauges and radii of the brackets and yoke of a knee-bolster system.

In this research the finite element simulation is used as a part of the optimization procedure. Before starting to optimize vehicle frontal structure, here, shortly the general optimization procedure and some essential tools which are used in this procedure are explained.

2.3 General optimization problem

Crashworthiness design problems can be systematically solved when formulated in the form of an optimization problem as

Minimize (or maximize) $f(X)$ under restrictions

$$\begin{aligned} &g(X) \geq 0, \\ &h(X) = 0, \\ &X = [x_1, \ldots, x_n]^T \qquad x_i \in X \qquad i = 1, \ldots, n_d \end{aligned} \tag{2-7}$$

Where X is the set of design variables x_i (which may be continuous, discrete or integer),

$$f(X) = [f_1(X), f_2(X), \ldots, f_m(X)]^T \qquad (m \text{ objectives}), \tag{2-8}$$

$$g(X) = [g_1(X), g_2(X), \ldots, g_p(X)]^T \qquad (p \text{ inequality constraints}), \tag{2-9}$$

$$h(X) = [h_1(X), h_2(X), ..., h_q(X)]^T \qquad (q \text{ equality constraints}). \tag{2-10}$$

Realizing the large range of the design space and the complexity of the nonlinear solution which is provided by the *FE* analysis solver, it is not hard to imagine that this approach may not necessarily lead to an optimum solution in a few iterations. It would require an exhaustive number of computationally expensive analysis simulations in a large design space with possibly high chances of converging in local minima, instead of reaching a true optimum solution. A more effective strategy is to replace the optimization problem in Equations (2-7) to (2-10) with a series of simpler approximate subproblems. In this approach, solutions of the subproblems are expected to yield the optimum of the original optimization problem. The k-th subproblem in this approach is defined as

$$\begin{aligned} &\text{Minimize (or maximize) } \underline{\tilde{f}}^{(k)}(X^{(k)}) \text{ under the restrictions} \\ &\underline{\tilde{g}}^{(k)}(x) \geq 0, \\ &\underline{\tilde{h}}^{(k)}(x) = 0. \end{aligned} \tag{2-11}$$

Where,

$$X^{(k)} = [x_1^{(k)}, ..., x_n^{(k)}], \qquad x_1^{(k)} \geq x_1, \quad x_n^{(k)} \leq x_n. \tag{2-12}$$

$x_1^{(k)}$ and $x_2^{(k)}$ define the bounds of the k-th subregion. $\underline{\tilde{f}}^{(k)}(X^{(k)})$ is a piecewise approximation of $f(X)$ in the k-ih subregion. Several approximation methods such as response surface method *RSM*, space mapping and stochastic technique are implemented to construct approximative subproblems. The subproblem in Equations (2-11) and (2-12) can be inexpensively solved by a conventional optimization method. Since in this research the *RSM* method is applied to construct the subproblems and a genetic algorithm is implemented to optimize the subproblems, these methods are reviewed briefly here.

2.4 Response surface method

Today, the response surface method *RSM* is the preferred tool to construct subproblems in the optimization procedure in the vehicle crashworthiness design. Several attempts have been made to use optimization methods in crashworthiness design problems. Etman et al. (1996) [22] and Etman (1997) [23] were among the first using *RSM* in structural optimization. Yamazaki and Han (1998) [115] crushed tubes into a rigid wall and compared the optimized results with real physical tests. They used *RSM* to construct approximative subproblems. Roux et al. (1998) [90] determined an optimal number of experimental points such that the surface approximation error was reduced a lot. Schramm and Thomas (1998) [95], (1999) [96] and Schramm (2001) [97], (2002) [98] have applied *RSM* in a vehicle design context. Marklund and Nilsson (2001) [72] were among the first to use *RSM* in an industrial application. They minimized the mass of a B-pillar of a vehicle. Sobieszczanski-Sobieski et al. (2000) [104] used *RSM* to minimize the mass of a vehicle when the roof crush performance was coupled to its noise, vibration and harshness *NVH* as constraints. Yang (2002) [118], (2003) [119] have investigated several industrial applications of optimization and multidisciplinary optimization using *RSM*. Redhe and Nilsson (2002) [85], Redhe et al. (2002) [86] and Redhe and Nilsson, (2002) [87] studied different aspects of *RSM* in crashworthiness applications and carried out some work on space mapping compared to *RSM*. Craig et al. (2002) [18] applied *RSM* to multidisciplinary optimization where he separated the design variables for the different disciplines. In the response surface method, the design domain is the space spanned by the design variables, i.e. $\{x_1, x_2, ..., x_i\}$. The design domain can be further narrowed by introducing limits on the design variables separate from the global limits. This creates a subdomain called the region of interest; see Figure 2.4, where the approximations are calculated. When the optimum is found, the region of interest is moved in the indicated direction during the next iteration of the optimization process. The selection of approximation functions to represent the actual behavior is essential. These functions can be polynomials of any order or the sum of different basis functions, e.g. Sine and Cosine functions. For a general quadratic surface approximation the function will be

$$y_i = \beta_0 + \sum_j \beta_j X_{ij} + \sum_j \sum_k \beta_{ik} X_{ij} X_{ik} + \varepsilon_i, \qquad i = 1,2,..., N. \tag{2-13}$$

Where, the different parameters β are the constants which to be determined, X_i are the design points in the region of interest and ε_i includes both bias and random errors and N is the number of the experimental points. Obviously, the minimum number of experimental points (N_{min}) is equal to the number of unknown constants β_i. By examining Equation (2-13) it can be concluded that for two design variables the minimum number of experimental points is three for a linear surface approximation, five for an elliptic and six for a quadratic surface. A generalization of this observation is found in Table 2.1, where the minimum numbers of simulations for different approximations are stated as function of the number of design variables. Here, n_d is the number of design variables. When using higher order polynomials over fitting may be an issue. There exists methods to avoid this effect, e.g. by iteratively removing one term in the polynomial and selecting the basis set with the least surface approximation error. In order to minimize the error ε_i the least square method is used to find the estimation of β_i. How the experimental points should be distributed in the region of interest is a delicate and important task, which is explained in Section 2.5.

2.5 Experimental design

The problem of distributing the experimental points in the region of interest is known as selecting a design of experiment *DOE*. The difficulty lies in the attempt of minimizing the number of experiments, but at the same time achieving a surface approximation with good quality. A popular design of experiment in structural analysis is the D-optimality criterion, but several other methods exist which two popular of them are briefly introduced in the following.

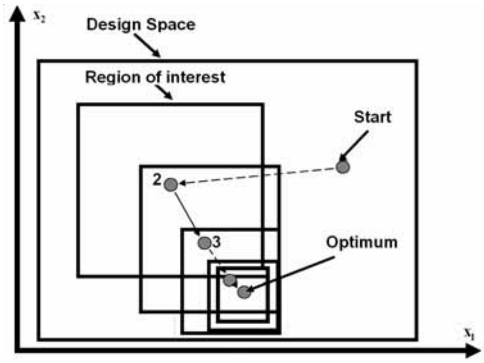

Figure 2.4: Example of the design domain and region of interest (two variables x_1 and x_2)

Table 2.1: Minimum number of simulations, N_{min}, as function of the number of variables, n_d

Assumption	N_{min}
linear	$n_d + 1$
elliptic	$2\,n_d + 1$
quadratic	$(n_d + 1)(\,n_d$

2.5.1 Koshal design

Koshal (1933) [57] proposed a design of experiment which uses a minimum number of simulations. The Koshal design uses a "one factor at the time" approach. This approach will end up with a saturated system of equations for the surface construction. The advantages for a Koshal design are minimum number of experimental points, which influence the accuracy of the surface approximation.

2.5.2 Factorial design

In contrast to the Koshal design, the factorial design places a grid on the region of interest and the simulations are evaluated at all grid points. The number of experimental points N_p in the factorial design is $N_p = P^k$. Where k is the number of design variables involved and P determines the grid intensity in the region of interest. There is also a coupling between P and the order of the functions used for the approximation since at least as many simulations as there are unknown constants have to be carried out. The factorial design is very expensive, especially when the number of design variables increases.

2.5.3 D-optimality design

The D-optimality criterion belongs to the class of so called alphabetic optimality criteria. All of the alphabetic optimality criteria are based on some property of the prediction variance of the approximation; see Myers and Montgomery (1995) [74]. The use of the D-optimality criterion is closely related to the factorial design. The D-optimality criterion chooses only some points from the set candidate of factorial design. The factorial experimental design creates N_p mesh of design points. Then, N_q points out of N_p candidate points are selected using

D-optimality criterion. The D-optimality criterion selects different design points in the design space for different *RSM* approximation types. Notice that it is up to the user to define the number of functional evaluations that should be used. The D-optimality criterion will then define the locations in the region of interest where to evaluate the functions. Generally the percentage of acceptable error is a key to determine number of functional in the D-optimality design of experiments.

2.6 Genetic algorithm

Genetic algorithms *GA* are a part of evolutionary computing, which is a rapidly growing area of artificial intelligence. Genetic algorithms are inspired by Darwin's theory about evolution. The idea of evolutionary computing was introduced in the 1973 by Rechenberg in his work on evolution strategies [84]. His idea was then developed by other researchers. Genetic algorithms were invented by John Holland and developed by him and his students and colleagues [45]. Genetic algorithm is started with representation of a solution to the problem as a genome (or chromosome). In order to perform the genetic operators this algorithm encodes the solutions to the binary values. The genetic algorithm then creates a population of solutions and applies genetic operators such as mutation and crossover to evolve the solutions in order to find the best one(s), see Figure 2.5. Solutions which are selected to form new solutions (offspring) are selected according to their fitness - the more suitable they are the more chances they have to reproduce. This is repeated until some condition (for example number of populations or improvement of the best solution) is satisfied. The outline of the basic Genetic algorithm is:

1. [Start] Generate random population of n_c chromosomes (suitable solutions for the problem),

2. [Fitness] Evaluate the fitness $f(x)$ of each chromosome x in the population,

3. [New population] Create a new population by repeating following steps until the new opulation is complete,

    [Selection] Select two parent chromosomes from a population according to their fitness (the better fitness, the bigger chance to be selected),

    [Crossover] With a crossover probability cross over the parents to form a new offspring, (children). If no crossover was performed, offspring is an exact copy of parents,

    [Mutation] With a mutation probability mutate new offspring at each locus (position in chromosome),

    [Accepting] Place new offspring in a new population,

4. [Replace] Use new generated population for a further run of algorithm,

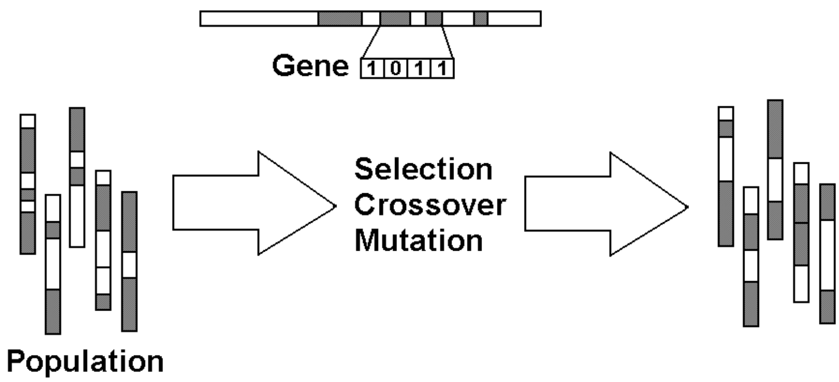

Figure 2.5: Schematic presentation of the genetic algorithm method

5. [Test] If the end condition is satisfied, it stops, and returns the best solution in current population,

6. [Loop] Go to step 2

2.7 Optimization of the frontal vehicle's structure

When designing a vehicle's front structure for NCAP, the vehicle deceleration-time history and the maximum crush distance are important to protect the occupants of the vehicle. It is clear that, the stiffness of the vehicle is proportional to the mass of the vehicle. The thicker vehicle front parts are, the stiffer its front structure will be. In order to optimize the vehicle front structure, in this study the chest and head injury criteria, maximum crush distance and total vehicle mass are considered. The vehicle frontal impact is simulated using a full-scale FE model of a Ford Taurus, see Figure 2.1. The optimization process is applied to design the vehicle frontal structures in order to satisfy crashworthiness requirements. The model has about 280,000 elements. The FE vehicle model was originally developed and validated at the national crash analysis center NCAC of the USA for a full frontal impact [120], [121]. The initial velocity of the vehicle is 56.3 km/h (35 miles per hour). The CPU time for a single run is about 5 hours using four 440 MHz parallel CPUs. All the impact simulations were performed using LSDYNA v970 [36].

A vehicle's safety performance can be measured by various safety parameters such as intrusion distance, intrusion velocity, peak acceleration, and contact force. These parameters are not totally independent of each other. There is no obvious solution for identifying those components whose design changes may strongly affect the safety parameters. These safety parameters, however, are closely related to the vehicle's energy absorption history that consists of both energy absorption capacity and energy absorption rate. The more energy can be absorbed by the vehicle in the early stage of an impact, the less injury will incur on the occupant. Therefore, an analysis on the energy absorption history will help identifying those important components. Since a vehicle impact finishes in a short period (in the magnitude of

100 ms), both the energy absorption capacity and absorption rate are important. A large energy absorption capacity is necessary but not sufficient, because the stress waves pass through a component if the energy cannot be absorbed quickly. Based on this understanding, the energy absorption of all vehicle frontal components at 20, 40, 60 and 100 ms are examined, and the components with large energy absorption capacity are determined. Based on the simulation result about 60 percent of the kinetic energy is absorbed only by thirteen components: the bumper beam, the outer and inner rail, right and left apron, outer and inner shotgun, right and left cradle rail, crash boxes, upper and lower frontal cross cradle. Here the nine most effective components are selected to be considered in the optimization procedure; they are shown in Figure 2.6. Figure 2.7 shows the time histories of energy absorptions of selected components compared to those of the whole vehicle. The nine components account for 59%, 53%, 50%, 51% of the vehicle's total internal energy at 20, 40, 60, 100 ms, respectively. These contributions are significant considering the fact that the nine components only hold 2.26% of the total vehicle's weight. Figure 2.7 shows two curves with the initial values coinciding with each other. That means most of the impact in the first stage of impact are absorbed by these nine elements.

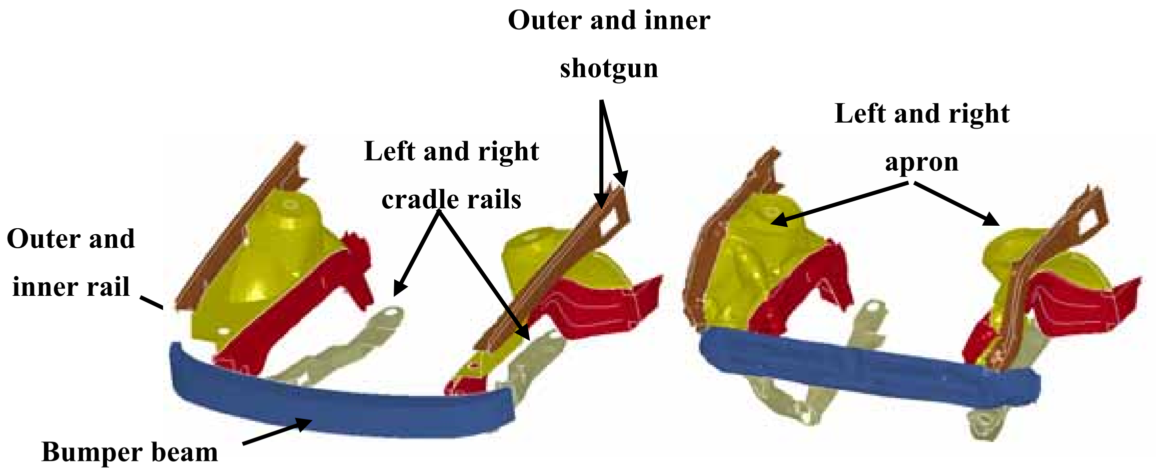

Figure 2.6: Frontal structure of the vehicle, before impact (left) after impact (right)

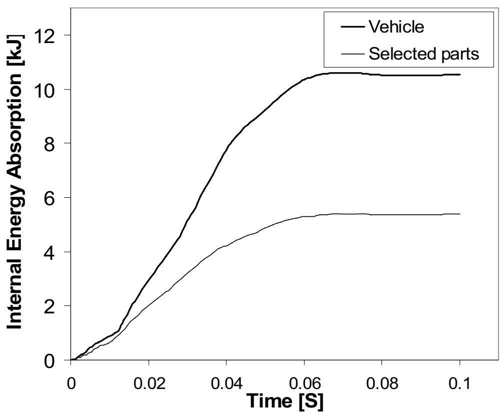

Figure 2.7: Time histories of the vehicle and components' internal energy

Table 2.2: The bounds on design variables

Variable name	Lower bound	Starting value	Upper bound
Bumper beam	1	1.5	3
Inner rail	1	1.5	3
Outer rail	1	2	3
Inner and outer shotguns	1	1.3	3
Left and right aprons	1	1.3	3
Left and right Cradle rails	1	1.93	3

The thicknesses of the selected components are used as design variables for size optimization. A total of six design variables are needed for the nine components due to component symmetry. In the optimization procedure, the mass of the selected components is to be minimized with imposed constraints on maximum structure intrusions D_{max}, the dummy head injury criterion *HIC* and chest severity index *CSI*. The optimization problem is written as

Minimize vehicle mass M subject to

$$HIC \leq HIC_0,$$
$$CSI \leq CSI_0,$$
$$D_{max} \leq D_0.$$

Where HIC_0, CSI_0 and D_0 are the head injury criterion, the chest severity index and maximum crush distance of the vehicle with original crash elements, respectively. Maximum crush distance is the vehicle maximum deformation measured during the crush event. The variables are only thicknesses of the parts and no shape optimization is considered. Figure 2.6 left and right show the frontal vehicle structure before and after crash, respectively. The bounds on design variables are given in Table 2.2.

The general procedure of the implementation of the crashworthiness optimization is explained in Figure 2.8. In this procedure after replacing the optimization problem by a series of simpler approximative subproblems which can be constructed by using *RSM*, the subproblems can be solved by an optimization method. In this study, the genetic optimization algorithm that is provided in [75] was utilized to solve the subproblems. The first step in the construction of an approximate function by *RSM* is to assume its form. This information is needed to select enough points to create the approximation efficiently. Every point is the result of one numerical simulation.

Here, linear *RSM* is selected to reduce the number of simulation. In order to reduce the CPU cost in this approach, the D-optimality design of experiments method is used. This method reduces the number of required points for the construction of approximate functions. After four iterations the optimum values were obtained. The total numbers of simulations are 55. In every iteration, the optimum design result is compared with the reanalysis solution. If reanalysis solution is not satisfied, new response surface models are built by adding the reanalysis results. The next optimization is then carried out from the new response surfaces. The comparative optimization histories of the optimization function, variables and constraints are shown in Figure 2.9. This figure shows that the total component's mass is reduced about 9% while vehicle safety performance is improved after optimization. There is 9.9% improvement in the *HIC* and the maximum intrusion is reduced 0.66% with respect to original intrusion. Finally the *CSI* is improved about 0.99%. Also it can be seen how the optimization parameters varies in every iteration. Here, the thicknesses of some parts are increased from initial values and some of them are reduced.

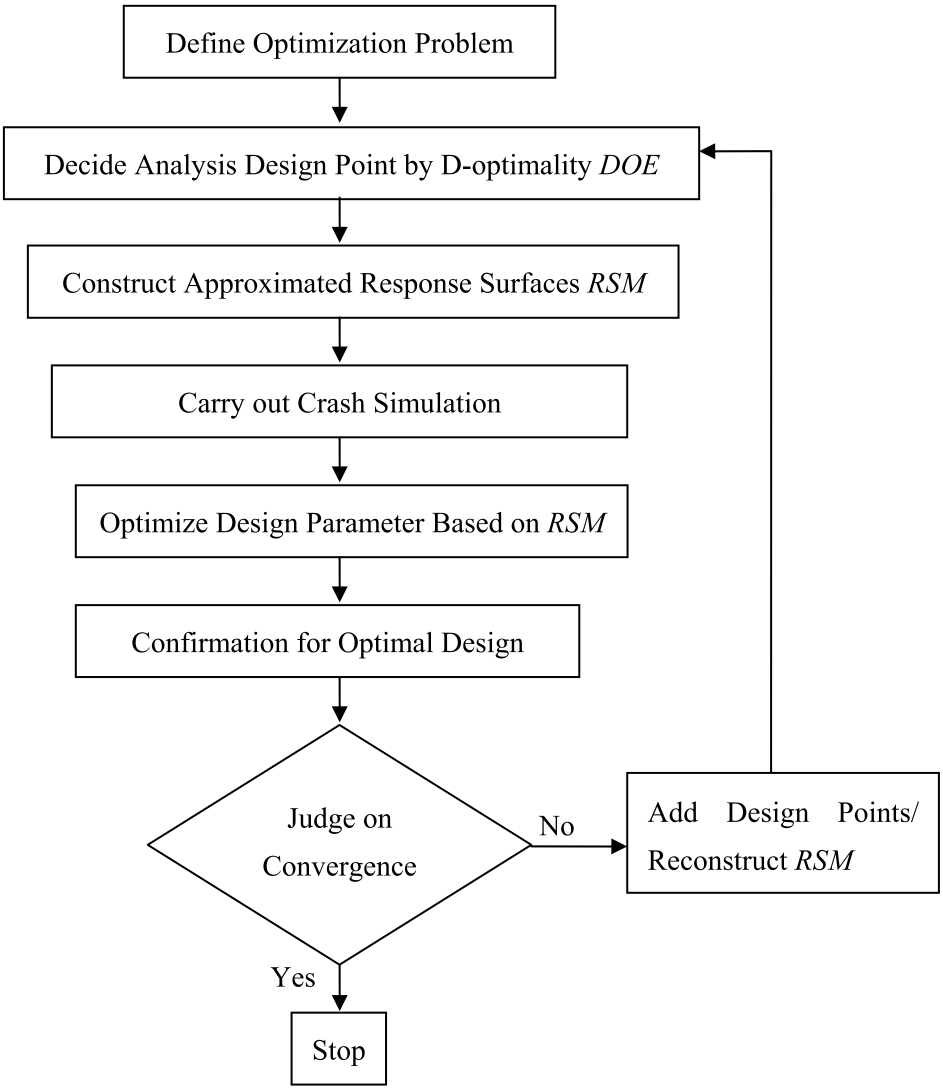

Figure 2.8: Flowchart of the optimization process

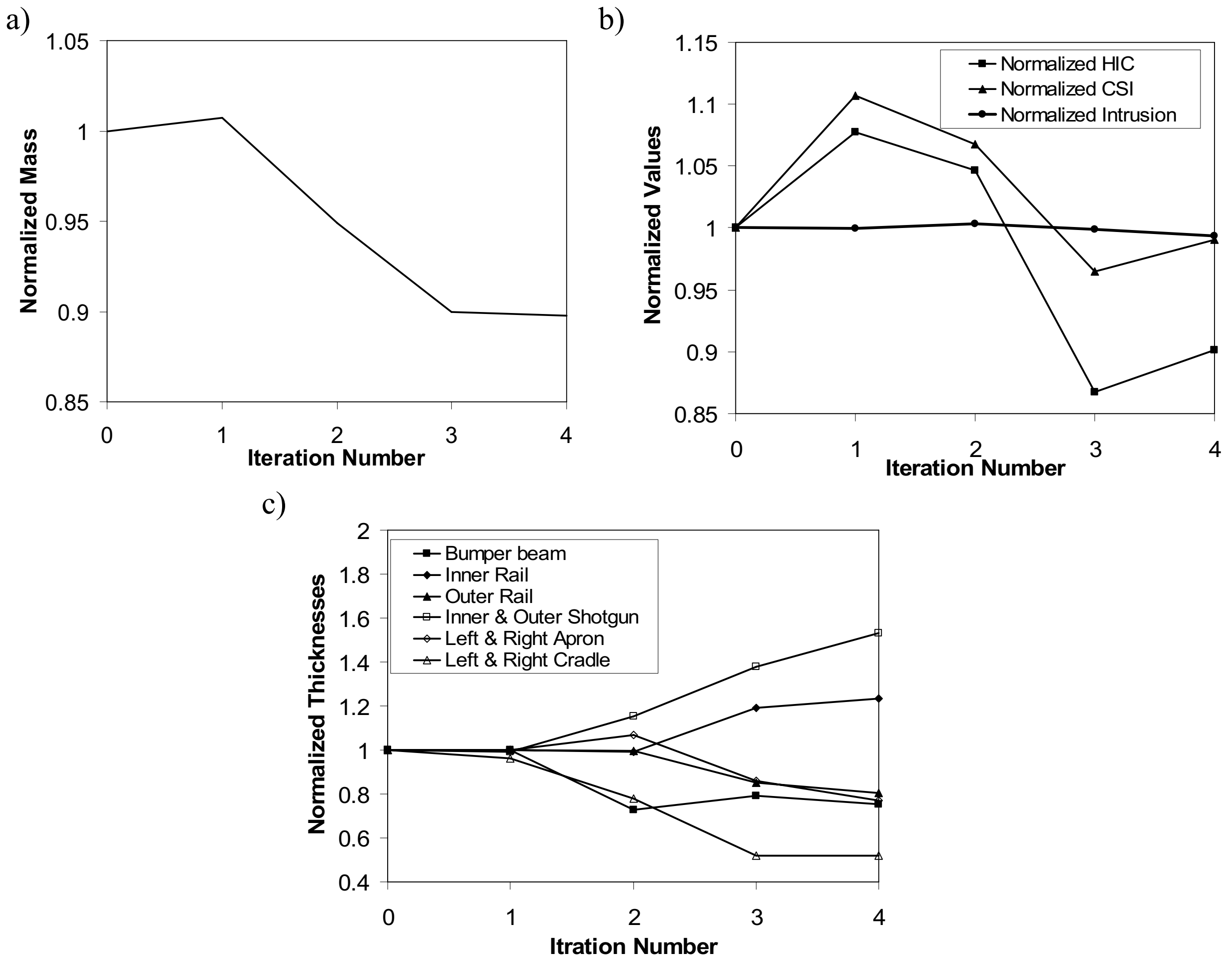

Figure 2.9: Variation of the a) vehicle component's weight b) optimization constraints c) normalized thickness of the vehicle components

In this study only the thicknesses of the vehicle parts were selected as optimization parameters. It is not hard to imagine how effective the vehicle's weight can be reduced if in addition to the thickness, the shape and material properties of the parts are selected as optimization parameter. It should be emphasized that a good selection of optimization parameters is also determinative. As mentioned before, a large energy absorption capacity is necessary but not sufficient. The energy absorption in the first stage of the impact is also an important parameter. Here, the results of vehicle crash simulation showed that, a large amount of impact energy is absorbed only by the bumper beam. On the other hand it has been seen that the vehicle crash boxes are the first crash element which start to crush in the first moment of collision. The more energy can be absorbed by the vehicle in the early stage of an impact, the less injury will incur on the occupant. Therefore in the next chapters a comprehensive study will be done to investigate the crush behavior of the vehicle's bumper beam and crash box. The optimization procedure will be implemented to improve the weight and crush efficiencies of these two elements.

3. Crush performance investigation and optimization of aluminum tubes

3.1 Introduction to the crush performance of aluminum tubes

There have been considerable activities on dynamic crush of thin walled tubes during the past decades and a significant part of these efforts have been concerned with the use of these structures in the energy absorbing structure of vehicles. Thin walled columns are connected to the vehicle bumpers as crash boxes to protect passengers and the structure itself during collision. As an example Figure 3.1 shows the main structure of Audi model A8 and it's crash boxes which are made from aluminum. Here, the crash boxes are part of the vehicle's frontal rails. The crash boxes absorb the initial kinetic energy in the first stage of the impact, to keep the force levels sufficiently low and to avoid damage to the engine cooling system and other high cost components. Energy absorption normally takes place by progressive buckling of columns. A distinctive feature of such a deformation mechanism is that the rate of energy dissipation is concentrated over relatively narrow zones, while large parts of the structure undergo a rigid body motion.

Traditionally steel alloys were used in the vehicle energy absorption systems but since several years aluminum alloys are used due to their weight and crashworthiness benefits. The use of aluminum for crash energy management has many advantages:

- The high strength to weight ratio of the aluminum allows strong, yet lightweight body structures to be built.
- For the same weight, aluminum allows for larger crush zones compare to steel which serve to reduce forces on vehicle occupants in a crash.

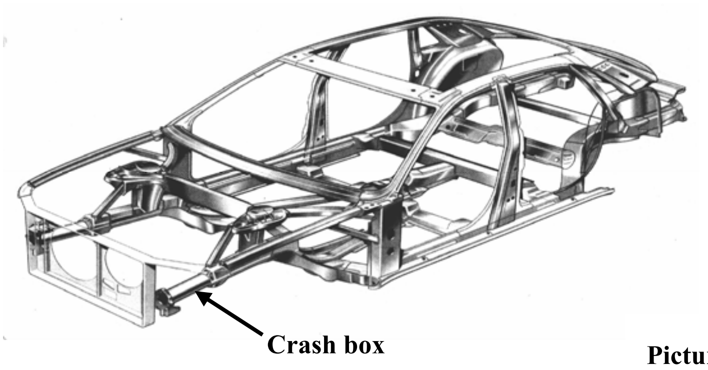

Picture from Volkswagen AG

Figure 3.1: Body-in-white image of Audi model A8

- Aluminum structural members can be engineered to collapse in a predictable manner in severe impacts and, as a result, can be designed to provide the desired amount of crush energy absorption.
- The good corrosion resistance of aluminum minimizes deterioration of the crush energy absorption capabilities over the life of the vehicle.

Using aluminum alloys in vehicle structure will provide simultaneous improvement in fuel economy, crush performance and safety, a compelling combination for vehicle manufacturers and their customers. The benefits of using aluminum in vehicle design allow automotive designers to maintain vehicle size and occupant safety while achieving up to 25% vehicle weight saving.

Kröger (2002) [58] introduced three mechanisms that can be used when aluminum tubes are considered as energy absorption device, namely progressive buckling, tapering and inversion. He investigated in detail the crush behavior of tube in each of these mechanisms and made a comprehensive comparison between energy absorption capacities of them [59]. Figure 3.2 shows schematically the geometry of the aluminum tube in each of the mentioned mechanisms. The results of his work showed that the tapering followed by progressive buckling mechanisms has higher energy absorption capacity and the inversion mechanism has the lowest. Here, for more realization, three real car crash boxes are presented in Figure 3.3. The position of the initiation of the crush is marked by circle. The inversion mechanism is used e.g. in the MCC Smart and the tapering mechanism is implemented e.g. for VW passat while progressive buckling is used e.g. in Audi A8 vehicle.

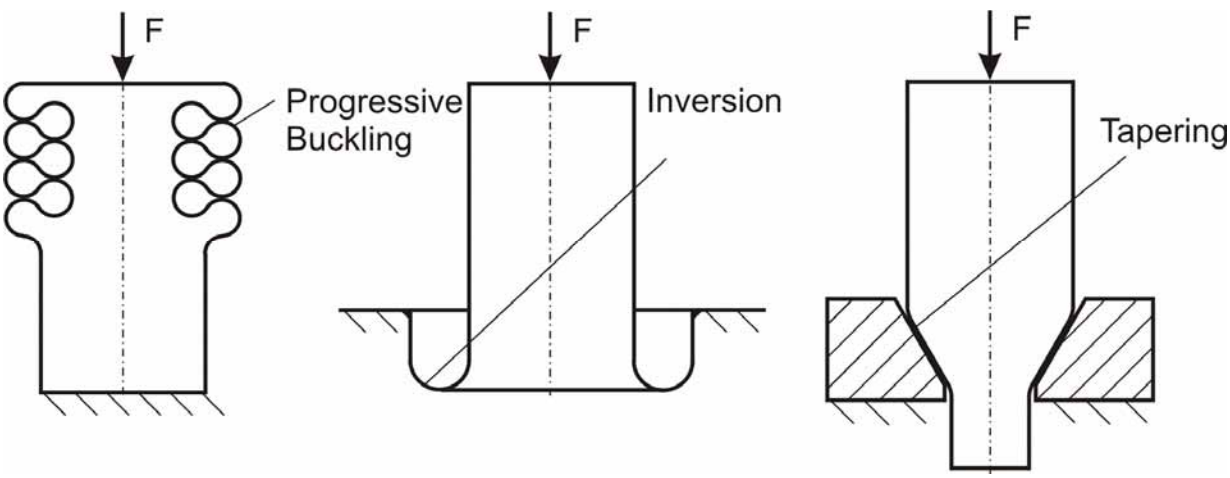

Figure 3.2: From the left: Progressive buckling, inversion and tapering mechanism, respectively

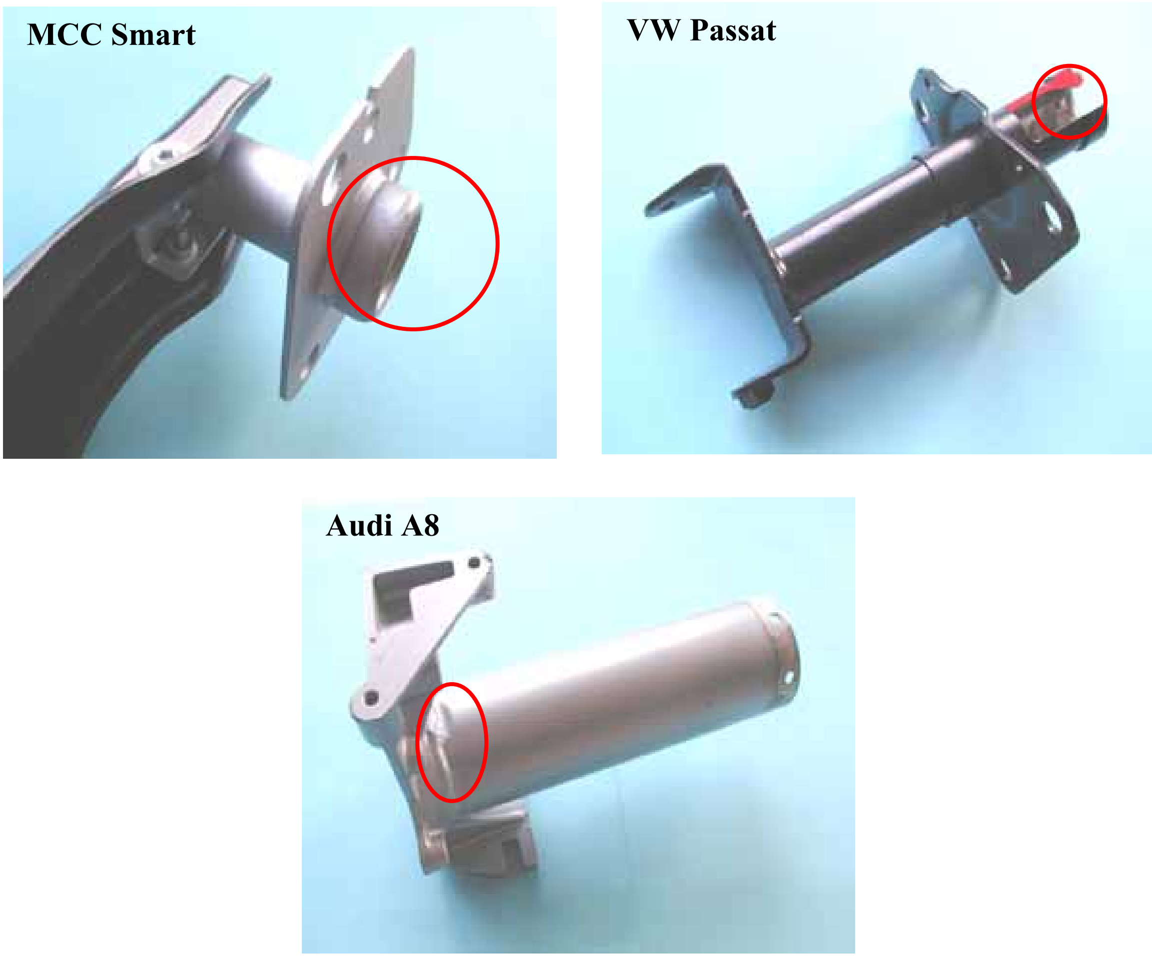

Figure 3.3: Some real crash boxes

Good energy absorption and simplicity of the progressive buckling made this mechanism attractive for vehicle designers. A typical crush load displacement characteristic of an aluminum column in progressive buckling is shown in Figure 3.4. Except the initial peak, the load–displacement behavior exhibits a repeated pattern. Each pair of peaks is associated with the creating of one lobe. Generally the formation of the lobes starts sequentially from one end of the tube and repeats up to tube densification. So this behavior is known as progressive buckling. Hence, to quantify the crush characteristics of the tubes, the mean crush load P_m, the length of the folding wave $2H$, and absorbed energy E become significant parameters. Conventionally crush load is expressed as non–dimensional ratio, P_m/M_0 where $M_0=\sigma_0 t^2/4$ is the full plastic bending moment. Here, σ_0 and t denote the tube flow stress and the thickness, respectively. The value of the specific energy absorption *SEA* is the ratio of the absorbed energy to the mass of the crushed structure. High values indicate light weight crash absorbers. The parameter crush load efficiency η that can be calculated from crush history of structures is the ratio of mean load to maximum peak load.

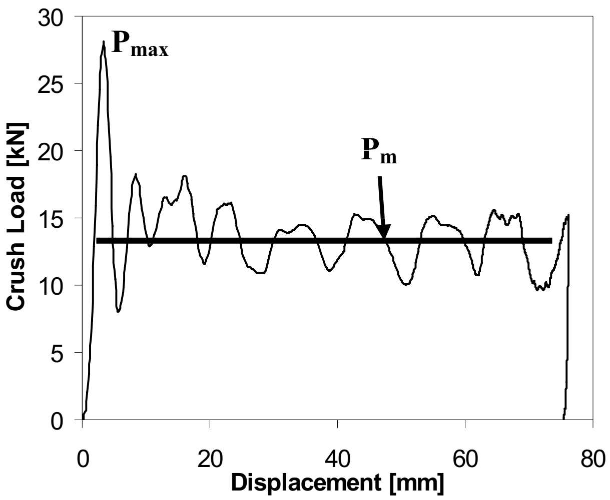

Figure 3.4: Typical crush load-displacement diagram of aluminum tube

Here, the results of experimental and numerical investigations on crush performance of circular and square aluminum tubes in progressive buckling are presented. The experimental tests were conducted on the drop weight test rig; see Figure 3.5, which is installed in the Institute of Dynamics and Vibrations Research at the Leibniz University of Hannover. This test rig has a top mass which can be varied from 20 to 300 kg and the maximum drop height is 8 m which results in a maximum impact speed of 12.5 m/s. The force, moments and displacement are recorded with a PC using AD-converter. The deformation force is measured using strain gauges and a laser displacement sensor provides the axial deformation distance of the tubes. The crash test specimens are made from commercial quality extruded 6060 (AlMgSi0.5F22) aluminum alloy with thickness of t, diameter d and length l in the as-received heat treated condition. Mechanical properties were determined from standard tensile tests of coupons cut from several tubes based on ISO 6892. The aluminum alloy has a 0.2% proof stress, $\sigma_{0.2}$ =231 MPa, and ultimate stress, σ_u =254 MPa.

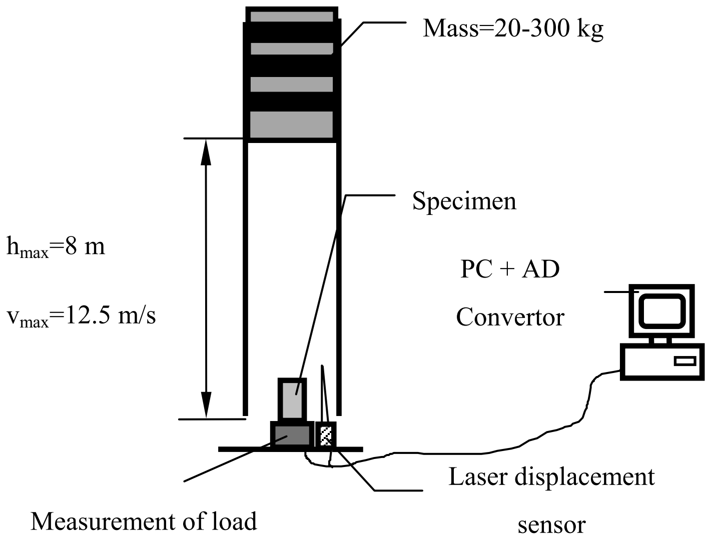

Figure 3.5: Test rig

Numerical simulations of the crash tests are performed to obtain detail information about crush process of the tube, which are difficult to measure during impact loading. The modeling and analysis is performed on a UNIX server using the explicit finite element code LS-DYNA.

3.2 Crush performance of circular aluminum tubes

Circular tubes under crush load achieve different crash modes based on their length and cross section dimensions. A circular tube of mean diameter *d* and thickness *t*, when subjected to an axial impact load, collapses in an efficient manner, either in axisymetric buckles (concertina mode) or in a non–axisymetric (diamond mode) or mixed mode pattern. However, when its length is greater than the critical length for a given tube, it deforms in the overall Euler buckling mode, which is an inefficient mode of energy absorption in the view point of crashworthiness. Analytical aspect of this problem was investigated by several researchers. It is interesting to compare the analytical findings on mean crush load and length of folding wave for axisymetric and non-axisymetric collapse of tubes with experimental results. Here, the derived formulations to predict the crush performance of metallic tubes are summarized and compared with the experimental results. Finally the finite element method is used to find detail information about the crush process.

3.2.1 Analytical investigations

Andrews et al. (1983) [9] experimentally investigated the mode of deformation of aluminum tubes of *d/t*= 4-60 (diameter/thickness), *l/d* = 0.2-8.88 (length/thickness). Consequently, they developed a collapse mode classification chart which predicts the mode of collapse for any given *d/t* and *l/d* combination. Alexander (1960) [8] was the first researcher to propose a theory for the axisymetric collapse mode based on balance of external and internal work done. His simple model assumes the formation of three plastic hinges, and that the collapsing length 2*H* of the tube consists of two straight arms between the hinges. Expressions for mean crushing load and length of folding wave are

$$\frac{P_m}{M_0} = 20.73\left(\frac{2R}{t}\right)^{0.5} + 6.283, \qquad \frac{H}{R} = 1.905\sqrt{\frac{t}{2R}}, \qquad \text{for concertina mode.} \tag{3-1}$$

Pugsley (1979) [79] developed his previous work with Macoualy (1960) [80] for the case of four equal diamonds around the tube and produced an expression for mean crushing load of axially crushed tube deforming in five diamond lobes,

$$\frac{P_m}{M_0} = 0.326\left(\frac{2R}{t}\right) + 217.7, \qquad \text{for diamond mode.} \tag{3-2}$$

Abramowicz (1983) [1] and Abramowicz and Jones (1984) [2] proposed an improved model with the tube wall bending in the meridional direction into two oppositely curved arcs instead of a straight line and presented the following equations for mean crush load and half wave length of folding,

$$\frac{P_m}{M_0}=\frac{25.23\left(\frac{2R}{t}\right)^{0.5}+15.09}{0.86-0.568\left(\frac{t}{2R}\right)^{0.5}},\qquad \frac{H}{R}=1.84\sqrt{\frac{t}{2R}},\quad \text{for concertina mode and} \quad (3\text{-}3)$$

$$\frac{P_m}{M_0}=A_{1N}\left(\frac{2R}{t}\right)^{0.5}+A_{2N}, \quad \text{for diamond mode.} \quad (3\text{-}4)$$

Where A_{1N} and A_{2N} are two parameters which are defined based on the number of non-axisymetric lobes N_d. The parameter A_{1N} is 31.01, 28.86 and 28.23 and A_{2N} is 17.22, 44.74 and 83.15 when N_d= 2, 3 and 4, respectively.

Guillow et al. (2001) [35] did a complete set of crash test on the circular aluminum tubes with *d/t*=10-450 and found an empirical formula for both axisymetric and non–axisymetric modes,

$$\frac{P_m}{M_0}=72.3\left(\frac{2R}{t}\right)^{0.32}, \quad \text{for concertina and diamond modes.} \quad (3\text{-}5)$$

Wierzebicki and Bhat (1986) [110] present an improved analytic model based on energy balance method and further he and his collogue (1992) [111] addressed the fact that experimentally the tube wall is observed to fold both inward and outward. They introduced a parameter known as the eccentricity factor, m_s, which was defined as the ratio of outward fold length to the total fold length. This work was further refined by Singace et al. (1996) [102].

Wierzbicki (1986) [110] presented the equations

$$\frac{P_m}{M_0}=62.88\left(\frac{2R}{t}\right)^{0.33}, \quad \frac{H}{R}=0.816\left(\frac{t}{2R}\right)^{0.33}, \quad \text{for diamond mode and} \quad (3\text{-}6)$$

$$\frac{P_m}{M_0}=30.5\left(\frac{2R}{t}\right)^{0.5}, \quad \frac{H}{R}=2.67\left(\frac{t}{2R}\right)^{0.5}, \quad \text{for concertina mode.} \quad (3\text{-}7)$$

Wierzbicki et al. (1992) [111] presented the equations

$$\frac{P_m}{M_0}=31.74\left(\frac{2R}{t}\right)^{0.5}, \quad \frac{H}{R}=1.31\left(\frac{t}{2R}\right)^{0.5}, \quad \text{for concertina mode.} \quad (3\text{-}8)$$

Singace et al (1996) [102] presented the formula

$$\frac{P_m}{M_0}=22.27\left(\frac{2R}{t}\right)^{0.5}+5.632, \quad \text{for concertina mode.} \quad (3\text{-}9)$$

Singace A.A. (1999) [103] presented an analytic method for calculating the mean crush load in the case of non-axisymetric mode of deformation. The analytical outcome of his work is

$$\frac{P_m}{M_0} \cong -\frac{\pi}{3}\tan\left(\frac{\pi}{2N_d}\right)\frac{R}{t}, \qquad \frac{H}{t} = \frac{\pi}{N_d}\tan\left(\frac{\pi}{2N_d}\right)\frac{R}{t}, \qquad \text{for diamond mode. (3-10)}$$

That N_d is the number of non-axisymetric lobes.

Figure 3.6 left and right shows the test results for P_m/M_0 compared with theoretical equations for concertina and diamond crushes, respectively. Here, an average of yield stress and ultimate stress extracted from true stress-strain curve is used in calculation of flow stress. In view of Figure 3.6 left, response of tube with d/t= 40, 20 and 15.6 have good agreement with equation (3-3) and also empirical equation (3-5) is near to the experimental results. Also from Figure 3.6 right, it can be seen that for non-axisymetric mode, equation (3-4) and (3-6) is very good in agreement with the experimental results. Equations (3-2), (3-5) and (3-10) can present a close agreement with experiment results of relatively thin tubes. Equation perused by Abramowicz and Jones and equation presented by Singace have a reasonable result when the numbers of lobes are known.

3.2.2 Experimental and numerical results

Experimental impact with different velocities on circular tubes with the diameter of 40 mm and length of 180 mm and different thicknesses were generated, see Table 3-1. Here the lower end of tubes is fixed by means of special steel clamps that embedded a distance of 30 mm outside of the tubes and close fitting steel inserts are placed inside the end of the tube over the same length of external fixture for fixing the periphery of the specimens. After each test, the crush data were filtered and then the load-displacement curves were plotted.

The maximum crush load P_{max} corresponds to the first peak and the area under this curve is absorbed energy E. The mean crushing load P_m from the experimental results is defined by

$$P_m = 1/\delta \int_0^{\delta} P(\delta)d\delta . \qquad (3\text{-}11)$$

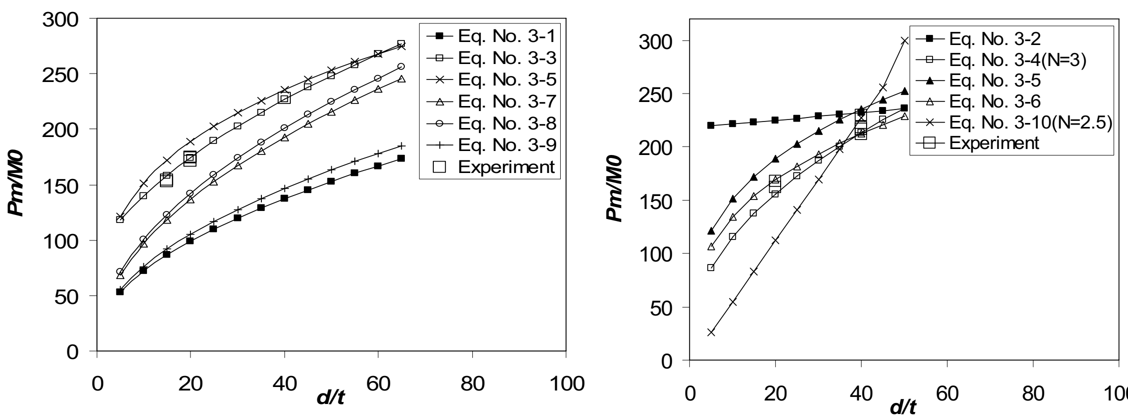

Figure 3.6: Comparison of present experimental results for crush loads with different experimental and theoretical equations; concertina (left) and diamond (right)

Table 3.1: Experimental crash results of aluminum tubes AlMgSi0.5F22, ϕ 40 mm

Test No.	V [m/s]	t [mm]	N_s [-]	N_d [-]	P_{max} [kN]	S_{max} [mm]	E [J]	SEA [J/kg]	P_m [MPa]	η [%]
S-1	4.3	1	2	2.5	24	76	1041	40286	13.7	57.1
S-2	4.3	1	1	2.5	28	76	996	38545	13.1	46.8
S-3	4.3	1	0	3.5	30	79	1044	38868	13.2	44
S-4	4.3	1	3	2	29	78	998	37632	12.8	44.1
S-5	4.3	1	1	3	28	77	1042	39801	13.5	48.2
S-6	4.8	1	1	4	29	96	1334	40870	13.5	46.6
S-7	4.8	1	10	0	28	94	1296	40551	13.8	49.3
S-8	5.2	1	1	4.5	28	118	1554	35708	13.1	46.8
S-9	5.2	1	1	4.5	24	113	1541	40109	13.5	56.3
S-10	5.2	1	12	0	21	109	1536	41446	13.9	66.2
S-11	5.2	1	2	2.5	29	114	1545	39861	13.4	46.2
S-12	5.9	2	2.5	0	63	47	1858	70379	42.5	67.5
S-13	5.9	2	2.5	0	60	48	1859	68699	42.3	70.0
S-14	6.6	2	3	0	61	51	2326	69103	41.6	68.2
S-15	6.6	2	1	1	62	55	2262	62314	41.1	66.3
S-16	6.6	2	1	1	61	54	2329	65348	43.1	70.6
S-17	7.5	2.5	2.5	0	78	48	2760	70988	56.4	72.3
S-18	7.5	2.5	2	0	77	47	2723	71526	57.9	75.2
S-19	7.5	2.5	2	0	79	46	2794	74987	58.6	72.2

Where $P(\delta)$ is the instantaneous load corresponding to the instantaneous shortening δ. After each test the crush patterns were visually investigated. Generally position and length of the folds depend on tube material and geometry. For low d/t ratio and strain hardening material, tubes would generally deform in the axisymetric (concertina) mode whereas for high d/t ratio and/or a material sensitive to strain hardening, tube would generally deform in the non-axisymetric (diamond) mode. From Table 3.1 it can be seen that except few number of columns that have been crushed in axisymetric manner, combined axisymetric and diamond crush modes have been seen in the other of the tests. The first fold in all tubes (except test S-3) is axisymetric and it continued with axisymetric or non-axisymetric one. In this table N_s and N_d are the number of axisymetric and non-axisymetric lobes, respectively.

Figure 3.7 shows the crush patterns of tests (S-4) and (S-10). Here the axisymetric crush mode and combined axisymetric and non-axisymetric crush modes can be seen. An axisymetric lobe is the result of bending of tube wall first outward and second inward.

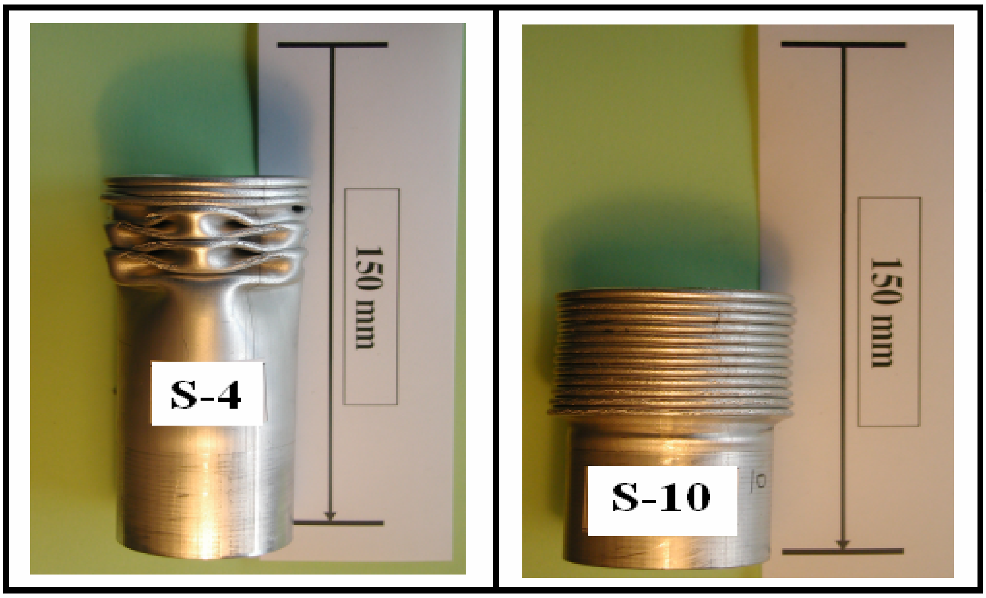

Figure 3.7: Combined axisymetric and non-axisymetric (left) and axisymetric (right) crush modes, AlMgSi0.5F22, ϕ40 mm

But the process of creation of one non-axisymetric lobe is quite different. In this mode the folds become triangular in shape having a base and an apex. Therefore, the wave length of diamond lobes generally is greater than concertina one.

For the finite element simulation, circular tubes with the dimension of experiment specimens are considered and because of symmetry, one half of tube is modeled with Belytschko-tsay thin shell elements. Symmetrical conditions are applied on all free vertical edges. The rigid impactor is modeled with solid elements.

Previously the effect of element size on computational results and CPU time was checked and results showed that using elements size of 3×3 mm have enough accuracy and acceptable computation expense [122]. In the finite element model the free length of the specimens is 151 mm. At the lower end, all degrees of freedom are fixed, while at the upper end the rotational degrees of freedom are fixed to avoid unrealistic deformation modes. The contact between the rigid impactor and the specimen is modeled using a node to surface algorithm with a friction coefficient of μ=0.2. To account for the contact between the tube walls during deformation, a single surface contact algorithm is used. The impact is imposed by modeling of free fall of a rigid block with the mass of 104.5 kg. In order to ensure that the impactor translate only in Z-direction and doesn't experience any rotation, nodal constraints are assigned to the nodes of rigid body. The aluminum alloy is modeled as an elastoplastic material using isotropic and kinematic work hardening with the use of material number #103 in the LS-DYNA. The strain hardening model used in this material model is described as

$$\sigma_e = \sigma_{0.2} + \alpha Q_1[1-\exp(-c_1\varepsilon_p)] + (1-\alpha)Q_2[1-\exp(-c_2\varepsilon_p)] + \sigma_v . \tag{3-12}$$

Here, $\sigma_{0.2}$ is the proportional limit in a uniaxial material test; $\varepsilon_p = \varepsilon - \sigma / E_t$ is the plastic strain; E_t is the elastic module of the tube material, c_i govern the rate of change in the isotropic and kinematic hardening variables, Q_i represent their asymptotic values, α determines the relationship between isotropic and kinematic hardening and σ_v is a viscous stress. Since the aluminum alloys are strain rate insensitive, the viscous effect is neglected. Tensile tests were performed to acquire material properties of the aluminum 6060 (AlMgSi0.5F22) alloy. Five tensile specimens were completed in accordance to ISO standard [49] and tested on an INSTRON tensile testing machine equipped with a 100 kN load cell at the Institute of Material Science of the Leibniz University of Hannover. The elongation of the specimens is measured using an extensometer. Data from the load cell and extensometer are acquired using a computer controlled data acquisition system. Load and extension measurements were recorded at a sampling rate of 5 Hz. The tests were conducted at a constant crosshead speed of 5 mm/min at room temperature. The typical engineering stress-strain curve of one representative 6060 tensile specimen is illustrated in Figure 3.8. The material constants $\sigma_{0.2}$, c_i and Q_i (i=1, 2) are determined based on the true stress-strain curve and presented in Table 3.2.

The crush load-displacement curve has oscillating behavior due to formation of the lobes. Numerical results of Berstadt et al. (1999) [14] have shown that this behavior is associated with loading and unloading of the material and that the relationship between isotropic and kinematic hardening may be important for the energy absorption. Therefore, analysis for different values of hardening parameter α was performed in [122].

Table 3.2: Material parameter of aluminum 6060 alloy

Parameter		Parameter	
$\sigma_{0.2}$ [Nmm^{-2}]	231		
c_1 [-]	735.1	c_2 [-]	13.46
Q_1 [Nmm^{-2}]	3.78	Q_2 [Nmm^{-2}]	60.93

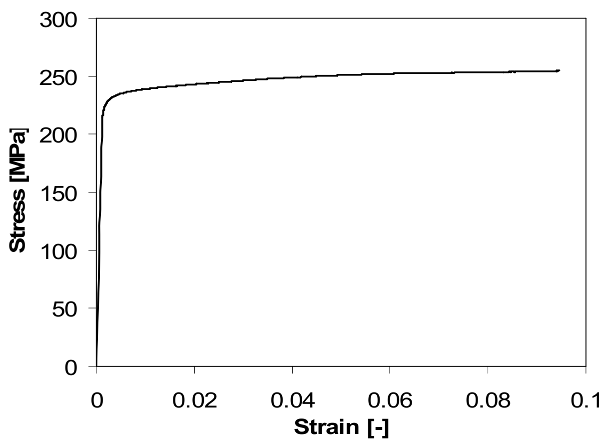

Figure 3.8: Typical stress-strain curve of aluminum 6060 alloy (AlMgSi0.5F22)

The results showed that the first peak load is not affected by hardening since there is not any unloading before the initial buckling load. Although there are some differences in the crush response of tube with different hardening parameters, the total energy absorptions for every value of α are more or less the same. Therefore, in this study the value $\alpha=1$ i.e. non-linear isotropic hardening is used. A comparison between experimental and numerical crush pattern of tube for two impact velocities (tests S-1 and S-8) are presented in Figure 3.9. It can be seen that the experiments can be covered by the simulations very good. The experimental and numerical crush load-displacement curves of impact with the velocity of 4.3 and 5.2 are presented in Figure 3.10 left and right, respectively. The exact match between the predicted and experimental curves is not achieved but the mean crush load and the energy absorption are predicted with satisfactory accuracy.

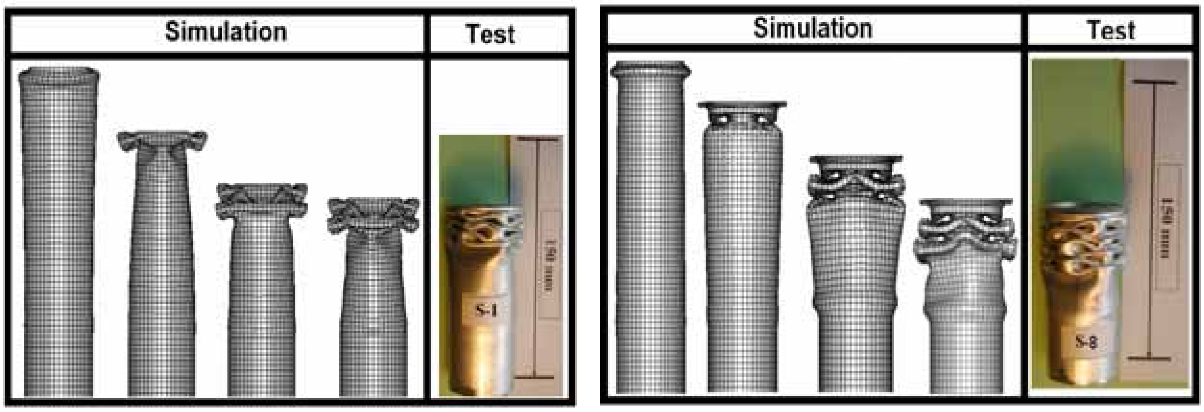

Figure 3.9: Comparison between experimental and numerical crush pattern of circular aluminum tubes, AlMgSi0.5F22, ϕ 40 mm

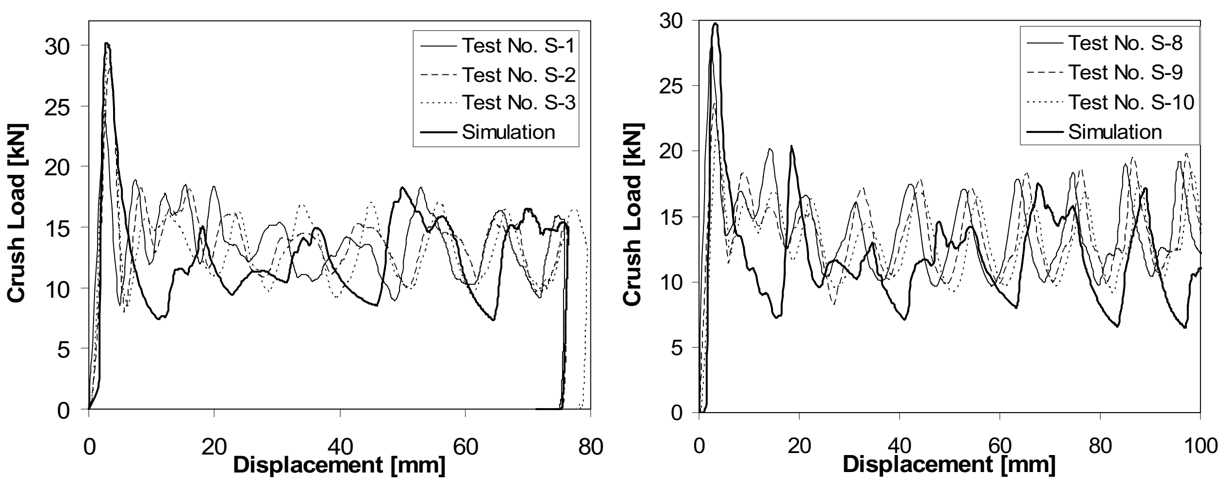

Figure 3.10: Comparison between experimental and numerical crush load-displacement curves of aluminum tubes, AlMgSi0.5F22, ϕ 40 mm

Higher crush load efficiency can be seen in the thicker tubes, see Table 3.1. The results of previously research showed that creation of simple groove at one end of the tube can improve the crush load efficiency up to more than 80% [122].

3.3 Crush performance of square aluminum tubes

Since the energy absorption of axially crushed square tubes depends so highly upon their collapse modes, the conditions governing the modes in which a tube will collapse are very important. Abramowicz and Jones (1997) [3] studied the role that material and geometric parameters of mild steel square tubes play in determining whether a tube will collapse in the global bending mode or in the progressive buckling mode. Tubes with a wide range of lengths, widths, and wall thicknesses were quasi statically crushed in order to determine their collapse modes. Their experimental results are summarized in Figure 3.11 in terms of the dimensionless parameters *l/d* and *d/t*, where *l* is the length of the tube, *d* is the width of the tube's sides, and *t* is the wall thickness. The star and sum symbols are the experimental results and the solid line in the figure approximately separates the experimentally determined progressive buckling and global bending regions. The region above the line represents geometries of tubes that collapse in the global bending mode and the region below the line represents geometries of tubes that collapse in the progressive buckling mode). Langseth et al. (1998) [61] conducted extensive research on the axial crushing of aluminum extrusions, suggested a critical length to width ratio of 3 for a stable (progressive buckling) collapse mode. For small width to thickness ratios, as are considered in this research, this value is in reasonable agreement with the experimental and theoretical results illustrated.

Similar to circular tubes, here the existing analytical formulations to predict crush response of square tubes are presented and compared with the experimental results. Simulation results are presented to find detail information about the crush phenomenon.

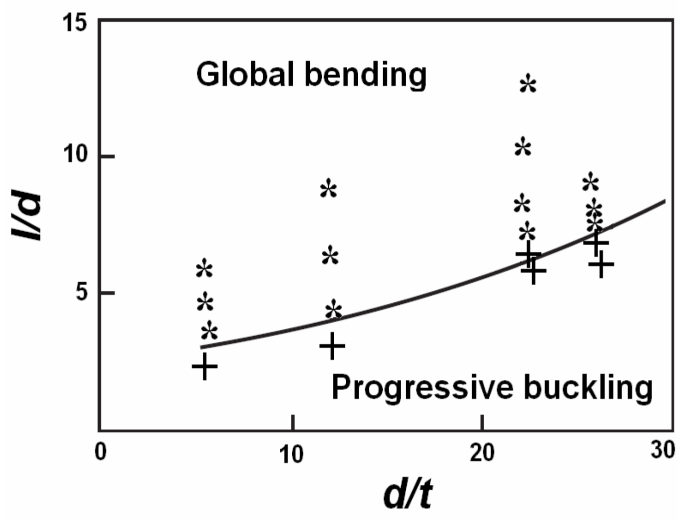

Figure 3.11: Design curve for square steel tubes, cp. [3]

3.3.1 Analytical investigations

The first step towards developing an analytical model for the crush collapse of square columns is the work carried out by Wierzbicki and Abramowicz (1983) [112]. They introduced their basic folding mechanism, based on the kinematic continuity, for symmetric collapse mode of the columns. In 1989 [4], they use a modified version of the theory to obtain a relation for the amount of energy dissipated by multi-corner sheet metal columns. Based on their model the expression for the mean crush load P_m and half wave length H are derived from the energy balance by equating the external work done by the crush load with energies dissipated in different types of deformation mechanisms as they occur in a folding process,

$$P_m = 38.27 M_0 C^{1/3} t^{-1/3}, \qquad H = 0.983 t^{1/3} C^{2/3}. \tag{3-13}$$

Where P_m is the mean crush force, M_0 the fully bending plastic moment, σ_0 is the flow stress, $C = 1/2\ (a+b)$ with a and b being the length of sides of a rectangular box column, and t its wall thickness. For a square tube, for which $C = d = b$, Equation (3-13) simplifies to

$$P_m = 13.06 t^{5/3} d^{1/3}. \tag{3-14}$$

The above model was validated by experimental results of Abramowicz (1983) [1] and Abramowicz and Jones [2] in 1984. Based on their experimental results the square tubes collapse either in symmetric or the mixed asymmetric collapse mode. The symmetric modes of deformation for square tubes have a layer with four individual lobes deforming, two opposite sides deforming inwards while the other two deforming outwards and vice versa. This should be contrasted with an asymmetric mode of deformation which has a layer with three individual sides deforming outwards and one inwards (associated with asymmetric mixed mode A), or two adjacent sides deforming outwards while the other two adjacent sides deforming inwards (associated with asymmetric mixed mode B). A transition from progressive axial buckling to global buckling could occur in a column if sufficient asymmetric lobes developed to produce instability. Here, it should be mentioned that a transition to global buckling may also develop following symmetric crushing. The symmetric crushing introduces deflections, or disturbances, into the uncrushed part of a column, which act as imperfections and can produce global buckling. Abramowicz and Jones (1984) [2] presented the following equations to predict the mean crush load and half wave length of asymmetric crush modes A and B

$$\frac{P_m}{M_0} = 33.05\left(\frac{d}{t}\right)^{0.33} + 2.44\left(\frac{d}{t}\right)^{0.66} + \pi/2, \quad \frac{H}{t} = 0.78\left(\frac{d}{t}\right)^{0.66}, \text{ for asymmetric mode A,} \tag{3-15}$$

$$\frac{P_m}{M_0} = 35.34\left(\frac{d}{t}\right)^{0.33} + 2.35\left(\frac{d}{t}\right)^{0.66} + \pi/4, \quad \frac{H}{t} = 0.86\left(\frac{d}{t}\right)^{0.66}, \text{ for asymmetric mode A.} \tag{3-16}$$

Table 3.3: Empirical relationship between structural effectiveness η_e and relative density ϕ for the collapse of various structures

Structure	$\eta_e = (\phi)$	ϕ
Cylindrical tubes	$2\phi^{0.7}$	4t/d
Square and rectangular tubes	$1.4\phi^{0.8}$	4t/c
Honeycomb	$5\phi^{0.9}$	8t/3c
Foam	$0.7\phi - 0.4\phi$	ρ_f / ρ_s

On the other side of the modeling spectrum are purely experimental approaches, see [63], [64] and [78]. Magee and Thornton (1978) [63] performed crash tests on several different section geometries and provided a relationship between structural effectiveness η_e of the section and relative density ϕ. The structural effectiveness is defined as the ratio of specific energy (maximum energy that can be dissipated, divided by specimen weight) to the specific ultimate strength (ultimate tensile strength divided by material density). Also, the relative density is defined as the ratio of material volume to the volume enclosed by the structural section. They then derived, by the way of curve fitting, a relationship between these two parameters. Table 3.3 summarized their relationships for different section geometries. The expression for mean crush load is

$$P_m = \eta \sigma_u \phi A_0 . \tag{3-17}$$

Where d is the diameter, ρ_f and ρ_s are the foam and base material densities, respectively, A_o is the overall area of the section and σ_u is the ultimate strength of the material. For a square section the mean crush load is

$$P_m = 17 \sigma_u t^{1.8} b^{0.2} . \tag{3-18}$$

A disadvantage of the above formulations given by Equations (3-13) to (3-18) is that the elasticity of the material does not come into play. Thus, for the same ultimate strength, materials like steel and aluminum would exhibit the same mean crush load. The test results of Mahmood and Paluszny (1984) [64] showed a considerable difference between the crush characteristics for these two materials. Mahmood and Paluszny (1981) [65] developed a quasi analytical approach that overcomes some of these drawbacks. They start with a premise that thin walled box columns, composed of plate elements and subjected to axial compression, will buckle locally when critical stress is reached. Local buckling initiates the processes that lead to the eventual collapse of the section and a subsequent folding of the column. The collapse strength of the section is related to its thickness/width (*t/d*) ratio and material properties.

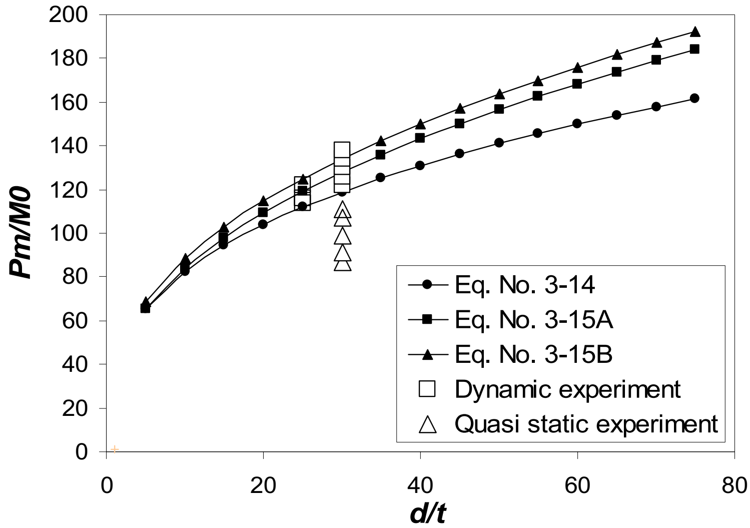

Figure 3.12: Comparison of present experimental results for crush load with different theoretical formulations for axisymetric lobes.

For very small *t/d* ratios *(t/d*=0.0085-0.016), which show asymmetric crush mode, they called these sections as "non-compact" sections, the mode of collapse of a section will be influenced predominantly by the geometry, since its local buckling strength is considerably below the material yield strength. For higher *t/d* ratios, typified as "compact" sections, in which the elastic buckling strength exceeds material yield strength, the material strength properties are expected to govern the mode of collapse and, consequently, the post-buckling stability. The collapse mode in this case will appear very stable even in the presence of considerable geometry or loading imperfections (symmetric crush mode). Since the "compactness" of an axially compressed column affects the stability of collapse, it is important to define when a section becomes "noncompact" and fails in a crumbling mode. According to Mahmood and Paluszny (1982) [66] the threshold $(t/d)^*$ ratio is given by

$$(t/d)^* < 0.48[\sigma_y(1-\upsilon^2)/E_t]^{1/2}. \tag{3-19}$$

Here, E_t is the Young's modulus of elasticity and υ the Poisson's ratio. Figure 3.12 shows the test results for P_m/M_0 compared with theoretical equations. Here, except the result of quasi-static crash tests which are below the curves, the dynamic test results are close to the Equations (3-14) and (3-15).

3.3.2 Experimental and numerical results

Quasi-static and dynamic crash tests were conducted on aluminum 6060 alloy square tubes. The outer width of the aluminum tubes are 55 and 60 mm, while the nominal wall thickness is 2 mm. In the case of quasi-static tests, the square tubes with the length of 120 and 240 mm were compressed by INSTRON tensile testing machine at the Institute of Material Science of the Leibniz University of Hannover. Simply support boundary condition is applied for quasi-static tests. For the dynamic tests 270 mm long tubes are used and the lower end of tubes is fixed by means of special steel clamps that embedded a distance of 30 mm outside of the tubes and close fitting steel inserts are placed inside the end of the tube over the same length of external fixture for fixing to the periphery of the specimens. To investigate the crush performance of the tubes in non axial impact conditions, in some dynamic tests, the impact angles θ are set to 5 and 10 degree. After each test, the data were filtered and then the load-displacement curves were plotted. The values correspond to the first peak is maximum crush force P_{max} and the area under this curve is absorbed energy E. The mean crushing load P_m from the experimental results is defined by equation (3-11). The results of visual inspection of the crush modes *CM* showed that all tubes crush in symmetric manner.

Table 3.4 summarized the results of experimental tests. Here, quasi-static test numbers (S-20), (S-21) and (S-22) corresponds to the tube with the length of 120 mm and the tube length in test numbers (S-23), (S-24) and (S-25) are 240 mm, cp. [123]. Here, it should be mentioned that the maximum axial deformation distance which laser displacement sensor can measure is 160 mm.

For the finite element simulation, square tubes with the dimension of experiment specimens are considered. Because of symmetry in axial impact test, only half of the tube is modeled with Belytschko-tsay thin shell elements. Symmetrical conditions are applied on all free vertical edges. The effect of element size on computational results and CPU time has been checked and elements size of 3×3 mm showed reasonable result. At the lower end all degrees of freedom are fixed. The contact between the rigid impactor and the specimen is modeled using a node to surface algorithm with a friction coefficient of μ=0.2. To account for the contact between the tube walls during deformation a single surface contact algorithm is used. The impact is imposed by modeling of free fall of a rigid block with the mass of 104.5 kg. In order to ensure that the impactor translate only in Z-direction and don't experience any rotation, nodal constraints are assigned to the nodes of the rigid body. As initial geometrical imperfections influence the peak loads a great deal, initial imperfections are prescribed along the length of model in the analyses with following expression

$$W = w_0 \sin(n\pi x / l). \tag{3-20}$$

Here, w_0 is the amplitude and n is the number of half-sine waves along the tube length. In these simulations the parameters are defined by w_0 = 0.1 mm and n = 5. To ensure quasi-static loading when using explicit code, the rigid body is given a prescribed velocity field $V(t)$,

$$V(t) = \frac{\pi}{\pi - 2} \frac{S_{\max}}{T} \left[1 - \cos\left(\frac{\pi}{2T} t \right) \right]. \tag{3-21}$$

T is the total duration of the loading, and S_{max} is the final crush displacement of the tube, cp. [89]. Simulations of the quasi-static tests show that the total kinetic energy is very small

Table 3.4: Experimental crash response of square aluminum tubes AlMgSi0.5F22

Test No.	V [m/s]]	d [mm]	θ [degree]	CM [-]	N_s [-]	P_{max} [kN]	S_{max} [mm]	P_m [MPa]	η [%]
S-20	-	60	0	S	2	93.8	92.9	21	22.6
S-21	-	60	0	S	2	93.8	96.2	22	23.5
S-22	-	60	0	S	2	93.6	96.4	24	25.6
S-23	-	60	0	S	4	91.9	190.7	27	29.4
S-24	-	60	0	S	4	93.7	192.9	26	28.0
S-25	-	60	0	S	4	92.5	186.8	26	28.1
S-26	5.5	60	0	S	2.5	59.1	84.5	31	52.5
S-27	5.5	60	0	S	2.5	75.5	87.9	33	43.7
S-28	5.5	60	0	S	3	58.4	98.6	32	54.8
S-29	7.5	60	0	S	3.5	69.2	130.5	34	49.1
S-30	7.5	60	0	S	3.5	67.1	128.9	34	50.7
S-31	8.6	60	0	S	4	66.7	>160	35	52.3
S-32	8.6	60	0	S	4.5	65.1	>160	33	50.7
S-33	8.6	60	0	S	4	71.3	>160	34	47.7
S-34	9.0	60	0	S	4.5	70.3	>160	34	48.4
S-35	9.2	60	0	S	4.5	69.4	>160	33	47.6
S-36	9.2	60	0	S	4.5	71.3	>160	34	47.9
S-37	6.9	55	0	S	3.5	63.9	>160	30	37.6
S-38	7.0	55	0	S	4	633	>160	29	36.3
S-39	7.0	55	0	S	4	68.1	>160	29	36.7
S-40	8.6	55	0	S	4	69.1	>160	31	39.1
S-41	8.7	55	0	S	4	63.6	>160	30	37.7
S-42	7.5	60	5	S	3.5	48.1	>160	28	58.2
S-43	7.6	60	5	S	3.5	47.3	>160	27	57.1
S-44	4.8	60	5	S	2.5	47.3	69.9	28	59.2
S-45	5.0	60	5	S	2.5	45.8	84.6	27	60.0
S-46	4.8	60	5	S	2.5	46.5	79.7	27	58.1
S-47	5.7	60	5	S	3	46.2	111.3	28	60.6
S-48	5.8	60	5	S	3	47.1	111.4	29	61.6
S-49	5.7	60	5	S	3	45.57	109.0	27	59.3
S-50	7.1	55	5	S	4	39.6	>160	26	65.7
S-51	7.1	55	5	S	4	40.3	>160	25	62.0
S-52	5.6	60	10	S	2.5	41.3	101.5	25	60.5
S-53	5.6	60	10	S	3	40.2	115.1	25	62.2
S-54	5.6	60	10	S	2.5	43.1	98.2	26	60.3
S-55	7.5	60	10	S	3.5	43.2	154.1	26	60.6
S-56	7.5	60	10	S	3.5	45.1	148.3	26	53.7
S-57	7.1	55	10	S	3.5	38.0	>160	25	65.9
S-58	6.9	55	10	S	3.5	41.4	>160	25	60.4

compared to the total internal energy over the period of the crushing process, which shows that inertia effects are negligible. In explicit finite element method, the time step usually is selected very small to maintain numerical stability. However, small step size prevents this method from being useful for routine analysis work like quasi-static crush process. Since in the explicit method the time step size is related directly to the elements density, one way to use this method for quasi-static problem efficiently is to scale up the mass, while keeping the velocity very low. Scaling up the mass results in a large time step, therefore, reducing the number of time steps increments and in addition the velocity up to 1000 times of original velocity can be used in simulation. The aluminum alloy is modeled as an elastoplastic material using isotropic and kinematic work hardening with the use of material model presented by equation (3-12). Figure 3.13 shows the experimental and simulated crush patterns of test (S-23) and crush load-displacement curves of the quasi-static tests (S-23) to (S-25). The results of axial dynamic tests (S-29) and (S-37) are presented in Figure 3.14. Also the same results for the dynamic oblique tests (S-42) and (S-55) are shown in Figure 3-15. As one can see the deformation mode is well described by the simulations. A quick observation on numerical crush load displacement curves will indicate that the mean crush load in the simulation curve is a little higher than experimental results. This shows that the imperfection model presented in Equation (3-20) is not quite accurate to model real imperfection of the tubes. Therefore, the final crush displacement is smaller than the experimental one.

Langset and Hopperstad (1996) [60] reported an increase of the mean crush load of aluminum tubes when subjected to dynamic loading compared to the quasi-static case. Since aluminum shows little strain rate sensitivity, they concluded that this effect is due to the inertia forces arising from the acceleration of the extrusion walls introduced by the dynamic loading. Here, also it can be seen in the Table 3.4 that as a result of inertia effect, the mean crush loads in dynamic tests are higher than the quasi-static one. From Figures 3.14 for the axial tests and Figure 3.15 for the oblique ones, it can be recognized that the load angle has dramatic influence on the first peak load. In the case of axial impact the curve starts with high peak load that corresponds to elastic-plastic buckling of tube and continues with a repeated pattern. Each pair of peaks is associated with the creating of one lobe. If the impact has been generated with an angle greater than zero, the first maximum load corresponds to the creation of the first lobe and in continue the load values oscillate around the mean crush load. The impact angle has influence on mean crush load as well. When the impact angle increases the mean crush load decreases.

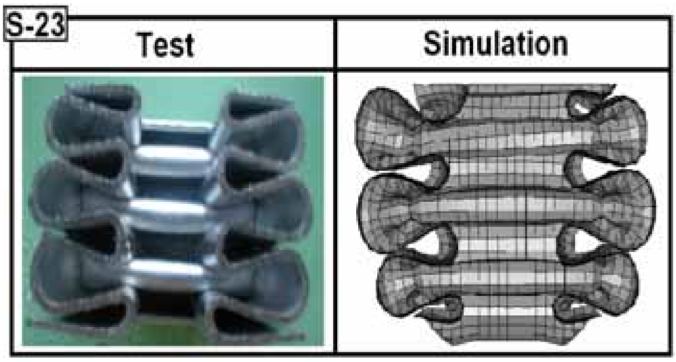

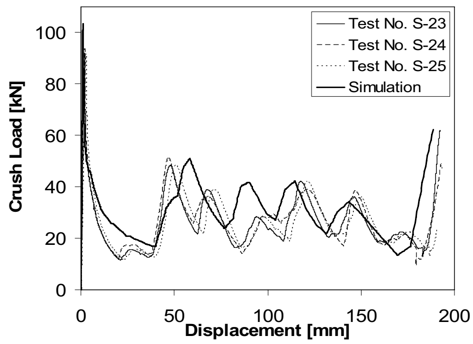

Figure 3.13: Comparison between quasi-static experimental and numerical crush patterns (left) and crush load-displacement curves (right)

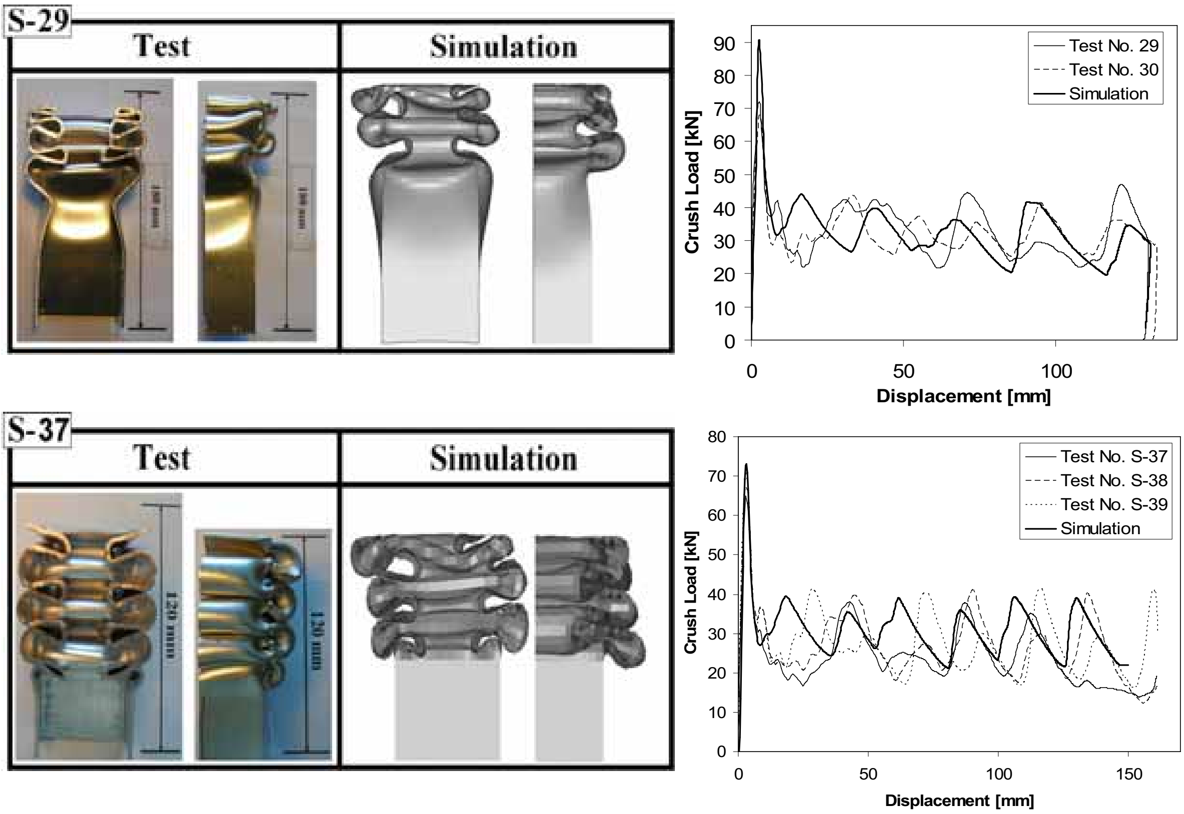

Figure 3.14: Comparison between dynamic experimental and numerical crush patterns (left) and crush load-displacement curves (right), impact angle S-29: 0^o and S-37: 0^o

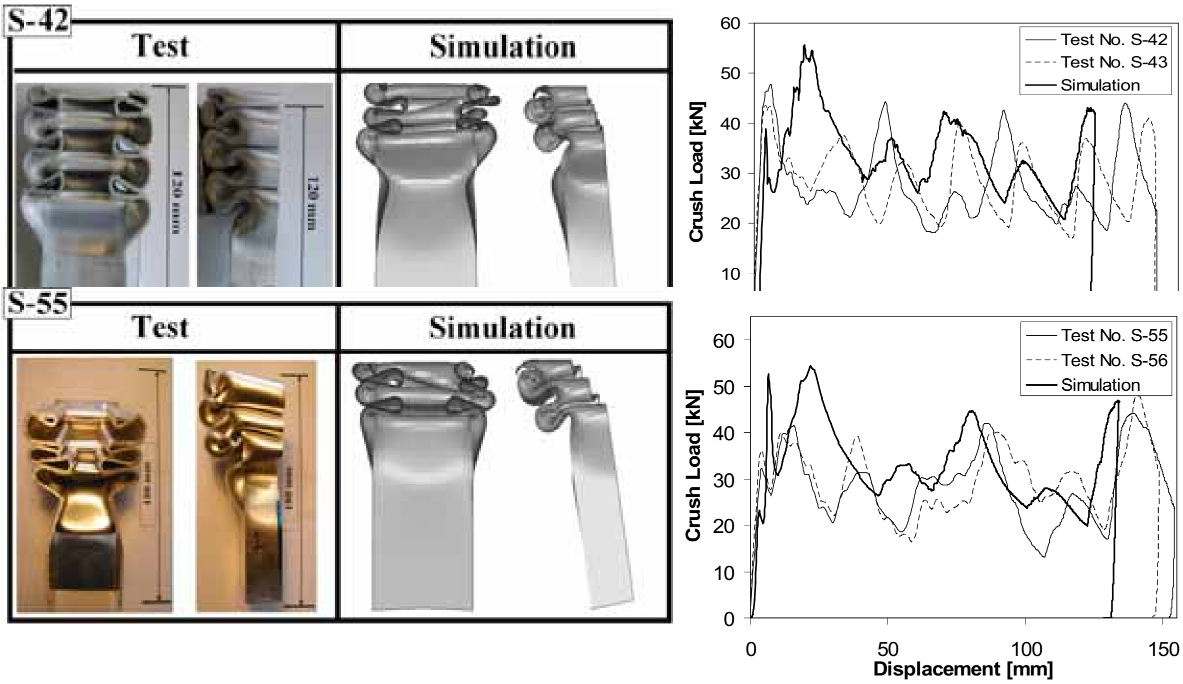

Figure 3.15: Comparison between dynamic experimental and numerical crush patterns (left) and crush load-displacement curves (right), impact angle S-42: 5^o and S-55: 10^o

3.4 Multi design optimization of crush behavior of aluminum tubes

There are high interests in vehicle industry to use commercial tube like circular, rectangular and square shapes as a crash box and save production cost. The comparison between specific energy absorption capabilities of the mentioned three categories of aluminum tubes showed that the specific energy absorption of the tubes follow the order: circular> square> rectangle [124]. Therefore, in this research the crashworthiness optimization procedure is used to find optimum square and circular aluminum tubes for crash absorption applications. Similar optimization procedure which was previously used to find optimum thicknesses of the vehicle frontal components, see section 2.7, is used here to find optimum tube geometry. Though lots of optimization studies deal with only one objective, these approaches are often not realistic for industrial applications. More and more real-life cases need several objectives to be handled simultaneously, for instance minimizing both the mass and cost of a mechanical structure. Yamazaki and Han (1998) [115] used crashworthiness maximization techniques for tubular structures. Based upon numerical analyses, the crush responses of tubes were determined and a response surface approximation method *RSM*, was applied to construct an approximative design subproblems. The optimization technique has been applied to maximize the absorbed energy of cylindrical and square tubes subjected to impact crash load. For a given impact velocity and material, the dimensions of the tube such as thickness and radius are optimized under the constraints of tube mass as well as the allowable limit of the axial impact force.

The implementation of the multi design optimization technique *MDO* in crashworthiness improvement of aluminum tube was examined previously [125]. Finite element simulation was used to find the crush response of the tubes. The approximative subproblems were constructed with the use of response surface method and finally the weighed sum method, the most popular method in the evolutionary algorithm community and also among design engineers, was used to find the optimum solution. In this method the *m* objective functions are aggregated into one,

$$f(x) = \sum_{i=1}^{m} W_i f_i(x) \tag{3-22}$$

Where the weights w_i are such that

$$\sum_{1}^{m} w_i = 1. \tag{3-23}$$

Therefore, the multiobjective problem is transformed into a single-objective problem. After replacing the optimization problem by a series of simpler approximative subproblems, the optimization algorithm that is provided in MATLAB was utilized to solve the subproblems. The *MDO* procedure is implemented here to find optimum circular and square aluminum tubes. The tube thickness *t*, diameter/width *d* and length *l* are considered as optimization parameters. The goal is to find the optimum circular and square tube that absorb maximum energy while has minimum weight. The general optimization procedure presented in

Figure 2.8 is used. In this procedure after replacing the optimization problem by a series of simpler approximative subproblems which can be constructed by using *RSM*, the subproblems can be solved by a conventional optimization method. The first step in the construction of an approximate function by *RSM* is to assume its form. This information is needed to select enough points to create the approximation efficiently. Every point is the result of one numerical simulation. In order to reduce the CPU cost in this approach, the D-optimality design of experiments method was used. This method reduces the number of required points for the construction of approximate functions.

The finite element method is used to calculate the absorbed energy and specific energy absorption of the tubes. The design variables are the thicknesses, lenght and the cross sections geometries of the tubes. The impact force constraint is usually required to reduce the occupant injury when passenger vehicles are considered. Therefore, in the optimization process, the mean crush load P_m should not exceed the allowable limit P_{ma} i.e.

$$g = P_m / P_{ma} \leq 1. \tag{3-24}$$

Where the value of P_{ma}=40 kN is selected in this research.

The above mentioned optimization system is applied to the maximization of absorbed energy *E* and specific absorbed energy *SAE* of the tube under axial impact load. Since the interest is to find the crush behavior of tubes up to the final effective crush length, all tubes are encountered with a large amount of impact energy. It should be mentioned that 75 percent of the tube length is considered as effective deformation length.

Table 3.5 shows the optimum results of square and circular tube. Comparison between optimized results indicate that the optimum square and circular tubes absorbed more or less the same energy but the specific energy absorption of circular tube is about 10 percent higher than square one. The optimization results proved that reducing the tube width/diameter or increasing the tube thickness can increase the crash efficiency of the tube. In addition it can be recognized that if the tube crushes in progressive mode it absorbs the impact energy efficiently. However, reducing the tube width/diameter or increasing the tube thickness will make the tube become longer and thicker. This raises the possibility that the tube deform into the global buckling mode which absorbs not much energy.

Another important factor that should be considered is the crush behavior of the tube in oblique impact condition. In oblique impact condition, not only the tube should have a good resistance against axial crash load but also reasonable bending resistance is expected. The bending resistance of tubes is directly related to the tube geometry. Reduction of the tube width/diameter reduces the bending strength of the tubes as well. Therefore, in practical application the tube with the cross section values as presented in Table 3.5 cannot be used as a vehicle crash box. They have good resistance in axial direction but very weak bending behavior. As mentioned before, the optimum circular tube has higher (9.8 %) specific energy absorption than square tube but on the other hand the optimum square tube has higher bending resistance (10.4%) than the circular one. With the above understanding, here the geometrical restrictions in designing aluminum tubes as a crash box are changed. In the new optimization procedure the tube width/diameter is not allowed to be smaller than d=70 mm. To avoid global buckling the maximum allowed tube length to diameter/width ratio l/d is set equal 3 based on experimental observations [61], [39], [40]. In order to prevent damage to the rest of the structure behind crash boxes (front rail) the maximum crush load is not allowed to be higher than P_{max}=85 kN. Previous research showed that by creating simple groove in one end of the tube, the high maximum crush load levels can be overcome [122]. They used the optimization procedure to find optimum groove geometry and its position along of the tube length that minimizes the maximum crush load while the mean crush load remains more or less unchanged. Here, the purposed groove is created at the top end of the tubes.

Finally, the *MDO* procedure is applied to maximize the energy absorption and specific energy absorption of the tubes with square and circular cross sections. The absorbed energy, the specific absorbed energy and the mean crush load are approximated as non-linear second order polynomials. Then the approximative subproblems are solved by genetic algorithm optimization method [75]. The allowable mean crush load P_{ma} is set to 68.5 kN as purposed by other researchers [71], [115]. Table 3.6 shows the optimized tube geometry and its energy absorption characteristics. Here η is the crush load efficiency, and S_E is the stroke efficiency, the ratio between the crush length at which the densification takes place (effective crush length) and the total tube length. Higher values of these parameters indicate more efficient tubes. This table shows that the optimum circular tube absorbs about 6 percent more energy than optimum square tubes and has about 23 percent lower weight.

Table 3.5: Optimum circular and square aluminum tubes AlMgSi0.5F22

Tube Type	Design Domain [mm]	t [mm	d [mm]	l [mm]	E [J]	SEA [J / kg]
Square	$1<t<4$ & $20<d<120$ & $50<l<300$	2.31	29.8	300	8591	55677
Circular	$1<t<4$ & $20<d<120$ & $50<l<300$	2.27	34.4	300	8522	61221

Table 3.6: New optimum circular and square empty tubes AlMgSi0.5F22

Tube Type	t [mm]	D [mm]	L [mm]	E [J]	Increase [%]	SEA [J / kg]	Increase [%]	η [%]	S_E [%]
Square	2.1	70	210	7602	-	26124		53	84
Circular	1.95	70	210	8087	6.0	33880	22.9	61	87

4. Crush performance investigation and optimization of filled aluminum tubes

4.1 Introduction to the crashworthiness investigation of filled tubes

Cellular solids are increasingly used in many engineering applications like energy absorption, thermal insulation and lightweight structures due to their unique property of high porosity. For light weight crash box or bumper beam designs, low density metal fillers, such as aluminum honeycomb or foam, are preferred to tube with thicker tube walls in terms of achieving the same energy absorption. Metal fillers are able to increase the energy absorption of a thin- walled column. This increase is the result of the large compressive deformation of the filler. The investigations indicated that the interaction between filler and tube walls produces some worthwhile crush characteristics and energy absorption properties. The mean crushing loads of filled tubes are found to be higher than the sum of the crushing loads of foam alone and tube alone. In this chapter the strengthening effect of metal filler in aluminum tubes is investigated. A series of experimental and numerical efforts are done to determine and optimize the crush behavior of the filled aluminum tubes. Also the existing analytical formulations are summarized.

4.2 Crush performance investigation of the foam-filled aluminum tubes

Metallic foams can be made by a number of novel processes. Open cell metallic foams can be made using open cell polymer foams as a form. The voids of the polymer foam are filled with a heat resistant material such as plaster, the polymer is burned off and molten metal is cast into the resulting form. Finally, the heat resistant material is removed. Closed cell metallic foams can be produced by several methods. They can be made by injecting gas into a mixture of molten aluminum and either silicon carbide or alumina particles which stabilize the bubbles in the melt. The resulting foam is conveyed off the surface of the melt and allowed to cool. Metallic foams can also be made by using a chemical blowing agent which decomposes to form a gas. For instance, titanium hydride decomposes to give off hydrogen gas at 400 centigrade; it can be used as a blowing agent for aluminum (melting point of 660 centigrade). The foam which is used in this study, trade named Alporas, is made by first mixing calcium into the molten aluminum to increase viscosity, then introducing titanium hydride which separates into titanium and hydrogen. The titanium mixes with the aluminum alloy and the hydrogen causes foaming of the molten mixture which is responsible for creating the porous aluminum foam [6]. Powder technology also is used to produce aluminum foam. In this process, powdered titanium hydride and powdered aluminum are mixed, pressed and then heated to release the hydrogen gas [12], [13].

Figure 4.1 shows the deformation curves of cellular metal foams under the compression and tension loads. Here, the compressive behavior is characterized into three stages, which apply to three distinct regions on the stress-strain curve. The first region, is the ‘‘elastic’’ region. After the peak stress is reached a constant plateau occurs, where small but distinguishable peaks and valleys are recognized. The constant stress plateau continues up to large strains of the order of 50-60%. Then the stress increases as the material becomes denser, comparable to base metal. The tensile stress-strain curve of aluminum foams shows initial linear elasticity followed by a brief nonlinear region which is terminated by fracture at strains of roughly 0.2±0.2% [33], [62], [106].

The studies of the mechanical properties of the foams have shown that the linear elastic response is related to cell edge bending in open-cell foams and to edge bending and face stretching in closed-cell foams. As the stress increases, the cells begin to collapse at a roughly constant load by elastic buckling, yielding or fracture, depending on the nature of the cell walls material. Once all of the cells have collapsed further deformation presses opposing cell walls against each other, increasing the stress sharply. This final regime is referred as densification. The area under the compression curve is the energy that can be absorbed by the foam. As can be seen it approximates an ideal absorber, in that it attains the maximum value quickly, and maintains this value over a very large deformation. The other very interesting observation from the compression response of foams is that foams exhibit very little lateral bulging during compression. There is a significant reduction in volume during compression. In fact, many foams exhibit a plastic Poisson's ratio of near zero [33].

As mentioned before, aluminum foams have many superior properties such as sound absorption, impact energy absorption and heat isolation, etc. All these properties are sensitive to the macroscopic cellular structure of the foam.

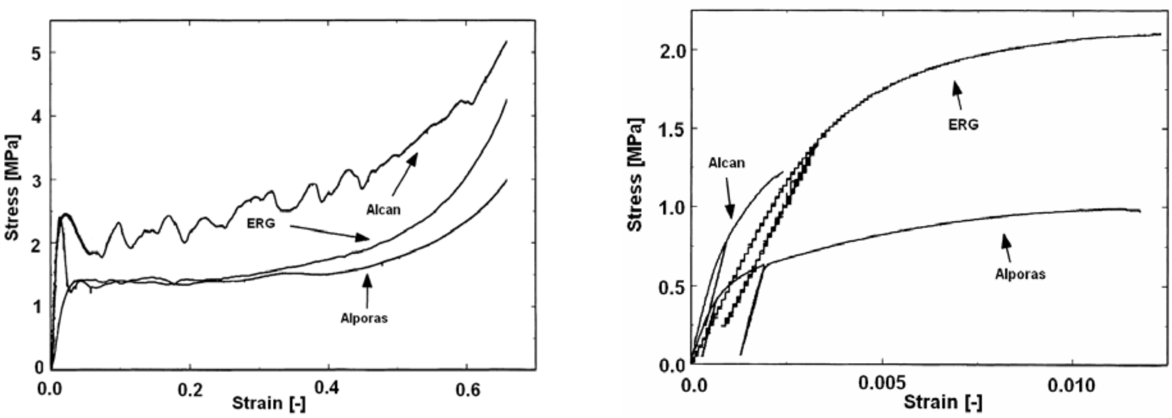

Figure 4.1: Stress-strain behavior of aluminum foam under compression (left) and tension (right), cp. [33]

Here, the strengthening effect of the aluminum foam in the vehicle crash box is investigated. First the analytical point of view is summarized. Several axial and oblique impact tests are generated on foam-filled tubes and to find details about the crush process the finite element method is used.

4.2.1 Analytical investigations

Gibson and Ashby (2000) [33] conducted a significant amount of work on the mechanical behavior of cellular structures. They have shown that the mechanical properties of cellular materials are heavily dependent on the relative density of them. Generally, the properties of foam follow a power law. For the elastic regime the relative young's modulus of the closed cell foam to the base material can be written as

$$\frac{E_f}{E_s} = C_{f1}\phi_f^2\left(\frac{\rho_f}{\rho_s}\right)^2 + C_{f1}^*(1-\phi_f)\left(\frac{\rho_f}{\rho_s}\right). \tag{4-1}$$

Where the ρ_f / ρ_s is the ratio of the foam density to the base material density, ϕ_f is volume fraction of the solid in the cell edges, C_{f1} and C^*_{f1} are the material constants. Finite element analysis of a unite cell of a closed-cell foam suggests that $C_{f1}= C^*_{f1} =0.31$ [101]. For isotropic closed cell foams it is expected the shear modulus to be about 3/8 the value of the elastic Young's modulus and the elastic Poisson's ratio to be about one-third [33]. Foams fail when the cell walls yield, either by the formation of plastic hinges in the bent cell edges of open-cell foams or by the uniaxial yield of the cell walls in ideal closed-cell foams. The uniaxial compressive strength, or plastic collapse strength, σ_f can be expressed as

$$\frac{\sigma_f}{\sigma_{ys}} = C_{f2}\left(\phi_f\frac{\rho_f}{\rho_s}\right)^{3/2} + C_{f2}^*(1-\phi_f)\left(\frac{\rho_f}{\rho_s}\right). \tag{4-2}$$

Where σ_{ys} is the yield stress of the base material, C_{f2} and C^*_{f2} are material constants. Finite element analysis of a unite cell of a closed-cell foam suggests that that $C_{f2}= 0.3$ and $C^*_{f2} =0.4$ [101].

At the end of the stress plateau, the stress rises sharply with increasing strain, corresponding to complete cell collapse; further strain loads opposing cell walls against another, increasing the stress sharply. The densification strain ε_D at which this occurs, decreases with increasing relative density according to [10]

$$\varepsilon_D = 0.8 - 1.75\left(\frac{\rho_f}{\rho_s}\right). \tag{4-3}$$

Reid et al. (1986) [81] performed a comprehensive experimental study on the crushing behavior of square foam-filled columns under quasi-static and dynamic loading. It was discerned that the interaction between foam and outer skin may play an important role in the process of tube crushing. A theoretical analysis of the problem was also performed, but the interaction between the structure and foam was not accounted. Their work was extended by Abramowicz and Wierzbicki (1988) [5]. They analyzed closed cell foam with a model consisting of a packed lattice of small and large cells. The structure of the closed cell foam was approximated as regular and symmetric unit cells assembled from a truncated cube section. The mean crushing load P_m of the basic folding element of truncated cube models was derived as

$$P_m = 4.43\sigma_{0f}\ t_f^{3/2} d_f^{1/2}. \tag{4-4}$$

Where d_f and t_f are cube wall width and thickness, respectively and σ_{0f} is the flow stress of the foam material. The crushing resistance of the truncated cube model is defined by ratio of the mean crushing load to the tributary area of the basic folding element. Thus, the crushing strength of a foam structure based on the truncated cube model is

$$\sigma_f = 5.87\sigma_{0f}\ (t_f / d_f)^{3/2}. \tag{4-5}$$

From the geometrical relationship of the truncated cube model, the thickness to width ratio is related to the solidity ratio as t_f / d_f=3.1(ρ_f / ρ_s). Therefore, in terms of solidity ratio, the crushing strength of a closed cell foam structure can be written as

$$\sigma_f = 1.05\sigma_{0f}\ (\rho_f / \rho_f)^{3/2}. \tag{4-6}$$

Then the mean crushing load of a foam-filled square column can be calculated approximately by adding the resistance of an empty tube, Equation 3-14, to foam filler,

$$P_m = 13.06\sigma_0\ t^{5/3} d^{1/3} + d_f^2 \sigma_f. \tag{4-7}$$

Hanssen et al. (1999) [39] conducted quasi-static crushing of square AA6060-T4 and AA6082-T4 aluminum extrusions with foam densities of 0.15-0.50 g/cm^3. Tubes with widths of 60-80 mm were used with 41≤ d/t ≤80. They explored both bonded and unbonded specimens. They found that the foam filling increased the number of lobes formed during crush and that the number of lobes was a function of foam density. They also found that bonding the foam could cause an increase of 64.5% in the specific energy absorption. However, many of the higher strength AA6082 specimens ruptured with lower energy absorption. They reported that strict requirements are needed to be placed on the properties of the extrusion material if bonding is to be used. They developed an empirical relationship based on the experimental results for foam-filled square columns, given by

$$P_m = 13.06\sigma_0\ t^{5/3} d^{1/3} + d_f^2 \sigma_f + C_{avg}\sqrt{\sigma_f \sigma_0}\,td. \tag{4-8}$$

Here, the first term represents the experimental crush load for an empty column, the second term is the uniaxial contribution of the foam filling, and the last term accounts for the interaction effect. The coefficient C_{avg} is the interaction constant and has to be calibrated from the experiments. They used the experimental results of hydro aluminum foam-filled columns and purposed the value of 5.5 for the interaction constant. Later, Hanssen et al. (2000) [40] expanded their previous work by conducting work on the collapse response of foam-filled aluminum columns subject to dynamic impact loading. The ratios of the dynamic to quasi-static mean crush loads for the empty columns tested were significant, but were usually found to be only approximately 1.1 for the foam-filled columns. Figure 4.2 compares the experimental and analytical crush strength of the foam-filled column. The tube thickness is 2 mm and foam density is varies between 50-500 kg/m^3. It shows that the Equation (4-7) gives a little underestimated prediction. Equation (4-8) which accounts the interaction effect gives acceptable agreement with the experiments if the value of 1.4 selected for interaction effect coefficient C_{avg}. The correlation between the Gibson and Ashby prediction, Equation (4-2), and the experimental data is good if the volume fraction of the solid in the cell edges is assumed to be 0.15.

4.2.2 Experimental and numerical results

A closed cell aluminum foam Alporas with a relative density of 0.085 is used in this study. The Alporas aluminum foam is manufactured by the Shinko Wire Company. The foam is produced as sheets with a nominal thickness of 50 mm. Dynamic compression tests were conducted on foam-filled aluminum square tubes. The outer width of the aluminum square tubes is 55 mm, while the nominal wall thickness is 2 mm. Dynamic tests were done in drop weight test rig, Figure 3.5. Simply support boundary conditions are applied in quasi-static tests. Here, 270 mm long tubes are used and the lower end of tubes is fixed by means of special steel clamps that embedded a distance of 30 mm outside of the tubes and close fitting steel inserts are placed inside the end of the tube over the same length for fixing the specimens.

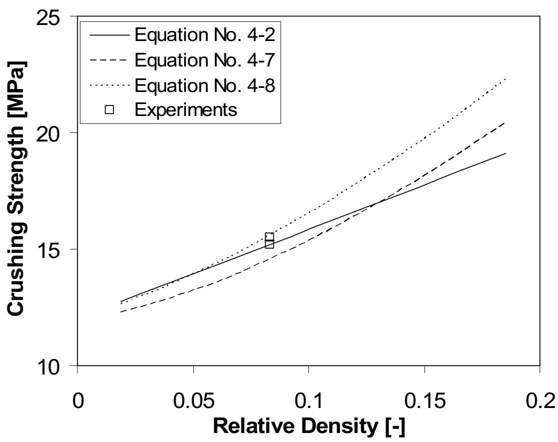

Figure 4.2: Comparison between the analytical expression and experimental results of aluminum square tube AlMgSi0.5F22 D 55 mm×2 mm with Alporas foam

To investigate the crush performance of the tubes in non axial impact conditions, some oblique tests, θ=5 and 10 degree, were performed. The results of visual inspections of the crush modes *CM* show that all tubes have been crushed in symmetric manner. Table 4.1 summarizes the results of experimental tests.

From Figure 4.3 it can be seen that the recorded force level of the foam-filled tube (Test F-1) is some what higher than that of the combined effect of the empty tube (Test S-38) and the foam alone. This increase is the result of the interaction between the tube walls and the foam during the crush process. In this figure the shaded area is the increase of energy absorption due to the interaction effect.

Numerical simulations of crash tests are performed to obtain detail investigation of the crush performance of the tube. The modeling and analysis is performed on a UNIX server using the explicit finite element code LS-DYNA.

In the simulations, the dimension of the tested foam-filled square tubes is considered. Because of the symmetry in axial tests, only one half of the specimen is modeled. The column walls are modeled with the Belytschko-Tsay thin shell elements. The foam filler is modeled with solid elements and symmetrical boundary conditions are applied on all free vertical edges. Rigid body elements are used to model the impactor. Initial imperfections are prescribed along the length of tube, like empty tube simulations. The contact between the rigid body and the specimen is modeled using a node to surface algorithm with a friction coefficient of $\mu = 0.2$. To account for the self contact between the tube walls during deformation, a single surface contact algorithm is used. The node to surface contact is implemented between tube walls and foam filler. The aluminum foam is modeled with the foam model of Dehspande and Fleck material number #154 in LS-DYNA [19]. In this model the foam is considered as an isotropic material. The following yield criterion is assumed for this model

$$\varphi = \hat{\sigma} - Y \leq 0, \qquad (4\text{-}9)$$

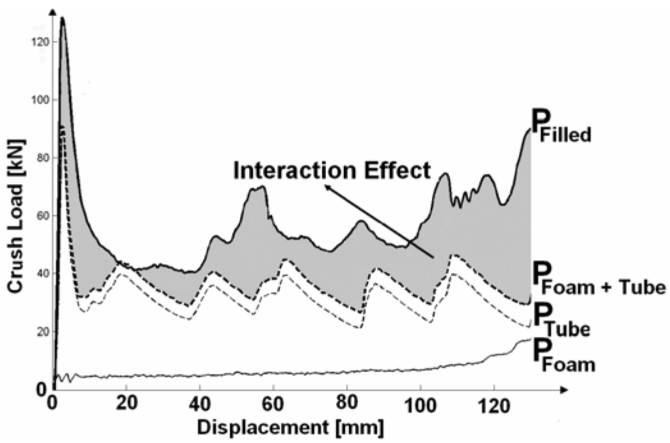

Figure 4.3: Interaction effect in the foam-filled tube

Table 4.1: Experimental result of crash test on foam-filled aluminum tubes D55 mm×2 mm AlMgSi0.5F22 and Alporas aluminum foam with the relative density of 0.085

Test No.	V [m/s]	d [mm]	θ [degree]	CM [-]	N_s [-]	P_{max} [kN]	S_{max} [mm]	P_m [MPa]	η [%]
F-1	6.9	55	0	S	3.5	67	106	36	53.7
F-2	7.0	55	0	S	3.5	66.8	104	36	53.9
F-3	8.7	55	0	S	4	66.8	150	37	55.4
F-4	8.7	55	0	S	4	65	139	36	55.4
F-5	8.6	55	0	S	4	68.7	144	36	52.4
F-6	9.9	55	0	S	5	79.2	160	36	45.5
F-7	9.9	55	0	S	5	72.1	160	36	49.9
F-8	7.0	55	5	S	3.5	49.8	109	36	72.3
F-9	7.1	55	5	S	3.5	52.8	104	36	68.2
F-10	7.1	55	10	S	3.5	52.1	99.8	37	71
F-11	7.1	55	10	S	3.5	50.1	108.9	36	71.1

with

$$\hat{\sigma}^2 = \frac{1}{1+(\alpha_f/3)^2}[\sigma_e^2 + \alpha_f \sigma_m^2]. \tag{4-10}$$

Here, $\hat{\sigma}$ is the equivalent stress, σ_e is the effective von Mises stress, σ_m is the mean stress, Y is the yield strength. The parameter α_f which defines the shape of the yield surface is a function of the plastic coefficient of contraction v_p and is given by

$$\alpha_f^2 = \frac{2(1-v_p)}{9(1+v_p)} \;. \tag{4-11}$$

The following hardening rule which includes the variation of the foam density is implemented in this model,

$$Y = \sigma_p + \gamma \frac{\hat{\varepsilon}}{\varepsilon_D} + \alpha_2 \ln\left(\frac{1}{1-(\hat{\varepsilon}/\varepsilon_D)^{\beta}}\right). \tag{4-12}$$

Where σ_p, α_2, γ, ε_D and β are material parameters, and $\hat{\varepsilon}$ is the equivalent strain. If the strain hardening rule is calibrated to a uniaxial compression test, the compaction strain ε_D can be expressed as

$$\varepsilon_D = \frac{9+\alpha_f^2}{3\alpha_f^2} \ln\left(\frac{\rho_f}{\rho_s}\right). \tag{4-13}$$

Where ρ_f is the foam density ρ_s and is the density of the base material.

In order to characterize mechanical property of the aluminum foam in compression, quasi-static compression tests based on ASTM D 1621 standard [11] were done on the foam specimens. The compression tests are simulated with use of LS-DYNA to insure the correct material behavior in further foam-filled column simulation. The stress-strain responses of the test and the simulation are presented in Figure 4.4. Good agreement shows that the specified material properties are quite accurate. Figure 4.5 shows the experimental and simulated deformation patterns and crush load-displacement curves of the tests (F-1), (F-8) and (F-10). The deformation mode is well described by the simulation. From this figure and Table 4.1, it can be recognized that the load angle has dramatic influence on first peak loads. In the case of axial impact the curve starts with high peak load that corresponds to elastic-plastic buckling of the tube and foam filler and continues with a repeated pattern. Each pair of the peaks is associated with the creating of one lobe in the tube. In the oblique impact tests, the tube does not experience elastic-plastic buckling. The first peak corresponds to creation of the first lobe and in continue the load oscillates around the mean crush load.

Due to isotropic behavior of the aluminum foam, more stability can be seen in the foam-filled tubes in the oblique tests in comparison with the empty tubes. The impact angle has not influenced the mean crush loads in the filled tubes. A comparison between experimental results of Figures 4.5 and 3.14 and Tables 3.4 and 4.1 shows that, in the same impact conditions, the mean crush load in foam-filled tubes is higher than mean crush load of empty one. That means foam-filled tubes are strengthened in the axial compressive direction. Also from Figure 4.5 it can be seen that the lateral strengthening mechanism leads to the formation of shorter folding length in foam-filled tubes in comparison with empty one. Because the foam resists against the inward penetration of tube walls, small lobes are created and more energy is absorbed.

The area under each load-displacement curve is the amount of absorbed energy. This energy absorption is associated by extensive stretching and bending collapse of the tube and foam cell walls.

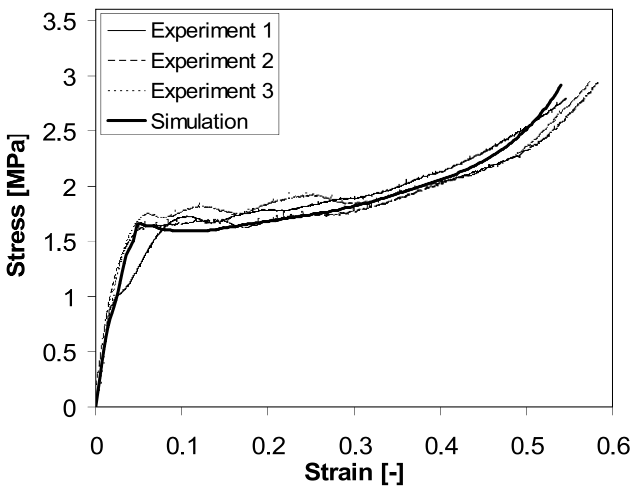

Figure 4.4: Comparison between simulation and experiment of the Alporas foam specimen with the relative density of 0.085

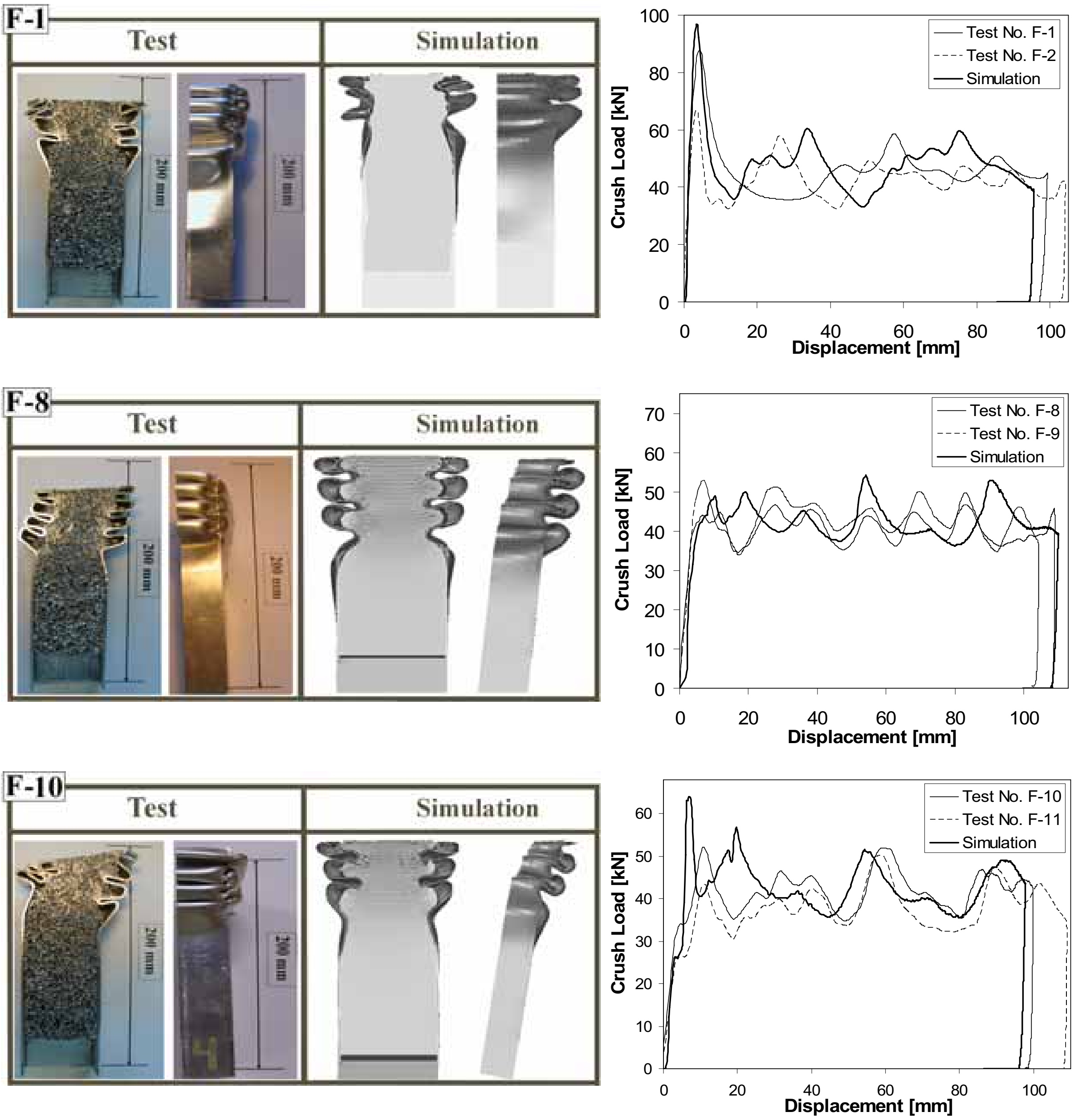

Figure 4.5: Comparison between the experimental and numerical dynamic crush patterns (left) and crush load displacement curve (right) of foam-filled tubes in the axial and oblique impact, impact angle: F-1: 0^o, F-8: 5^o and F-10: 10^o

Table 4.2 shows the average of the energy absorptions and specific energy absorption in empty and foam-filled tubes for equal impact velocity, 7.0 ± 0.1 m/s, and displacement, 100 mm. Consideration of this table indicates that filling of aluminum tube with foam has considerable effects on the crush behavior of the tubes. Here, the energy absorption and specific energy absorption are increased simultaneously in foam-filled tube. This means that more energy can be absorbed with lower weight.

Table 4.2: Comparison between the energy absorptions and specific energy absorption of empty and foam-filled tubes

Test No.	Filler type	θ [degree]	E [J]	Increase [%]	SEA [J/kg]	Increase [%]
Average of S-38 and S-39	-	0	2623	-	22908	-
Average of F-1 and F-2	Foam	0	4359	66.1	25343	10.6
Average of S-50 and S-51	-	5	2436	-	21275	-
Average of F-8 and F-9	Foam	5	4034	65.6	23453	10.2
Average of S-57 and S-58	-	10	2386	-	20838	-
Average of F-10 and F-11	Foam	10	3918	64.2	22779	9.3

4.3 Crush performance investigation of the honeycomb-filled aluminum tubes

Honeycomb is not a material, but a thin-walled cellular structure; see Figure 4.6, which can be made from different types of materials. The so called 'expansion' process is usually used to produce aluminum honeycomb. In this process adhesive is added on aluminum sheets along lines parallel to the "T_H" direction. The sheets are then assembled and cured in a block. Finally the slices (aluminum sheets) of the block are expanded to the desired cell cross section configuration. The corrugated process, in which pre-corrugated aluminum sheets are stacked and bonded with adhesive, is used for high density honeycombs. Honeycomb structures are used in various industrial products for their high strength/weight ratio, in which the honeycomb core is commonly sandwiched between flat plates. Further, the honeycomb structure can be used as a shock absorber in impacted objects, e.g., air-dropped container or crushed vehicle body. In these events, impact energy is transformed into the energy of plastic deformation and it is absorbed through the large compressive stroke. The honeycomb under compression loads exhibits the progressive buckling deformation. The energy absorption characteristic in impact crush deformation is strongly influenced not only by the mechanical properties of the honeycomb material and the thickness of cell wall but also by the geometric configuration of the honeycomb cell. Aluminum honeycomb has three principal directions due to its composure of corrugated and flat aluminum sheets, namely, directions "T_H" is the strongest, "L_H" is the intermediate strength and "W_H" is the weakest.

Aluminum honeycombs have large compressive deformation and therefore they have potential for increasing the energy absorption of the vehicle crash boxes. In this study a comprehensive experimental and numerical study is done to investigate the strengthening effect of honeycomb in the vehicle crash box. Existing expressions for predicting the mechanical behavior of the honeycomb are summarized and a series of axial and oblique impact tests are done on honeycomb-filled tubes.

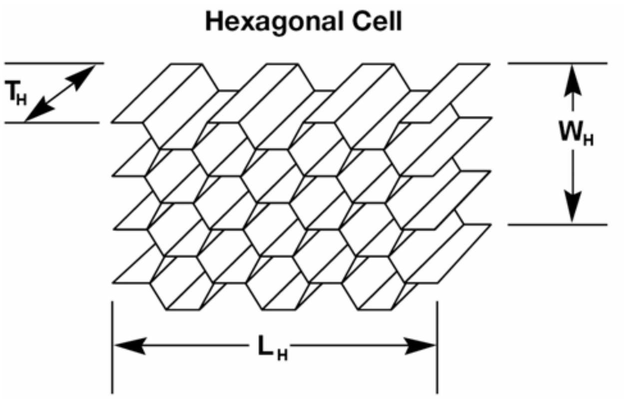

Figure 4.6: Honeycomb cellular structure

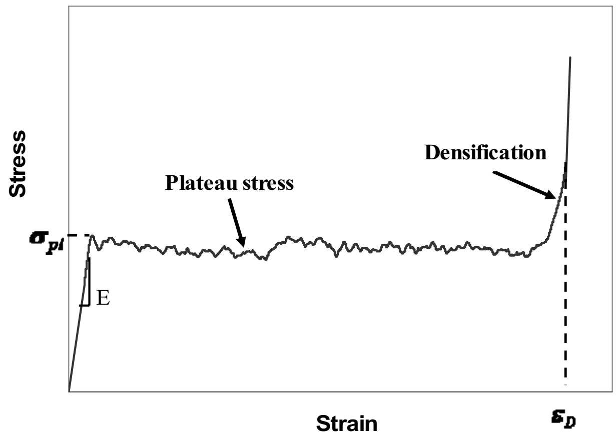

Figure 4.7: Typical compressive stress-strain curve of aluminum honeycomb

4.3.1 Analytical investigations

When honeycomb specimens are imposed by compression load in the strongest direction "T_H", after initial peak force, they crush in constant crush load and produce a plateau region. They exhibit a sharply rising peak load, followed by a series of oscillatory crush loads with a nearly constant mean value. The oscillations correspond to the onset of the progressive plastic buckling and subsequent plastic folding of the cellular structures, see Figure 4.7.

A fundamental theoretical study on the crush behavior of hexagonal honeycombs was published by Wierzbicki (1983) [114]. He used the concept of folding element and derived closed form solution for mean crushing load P_m and crush wave length *2H* of hexagonal honeycombs,

$$P_m = 8.61\sigma_{0h} t_h^{5/3} d_h^{1/3} = 7.17 t_h^{5/3} D_h^{1/3}, \qquad H = 0.821 t_{h1}^{1/3} D_h^{2/3}. \tag{4-14}$$

Where d_H and t_H are the width and thickness of the cell wall of honeycomb structure, σ_{0h} is the flow stress of honeycomb material and D_H is the minor diameter of the cell. From Figure 4.8, the 'tributary' area A_S of one basic folding element is $A_s = \sqrt{3}D_h^2 / 4$.

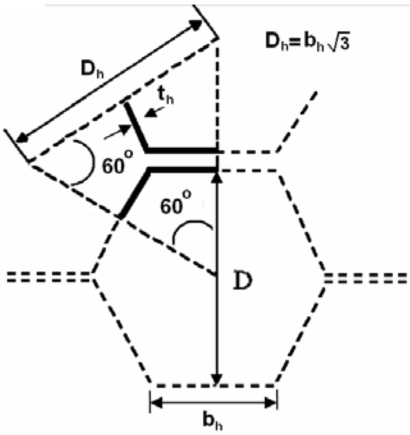

Figure 4.8: Honeycomb cell structure, cp. [91]

The crushing strength of honeycomb structure σ_h is defined as ratio of the mean crushing load to the tributary area, which is

$$\sigma_h = 16.55\sigma_{0h}(t_h / D_h)^{5/3}. \tag{4-15}$$

Relating cross sectional area of the basic 'Y' element $A_h = 2b_h t_h$ with the tributary area of one basic folding element A_S from the geometry given in Figure 4.8. One can show that $A_h / A_s = \rho_h / \rho_s = 8/3t_h / D_h$.

Hence, in term of relative density, the crushing strength of honeycomb can be written in the form

$$\sigma_h = 3.22\sigma_{0h}(\rho_h / \rho_s)^{5/3}. \tag{4-16}$$

Metallic honeycombs in compression along principal direction "T_H", first behave linear elastic that fallow by a plateau of roughly constant stress, leading into a final regime of steeply rising stress. Each regime is associated to a mechanism of deformation. On the first loading, the cell walls bend, giving linear elasticity. But when a critical stress is reached the cells begin to collapse and plastic hinges at the section of maximum moment in the bend members is formed. At high strains, the cells collapse sufficiently that opposing cell walls touch and further deformation compresses the cell wall material itself. This gives the final, steeply rising part of the stress-strain curve, labeled densification; see Figure 4.7, [33], [77].

The same behavior exists when honeycombs are compressed in L_H and W_H direction. An increase in the relative density of a honeycomb increases the relative thickness of the cell walls. Then the resistance to cell wall bending and cell collapse goes up, giving a higher modulus and plateau stress; and the cell walls touch sooner, reducing the strain at which densification begins.

Based on a bending model purposed by Gibson and Ashby [33], for a hexagonal honeycomb with cell wall thickness of t_h, its plastic crush strength σ_h in the "T_H" direction can be estimated as

$$\frac{\sigma_h}{\sigma_y} \approx 0.5\left(\frac{\rho_h}{\rho_s}\right)^2. \tag{4-17}$$

Where, σ_y is the yield stress of the cell wall material. The mean crushing load of a honeycomb-filled square column can be approximated as the sum of the resistance of an empty tube and honeycomb filler,

$$P_m = 13.06\sigma_0 t^{5/3} d^{1/3} + d_h^2 \sigma_h. \tag{4-18}$$

Figure 4.9 shows the comparison between experimental and analytical crushing resistance of honeycomb-filled tubes. The tube width is 60 mm and the thickness is 2 mm and honeycomb density is varied between 50-500 kg/m^3. It shows that the correlation between the theoretical prediction, Equation (4-16), and the experimental data is good if the flow stress of the honeycomb cell wall is assumed to be 100 MPa. Also it can be seen that the presented equation by Gibson and Ashby is a little overestimated.

4.3.2 Experimental and numerical results

Quasi-static and dynamic compression tests were conducted on honeycomb specimens and honeycomb-filled aluminum square tubes. The outer width of the aluminum tubes are 60 mm, while the nominal wall thickness is 2 mm. The outer width of the honeycomb core is 56 mm. Tubes with two lengths of 120 mm and 240 mm were used in quasi-static tests. Honeycomb cores were bonded to the tube walls by use of the epoxy adhesive. The tests were performed to analyze the strengthening effect of the strong mechanical properties of the honeycomb. Therefore, "T_H" direction of the honeycomb core is aligned with the crush direction. A standard tensile test machine, which is installed at the Institute of Material Science of the Leibniz University of Hannover, was used to apply the quasi-static load with a strain rate of 0.005 1/s.

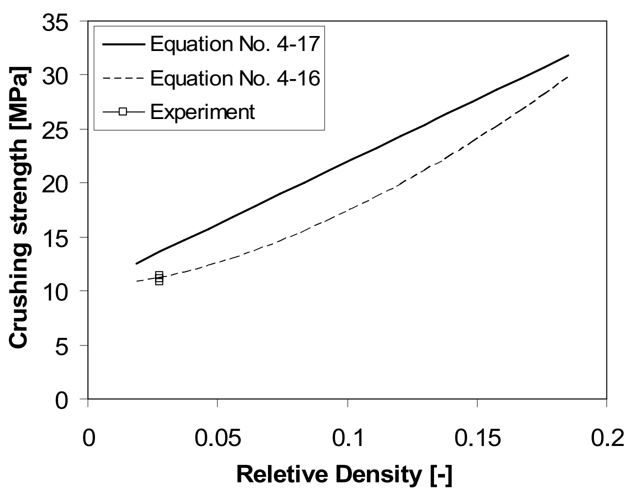

Figure 4.9: Comparison between experimental and analytical expressions of crushing strength of tube D 60 mm×2 mm AlMgSi0.5F22 with 5052 aluminum honeycomb filler

Dynamic tests were done in drop weight test rig, see Figure 3.5. Simply support boundary conditions are applied in quasi-static tests. For the dynamic test 270 mm long tubes were used and the lower end of tubes are fixed the same as foam-filled tubes. To investigate the crush performance of the tubes in non axial impact conditions, some dynamic tests were performed at impact angles θ of 5 and 10 degree.

Symmetric crush modes *CM* were seen visually in all tubes. Table 4.3 summarizes the results of the experimental tests. Here, quasi-static tests (F-12), (F-13) and (F-14) correspond to tubes with the length of 120 mm and the tubes length in tests (F-15) and (F-16) are 240 mm.

In order to characterize the crush response of the honeycomb material, quasi-static compression tests were done on honeycomb specimens separately. Square cubes of 100 mm×100 mm×120 mm honeycomb are used in the tests. Furthermore each compression test is simulated with LS-DYNA to insure the correct material behavior in further honeycomb-filled column simulation. The crush load-displacement responses of the tests and the simulation are presented in Figure 4.10. Good agreement shows that the specified material properties are quite accurate.

Numerical simulations of crash tests are performed to obtain more information about the crush mechanisms of the filled tubes which is difficult to measure during the test. The honeycomb s-

Table 4.3: Experimental results of impact test on honeycomb-filled tubes D 60 mm×2 mm AlMgSi0.5F22 with aluminum honeycomb 5052 filler

Test No.	V [m/s]	d [mm]	θ [degree]	CM [-]	N_s [-]	P_{max} [kN]	S_{max} [mm]	P_m [MPa]	η [%]
F-12	-	60	0	S	2	105.68	94.5	38	40.0
F-13	-	60	0	S	2	107.9	97.9	39	40.0
F-14	-	60	0	S	2	114.3	91.2	37	32.4
F-15	-	60	0	S	4	105.8	185.4	38	35.9
F-16	-	60	0	S	4	105.7	192.9	38	36.0
F-17	7.5	60	0	S	3	79.8	116.7	41	51.4
F-18	7.5	60	0	S	3	80.7	119.7	40	49.6
F-19	8.6	60	0	S	4	78.1	157.9	40	51.2
F-20	8.6	60	0	S	4	83.1	158.0	39	46.9
F-21	8.7	60	0	S	4	77.2	157.7	39	50.5
F-22	9.8	60	0	S	5	75.2	160	39	51.9
F-23	9.9	60	0	S	5	82.6	160	40	48.4
F-24	7.5	60	5	S	3.5	50.4	127.6	30	59.5
F-25	7.5	60	5	S	3.5	46.3	118.0	32	69.1
F-26	7.5	60	5	S	3.5	48.1	112.0	32	66.5
F-27	7.5	60	10	S	3.5	46.9	132.6	31	66.1
F-28	7.5	60	10	S	3.5	50.5	127.3	32	63.4
F-29	7.5	60	10	S	3.5	49.5	132.7	31	62.6

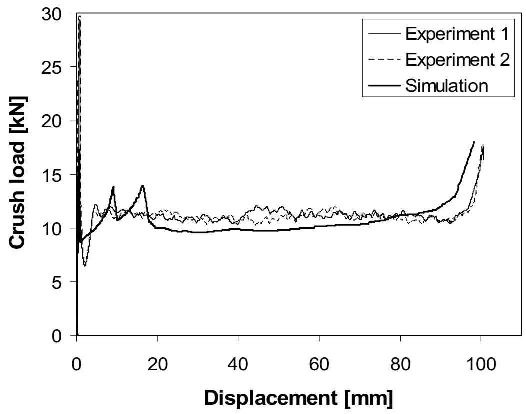

Figure 4.10: Quasi-static crash test of honeycomb square specimens 100 mm×100 mm×120 5052 aluminum, $d_h = 6.3$ mm, $t_h = 0.25$ mm

-pecimens and the honeycomb-filled square tube with the dimension of experiment specimens are considered. Because of the symmetry in axial tests, only one half of the specimens are modeled. The tube walls are modeled with the Belytschko-Tsay thin shell elements. The honeycomb filler is modeled with solid elements and symmetrical boundary conditions are applied on all free vertical edges. Rigid body elements are used to model the crosshead of the compression machine and impactor. Initial imperfections are prescribed along the length of tube in the simulations, the same as empty tubes. Also to ensure quasi-static loading when using explicit code, the rigid body has been given a prescribed velocity like Equation (3-21). When explicit dynamic procedure is used to simulate quasi-static crush process, very small time increments are used. To overcome to this problem the mass is scaled up. The contact between the rigid body and the specimen is modeled using a node to surface algorithm with a friction coefficient of $\mu = 0.2$. To account for the self contact between the tube walls during deformation, a single surface contact algorithm is used. The adhesive effect is simulated by a tiebreak contact between the tube wall and the honeycomb filler. Failure due to excessive tension and sharing force is considered for the adhesive material. Onset of failure is governed by the following failure criterion

$$\left(\frac{\sigma}{\sigma_{fail}}\right)^2 + \left(\frac{\tau}{\tau_{fail}}\right)^2 \leq 1. \tag{4-19}$$

Where σ_{fail} and τ_{fail} are tensile and shear strength of the adhesive material, respectively. In this simulation the nominal values of σ_{fail}=30 MPa and τ_{fail}=5 MPa are selected. The aluminum alloy is modeled as an elastoplastic material using isotropic and kinematic work hardening with the use of material number #103 in LS-DYNA. In order to simulate the honeycomb material number #29 in LS-DYNA is used. In this model the behavior of the honeycomb before compaction is orthotropic where the components of stress tensor are uncoupled. The elastic modulus vary from their initial values to the fully compacted values linearly with the relative volume,

$$E_{ii} = E_{iiu} + \beta_H (E - E_{iiu}), \qquad ii = aa, bb \text{ and } cc, \tag{4-20}$$

$$G_{ij} = G_{iju} + \beta_H (G - G_{iju}), \qquad ij = ab, bc \text{ and } ca. \tag{4-21}$$

Where *aa* is the strongest "T_H" direction, *bb* and *cc* are the honeycomb ribbon "L_H" and transverse "W_H" direction respectively, and

$$\beta_H = \max\left\{\min\left(\frac{1-V_H}{1-V_{HD}}\right)\right\}. \tag{4-22}$$

In this equation V_H is the relative volume, that is defined as the ratio of the current volume over the initial volume and V_{HD} designates the relative volume at full densification. In the computation of stresses, as volumetric compaction occurs, the directional elastic moduli vary linearly from their initial values to the fully compacted value according to equation (4-20) and (4-21). For fully compacted material, the assumption is that material behavior becomes elastic-perfectly plastic. It was assumed that there is no failure in honeycomb core. The material is assumed to compress under load until full compaction and continue as a perfectly plastic material, which is typically observed in this kind of materials [21]. The material parameters, including load curves, were extracted from quasi-static compression tests and the manufacture data [73].

Figure 4.11 shows the experimental and simulated deformation pattern of test (F-15) and crush load displacement curves of tests (F-15) and (F-16). Also the same results for tests (F-17), (F-24) and (F-27) are presented in Figure 4.12. Good correlation can be seen between the simulations and experiments. The simulated mean crush loads are little higher than the experimental results. Therefore, the final crush displacement is smaller than the experimental ones. As a result of inertia effect, it can be recognize from in Table 4.3 that the mean crush loads of dynamic tests are higher than quasi-static ones.

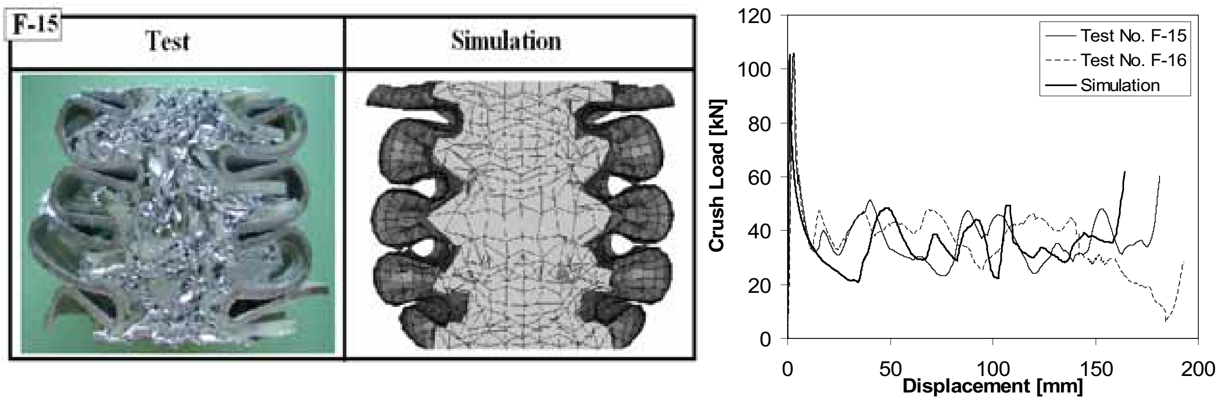

Figure 4.11: Comparison between the quasi-static experimental and numerical quasi-static crush patterns (left) and crush load displacement curves (right) of honeycomb-filled tubes

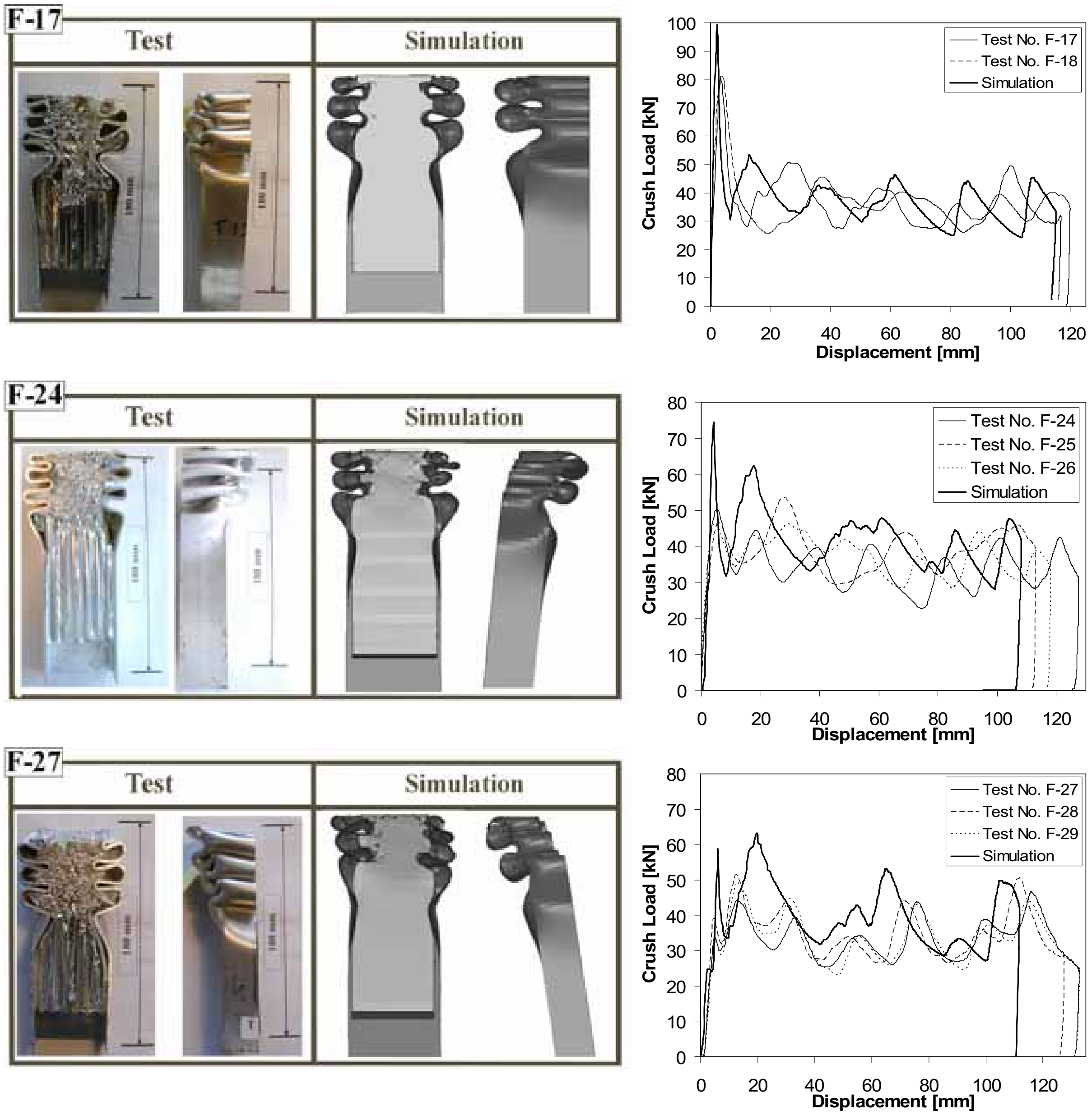

Figure 4.12: Comparison between the experimental and numerical dynamic crash patterns (left) and crash load displacement curve (right) of foam-filled tubes in the axial and oblique impact, impact angle F-17: 0^o, F-24: 5^o and F-27: 10^o

The effect of load angle on first peak load can be seen in the Figure 4.12. In the case of axial impact the curve starts with a high peak load that corresponds to elastic-plastic buckling of tube and honeycomb cell walls and continues with a repeated pattern. Each pair of peaks is associated with the creating of one lobe. In the case of oblique tests the first peak corresponds to creation of first lobe. In continue the load values oscillate around the mean crush load. The impact angle has influence on mean crush load as well. Because of low strength of honeycomb in the lateral directions, unlike foam-filled tubes, when the impact angle increases the mean crush load decreases. From Tables 4.3 and 3.4 it can be seen that in the same impact conditions, the honeycomb-filled tubes have higher mean crush loads than empty one. That means honeycomb-filled tubes have been strengthened in the axial ("T_H" direction) direction.

Also from Figure 4.12 and Figure 3.14 and 15 the shorter folding length in the honeycomb-filled tubes than empty tubes ,as a result of lateral ("L_H" and "W_H" directions) strengthening mechanism by the honeycomb, can be recognized. Because the honeycomb resists against the inward penetration of tube walls, small lobes are created and more energy is absorbed. Therefore, it can be concluded that in addition to axial property of honeycomb, the lateral strength has great influence on the strengthening mechanism of the tubes.

The area under each load displacement curve is the amount of absorbed energy. This energy absorption is associated by extensive stretching and bending collapse of the tube and honeycomb cell walls. Table 4.4 shows the average of the energy absorptions and specific energy absorptions of empty and honeycomb-filled tubes of equal crash velocity, 7.5±0.2 m/s, and displacement, 100 mm. This table indicates that filling of aluminum tube with aluminum honeycomb have considerable effects on crush behavior of tubes. An increase of energy absorptions and specific energy absorptions takes place simultaneously in honeycomb-filled tube. This means that more energy can be absorbed by lighter structure.

The low strength of honeycomb in the "L_H" and "W_H" directions provided weak stability in the filled tubes and caused reduction in the crush efficiency of the filled column in the oblique conditions. From Table 4.4 it can be seen that in the case of 10 degree impact angle, the increases in the energy absorption and specific energy absorption of the filled tube are considerably lower than the increases of these two values in the axial impact. As mentioned before both axial and lateral strengths of honeycomb determine the value of strengthening effect. The honeycomb strengths in different axes depend on the honeycomb density. Previously it has been proven that using honeycomb with higher density in filled structures will result more energy absorption [123]. Also it has been emphasized that an increasing of the honeycomb density always increase the energy absorption but there is one critical honeycomb density beyond that the structure will lose its weight efficiency. This critical density varies for different tube geometries. Also it has been shown that in order to find an optimum honeycomb-filled crash box, special consideration should be performed to select proper tube and honeycomb combination [126]. They used the crashworthiness optimization procedure to find optimum tube geometry and honeycomb density under some practical optimization constraints.

A higher crush efficiency of honeycomb over the foam is expected from the comparison of Equations (4-6) and (4-16). The fractional power to which the relative density is raised is in both cases almost the same (1.66 vs 1.5). However, the numerical coefficient in the solution for the Honeycomb material is an order of magnitude larger than that describing the foam material.

Table 4.4: Comparison between the energy absorptions and specific energy absorptions of empty and honeycomb-filled tubes.

Test No	Filler type	θ [degree]	E [J]	Increase [%]	SEA [J/kg]	Increas e
Average of S-29 and S-30	-	0	3232	-	25792	-
Average of F-17 and F-18	Honeycomb	0	3769	16.6	27509	6.7
Average of S-42 and S-43	-	5	2872	-	22921	-
Average of F-24 to F-26	Honeycomb	5	3345	16.5	24416	6.5
Average of S-55 and S-56	-	10	2887	-	23041	-
Average of F-27 to F-29	Honeycomb	10	3251	12.6	23730	3.0

To compare the strengthening effects of the honeycomb and the foam materials, the crash simulation of identical tubes filled with honeycomb and foam are conducted previously [124]. A density of 230 kg/m^3 was selected for honeycomb and foam. Unlike the expectation from the theoretical formulations the honeycomb has lower resistance against inward penetration than the foam. Therefore, in this case the energy absorption of the foam-filled tube is 6.2 % higher than the honeycomb-filled. As a result it can be concluded that for absorbing more energy with lower weight, the aluminum foam is preferred to aluminum honeycomb. Therefore in this study the effort is done to find optimum foam-filled tube.

4.4 Crush performance optimization of the foam-filled aluminum tubes

As mentioned before, the existence of foam inside of the tubes creates a resistance force against the inward penetration of tube walls, during the crush process. This resistance force is directly related to the foam density. Previously it has been shown that selection of the correct combination of the honeycomb and tube is a determinant issue to gain an efficient (higher energy absorption capacity) and light energy absorber [123], [126]. Similarly here, the crush behavior of the foam-filled tubes with identical tube dimensions and different foam densities are determined and summarized in Table 4.5. From this table it can be obviously recognized that the foam filling solution does not always end to simultaneously efficient and light energy absorbers. It can be seen that while the foam density increases the energy absorption increases considerably. But if one considers the *SEA*, there is one optimal foam density where the maximum *SEA* occurs. When foam with lower or higher density than this optimum density is selected, the specific energy absorption decreases. Again it can be concluded that to attain an efficient foam-filled crash absorber, a selection of the tube geometry and foam density is determinant.

Hanssen et al. (2001) [41] used an optimization procedure to minimize the weight of foam-filled tubes with a target energy absorption E_{goal}. They used the formula (4-8) to predict the mean crush load. With the help of this formula they estimate the energy absorption of the foam-filled tubes. They found that the optimum foam-filled tube compared to the non-filled tube show smaller cross section dimension in addition to less weight. Although they used very simple and time saving method to estimate the energy absorption of the filled tube, but this method have some disadvantages that can not be used for real world problems. As it can be seen in the formula (4-8) there are two unknown flow stresses σ_0 and σ_{0f} correspond to the aluminum tube and foam material, respectively, and also the interaction coefficient C_{ave} is also undetermined. Before using this formula in the optimization procedure, these three unknowns have to be determined.

A survey in the published work shows that there is no general method to determine the flow stress. This parameter is defined based on flow rule of the material. Abramowicz and Wierzbicki (1989) [4] assumed that the flow stress σ_0 is defined as an average stress over a given strain range (0, $\varepsilon_{\max}$),

$$\sigma_0 = \int_0^{\varepsilon_{\max}} \sigma(\varepsilon) d\varepsilon. \tag{4-23}$$

Here, $\varepsilon_{\max}$ is the maximum strain at failure. They showed that the flow stress for progressively collapsing columns made from mild steel equals approximately to $\sigma_0 = 0.92\sigma_u$. Abramowicz and Jones (1984) [2] replaced σ_0 by σ_u for a strain rate insensitive material and for quasi-static crush load. They also used a strain rate formula for σ_u for the dynamic crush load. Chen and Wierzbicki (2002) [17] used the value $\sigma_0 = \sqrt{\sigma_y \sigma_u /(n+1)}$ for the mean crush load. Here the n is the hardening parameter. Some researches also used the 90-95 % of the ultimate stress σ_u for equivalent flow stress. Average of the yield stress σ_y and ultimate stress σ_u has been used by some other researchers. After the selection of one of the above definition, several experimental tests are needed to calibrate the flow stress.

Table 4.5: Strengthening effect of tube filled with foam with different densities, tube D 55 mm×2 mm AlMgSi0.5F22 and Alporas foam

Test No.	ρ_f [kg/m^3]	E [J]	Increase [%]	SEA [J/kg]	Increase [%]
1	-	3736	-	25158	-
2	60	4383	17.31	27076	7.62
3	160	5242	40.31	27143	7.89
4	200	5634	50.8	27399	8.91
5	230	6134	64.17	28530	13.4
6	260	6178	65.36	27534	9.44
7	360	6631	77.49	25940	3.11
8	460	7139	91.1	24885	-1.1

In the case of foam and honeycomb the determination of the flow stress is more difficult. Normally the researchers use the crash test results to calibrate the flow stress. The strain rate sensitivity of the flow stress, also forces the researchers to calibrate this parameter in different strain rates. In the dynamic case, the inertia effect also influences the flow stress.

To determine the interaction coefficient C_{ave}, it is needed to generate crash tests on foam-filled tubes for different tube geometry and foam densities.

By the above understanding, it is clear that the predicted energy absorption by the Equation (4-8) is not an exact value and can not be used for more real problem where the exact value of energy absorption in needed.

Therefore, the previous optimization procedure that was used to optimize empty aluminum tube, is implemented to optimize the crush performance of the foam-filled tube. Since the foam gives additional support to the tube walls, at the same tube dimensions, the bending strength of foam-filled would be higher than empty tube. As a result in the optimization procedure, the minimum allowable tube width is selected d= 55 mm and the foam density is introduced as new optimization parameter. The optimization procedure is applied to find the optimum foam-filled tube that absorbed the energy of equal to optimum empty tube (7602 ± 20 J) and has maximum stroke efficiency. The foam density is introduced as optimization parameter and foam densities between 50-540 $\mathrm{kg/m^3}$ have been selected. It should be mentioned that a new estimation method in used to find the foam properties for different densities. The density dependent equations to determine elastic modulus, crushing strength and densification strain presented by Gibson and Ashby (2000) [33] is used to find the mechanical properties of the foam materials under compression load. The experimental impact test results on the foam material and also existing experimental results from other literatures are used to calibrate these equations. Then the needed information for the finite element simulation is extracted from these data.

Table 4.6 shows the results of optimum foam-filled tube. It can be seen that the foam-filled tube absorbed the same energy as the optimum empty tube but it has more than 19 percent lower weight [127]. Here, lower stroke efficiency of the optimum foam-filled tube compare to optimum empty tube can be considered as a disadvantage of using foam inside aluminum tube.

Table 4.6: Optimum foam-filled square tube AlMgSi0.5F22 and Alporas foam

Tube Type	t [mm]	d [mm]	l [mm]	ρ_f [$\mathrm{kg/m^3}$]	E [J]	η [%]	S_E [%]	SEA [J/kg]	increase [%]
Foam-filled	2.13	55	210	224	7623	60	66	31200	19.4

5. Bending crush investigation and optimization of empty and filled aluminum beams

5.1 Introduction to the crashworthiness of beams under bending load

Although the bending mode of collapse is the predominant mechanism of structural collapse of beam type structural elements of today's vehicles, it has drawn considerably less attention than the axial collapse. This predominance of the bending mode is the result not only of the current design practice but also of the natural tendency of structures to collapse in a mode that requires the least expenditure of energy; which is bending in the case of thin-walled beam elements like vehicle bumper and pillars. When the thin walled members are subjected by bending load, collapse of the component will be triggered at the location where compressive stress reaches critical value, causing the side or flange of the section to buckle locally, which initiates formation of a plastic hinge-type mechanism. Since the bending moment at the newly-created plastic hinge cannot increase any more, the moment distribution changes and a further increase of the external load creates additional hinges, until eventually, the number and the distribution of hinges is such that they turn the structure into a kinematically movable hinge collapse mechanism. Thus, the overall collapse mechanism is controlled by hinge absorbing capacity of the plastic hinges. In this study comprehensive experimental and numerical investigations are done to determine the bending behavior of empty and foam-filled aluminum tubes. The existing analytical formulations are summarized and compared with experimental results.

5.2 Analytical investigations

Bumper beams are an important part of vehicles because they protect the driver and passengers during collisions. Relatively high value of collision energy is absorbed by the bending deformation of the bumper beams. Bumper systems are commonly made by aluminum extrusion. Several studies deal with the determination of the bending behavior of aluminum extrusions. The first comprehensive experimental and theoretical investigation of the bending performance of square and rectangular prismatic beams was made by Kecman (1983) [53]. He proposed a simple failure mechanism involving stationary and moving plastic hinge lines. He assumed that bending collapse is initiated by local buckling of the compressively loaded flange and, using the concept of "effective flange width", develops expressions for the maximum bending strength capacity of a rectangular box section. If the critical local buckling stress σ_{cr} is less than material yield stress σ_y, the compressively loaded flange will buckle elastically, producing a non-linear stress distribution with the middle part carrying considerably less load than the corners. Thus, in terms of the corner stress, the effective width of the flange is reduced

$$d_e = d(0.7\sigma_{cr} / \sigma_y + 0.3). \qquad (5\text{-}1)$$

Where critical local buckling stress is given by

$$\sigma_{cr} = [K_1 \pi^2 E_t (t/d)^2] / 12(1-\upsilon^2). \qquad (5\text{-}2)$$

With, $K_1 \approx 5.23 + 0.16(d/b)$ being the flange buckling coefficient and d and b the sides of the section. Different formulations are used for the maximum moment depending on the magnitude of the critical local buckling stress σ_{cr} relative to the material yield strength σ_y.

If $\sigma_{cr} \le \sigma_y$ then,

$$M_{\max} = \sigma_y t b^2 [(2d + b + d_e(3d/b + 2))] / 3(d+b). \qquad (5\text{-}3)$$

If $\sigma_{cr} \ge 3\sigma_y$ (fully plastic moment M_p),

$$M_{\max} = M_p = \sigma_y t [d(b-t) + (b-t2)^2 / 2]. \qquad (5\text{-}4)$$

And finally, if $\sigma_y < \sigma_{cr} < 3\sigma_p$,

$$M_p^* = \sigma_y t b(d + b/3). \qquad (5\text{-}5)$$

And therefore the maximum strength becomes from linear interpolation,

$$M_{\max} = [M_p^* + (M_p - M_p^*)(\sigma_{cr} - \sigma_y)] / \sigma_y. \qquad (5\text{-}6)$$

In addition to deriving expressions for the maximum bending strength, Kecman developed a comprehensive model of the plastic hinge mechanism and its bending collapse behavior, achieving very good agreement with experimental results.

Wierzbicki et al. (1994) [113] extended the concept of a superfolding element, developed originally for axially loaded columns, to the case of bending and combined bending and compression loading. Usually, the bending collapse of thin-walled beams is localized at the central part of the beam, and the plastic work is dissipated through the formation of hinge lines and membrane action zones and the remaining parts of the beams undergo a rigid body rotation, see Figure 5.1. In this figure the typical crash pattern of the thin-walled beam with its hinge lines is shown. After a small rotation angle the local collapse occurs in the beam and its resistance drops significantly resulting in low energy absorption efficiency. The localized nature of bending collapse deformation is characterized by the folding length H, which is obtained from the postulate of minimum mean load,

$$H = 1.276 b^{2/3} t^{1/3}. \qquad (5\text{-}7)$$

The moment-rotation characteristic in the post buckling range was derived analytically based on the concept of superbeam element,

$$M(\theta) = P_m b(0.576 + 1/2\theta). \tag{5-8}$$

Where

$$P_m = 2.76\sigma_0 b^{1/3} t^{5/3}. \tag{5-9}$$

And σ_0 is the equivalent flow stress [17],

$$\sigma_0 = \sqrt{\sigma_y \sigma_u /(n+1)}, \tag{5-10}$$

With $\sigma_{y,}$ σ_u and n are yield stress, ultimate stress and exponent of the stress-strain power low of the material, respectively.

An approximate expression for the ultimate bending moment of the beam was derived by Sontasa (1999) [92],

$$M_{\max} = 4.65\sigma_0 b^{5/3} t^{4/3}. \tag{5-11}$$

By equating Equation (5-8) and Equation (5-11), the critical bending rotation θ_c for local sectional collapse can be obtained,

$$\theta_c = 1/4[1/(0.8(b/t)^{1/3} - 0.576)]^2. \tag{5-12}$$

Therefore, the moment-rotation response of a thin-walled square section can be expressed as

$$M(\theta) = \begin{cases} 4.65\sigma_0 b^{5/3} t^{4/3} & 0 \le \theta \le \theta_c, \\ P_m b(0.567 + 1/2\theta) & \theta \ge \theta_c. \end{cases} \tag{5-13}$$

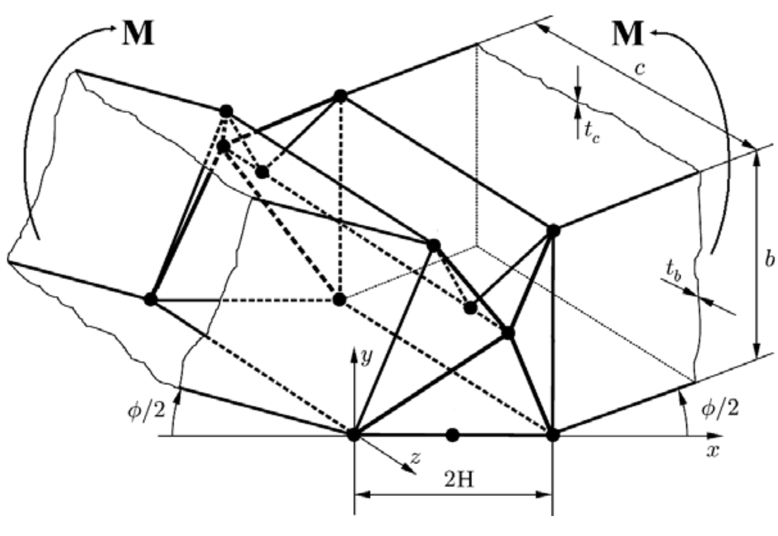

Figure 5.1: A simple model of bending collapse of a thin-walled beam [53]

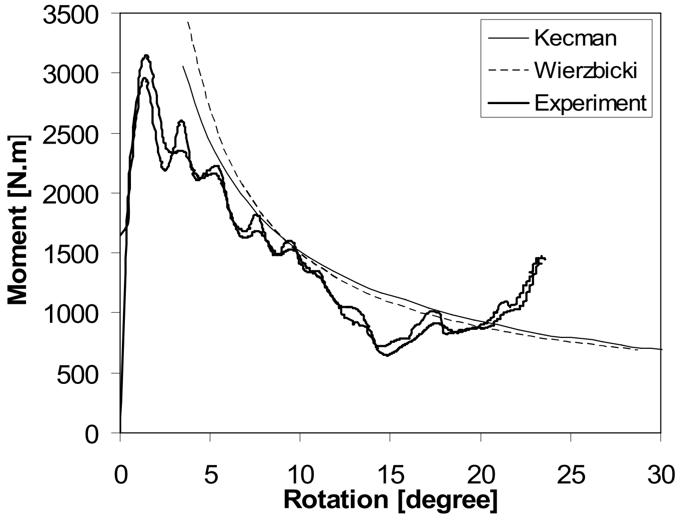

Figure 5.2: Comparison between experimental and theoretical expressions

Figure 5.2 shows a comparison between the Kecman's and Wierzbicki's formulations and experimental bending test results. Here, as result of elastic-plastic buckling resistance of the beam, first the experimental moment rises sharply up to the maximum moment and at this stage the tube buckles locally and hinge lines are created. The beam bends at the position of the hinge lines and additionally some damage are created in the highly strained parts of the beam. As result of creation of these mechanisms the moment value is decreased. There is a sudden fall in the moment value at the bending angle about 10 degree. The creation of the damages and rupture in some parts of the beam causes this descent. After about 15 degree rotation angle the tube walls touch each other and the moment rises again. Here it can be seen that except for initial stage of the moment curve, the two methods predict the bending behavior of the beam acceptable. Since these two models considered no rupture and damage in the beam, their perditions after about 10 degree rotation angle is overestimated. These two models predict the bending behavior of the beam only in small rotation angle and are not valid for tube bending after touching of the beam walls.

Cellular structures and, specially, metal foams have the capability to absorb a large amount of energy when they are severely deformed. Hence, to improve the energy absorption efficiency of thin walled sections, the concept of introducing lightweight metal fillers into thin-walled beams has attracted increasing interest. Low weight foams inside bumper beams reduce the rebound after compression and also allow using thinner bumper profiles and more potential for design freedoms. A pilot study on bending collapse of thin walled beams with light weight metal filler was given by Santosa and Wierzbicki (1999) [93]. They showed that the low density metal core retards sectional collapse of the thin-wall beam, and increases bending resistance for the same rotation angle. Their numerical simulations showed that, in terms of achieving the highest energy absorption to weight ratio, columns with aluminum honeycomb or foam core are preferable to thickening the column wall. Moreover, the presence of adhesive improved the specific energy absorption significantly. Bending collapse of double hat box beams filled with aluminum foam was numerically investigated by Shahbek et al. (2004) [99]. The same results as simple column were reported by them. Chen et al. (2002) [17] assumed that the ultimate bending moment of filled section is of the addition form of the ultimate bending moment of a non filled section and an elevation resulting from filling,

$$M_f = M_{max} + \Delta M \,. \tag{5-14}$$

Where M_f denotes the ultimate bending moment of the foam-filled section, M_{max} is the ultimate bending moment of an empty section given in equations (5-3) to (5-6) and ΔM is the moment elevation resolution from foam filling, which is a function of the foam properties and section dimensions. Based on this assumption the bending moment of a foam-filled section in the post buckling range can also be evaluated by a horizontal and a vertical shifting of the moment-rotation characteristic of the corresponding empty section given in equation (5-13). The bending moment of the foam-filled section is then equal to

$$M(\theta) = \begin{cases} M_f & 0 \le \theta \le \theta_{cf}\,, \\ P_m b(1/\sqrt{\theta} - 1/\sqrt{\theta_{cf}}) + M_f & \theta > \theta_{cf}\,. \end{cases} \tag{5-15}$$

Where $M_f(\theta)$ is the bending moment of the foam-filled section at rotation angle θ and P_m and M_f are given in Equations (5-9) and (5-14), respectively.

Here θ_{cf} is the critical bending rotation for the local sectional collapse of a foam-filled section and was given by Santasa (1999) [93] based on numerical simulation results,

$$\theta_{cf} = \theta_c + 3.98\frac{\rho_f}{\rho_s}. \tag{5-16}$$

To obtain the full expression of the bending moment characteristic of a foam-filled section, the moment elevation ΔM needs to be determined. Generally numerical or experimental results are used to find this value for every foam density and section dimension.

5.3 Experimental and numerical results

Bending impact tests were conducted on empty and foam-filled aluminum beams. The aluminum beams are made from aluminum 6060 (AlMgSi0.5F22) alloy and Alporas aluminum foam with relative density of 0.085 is used. The outer diameters of the aluminum beams d are 55 and 60 mm, while the nominal wall thicknesses t are 2, 3 and 4 mm. Beams with the length of l=550 mm are used. The beams are supported by two steel cylinders with 50 mm diameter placed 400 mm apart. Two cylinders with the radius of r=25 mm and r=50 mm are used as impactor in the mid-span, see Figure 5.3. The length of the aluminum foam in filled beam is 330 mm. An impact mass of 128 kg was selected for all tests. The experimental tests were conducted on the drop test rig, see Figure 3.5.

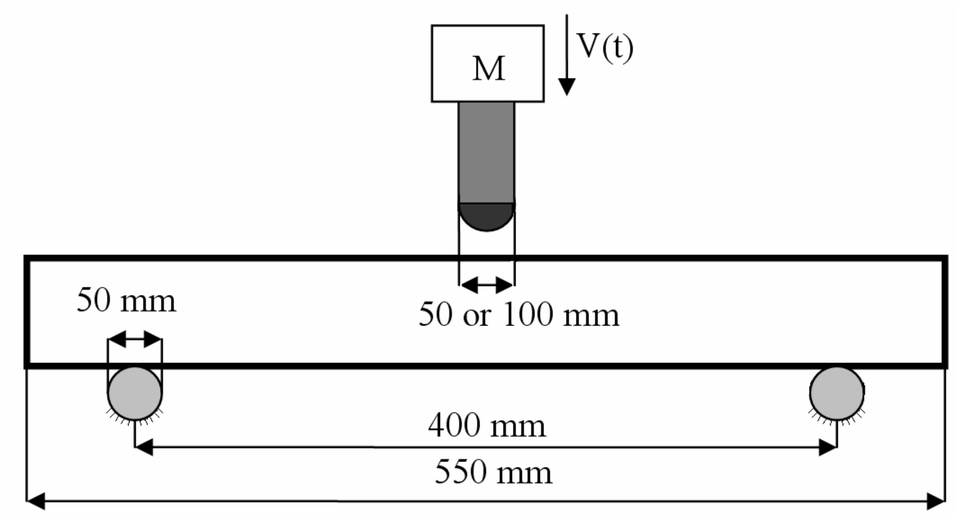

Figure 5.3: Boundary and loading conditions

Numerical simulations of crash tests are performed to obtain local information about the crush process. The modeling and analysis were done with the use of the explicit finite element code LS-DYNA. The empty and foam-filled beams with the corresponding dimensions of the specimens used in the experiments are considered. Because of the symmetry, only one half of the specimens are modeled.

The beam walls are modeled with the Belytschko-Tsay thin shell elements. The foam filler is modeled with solid elements. Symmetrical boundary conditions are applied on all free edges. Rigid body elements are used to model the impactor.

The contact between the rigid body and the specimen is modeled using a node to surface algorithm with a friction coefficient of $\mu = 0.2$. To take into account the self contact between the tube walls during deformation, a single surface contact algorithm is used. The node to surface contact algorithm is used for contact between the beam wall and the filler. The aluminum alloy is described as an elastoplastic material using isotropic and kinematic work hardening with the use of material number #104 in LS-DYNA. An anisotropic damage model is used in this material model. The damage law acts on the plane stress tensor in the direction of the principal total shell strains, ε_1 and ε_2, as follows

$$\begin{aligned} \sigma_{11} &= (1 - D_1(\varepsilon_1))\sigma_{110}, \\ \sigma_{22} &= (1 - D_2(\varepsilon_2))\sigma_{220}, \\ \sigma_{12} &= (1 - (D_1 + D_2)/2\sigma_{120}. \end{aligned} \tag{5-17}$$

The damage in the transverse plate shear stresses in the principal directions are assumed as follows

$$\begin{aligned} \varepsilon_{13} &= (1 - D_1/2)\sigma_{130}, \\ \varepsilon_{23} & (1 - D_2/2)\sigma_{230}. \end{aligned} \tag{5-18}$$

Here, $D_1(\varepsilon_1)$ and $D_2(\varepsilon_2)$ are anisotropic damage functions for the loading direction 1 and 2, respectively. Stresses σ_{110}, σ_{220} , σ_{120} ,σ_{130} and σ_{230} are stresses in the principal shell strain directions as calculated from the undamaged elastic-plastic material behavior. The aluminum foam is modeled with the foam model of Dehspande and Fleck [19] material number #154 in LS-DYNA. In this model the foam is considered as an isotropic material.

Details of the test results of empty and foam-filled aluminum beams are summarized in Table 5.1. Here, P_{max} is the first peak load and P_{60} is the crush load at the 60 mm crush length. The experimental results show that the aluminum foam inserts have a noticeable effect on increasing the bending resistance of the beams. The maximum bending load in the empty beam (Test S-59) is 26.2 kN while this value in the filled-beam (Test F-30) is 33.2 kN, which is an increase of around 25%. The same behavior can be recognized in the other tests comparing empty and filled beams.

Experimental results showed some damages in the tube walls and aluminum foam. Therefore, in this model, fracture is introduced by eroding elements when a certain criterion is satisfied. A strain based fracture criterion is adapted by default to the material model #104. In the current work the MAT_ADD_EROSION option in the LS_DYNA is used to examine the stress based fracture criterion. Since the results of the bending simulations with the strain based fracture criterion showed a better agreement with the experiments, all simulations are performed the strain based fracture criterion. Here, an element ruptures when one of the principal strains reaches a tensional fracture strain $\varepsilon^p_{failure}$. The damage is defined with a damage variable ω which is based on plastic strain. When the plastic strain at through thickness integration point exceeds the failure strain $\varepsilon^p_{failure}$ the damage variable is activated as follows,

$$\omega = \frac{\varepsilon^p_{eff} - \varepsilon^p_{failure}}{\varepsilon^p_{rupture} - \varepsilon^p_{failure}} \qquad if \qquad \varepsilon^p_{failure} \le \varepsilon^p_{eff} \le \varepsilon^p_{rupture}. \tag{5-19}$$

The damage variable ω is zero when the plastic strain reaches failure strain $\varepsilon^p_{failure}$ and rises to unity when the plastic strain reaches the rupture strain $\varepsilon^p_{rupturee}$. The nonlinear damage variable controls the softening behavior of the material after failure strain is exceeded. In this model the effective stress versus plastic strain data controls the plastic deformation and rupture of aluminum beam. The results of standard tensile tests are used to find the failure and rupture strains and the results of bending tests on empty beams are used to calibrate the damage variable.

For the damage in the foam filler, the volumetric strain controls the strain based criterion. i.e.

$$\varepsilon \ge \varepsilon_{cr} \qquad \Rightarrow \quad \sigma = 0. \tag{5-20}$$

Table 5.1: Experimental bending test results on aluminum beam AlMgSi0.5F22

Test No.	r [mm]	V [m/s]	d [mm]	T [mm]	ρ_f [Kg/m^3]	P_{max} [kN]	P_{60} [kN]
S-59	25	4.4	55	2	-	26.2	8.76
S-60	25	4.4	55	2	-	25.6	8.28
S-61	50	4.1	55	2	-	25.2	7.32
S-62	50	4.1	55	2	-	24.8	6.36
S-63	50	5.4	55	2	-	26.8	9.9
S-64	50	5.4	55	2	-	27.4	10.12
S-65	25	4.1	60	3	-	35.2	19.62
S-66	25	4.1	60	4	-	53.4	20.4
F-30	25	4.4	55	2	230	33.2	14.1
F-31	25	4.4	55	2	230	33.6	12.38
F-32	50	4.1	55	2	230	29.2	10.58
F-33	50	4.1	55	2	230	28.8	9.16
F-34	50	5.4	55	2	230	34.28	14.54
F-35	50	5.4	55	2	230	33.04	13.96

The stress based criterion is realized by erosion of elements when the maximum principal stress reaches a critical value

$$\sigma_1 \geq \sigma_{cr} \quad \Rightarrow \quad \sigma = 0. \tag{5-21}$$

The tensile test data can be used to estimate the tensile failure strain ε_{cr}. Henssen et al. (2002) [42] showed that the tensile failure stress of aluminum foam is approximately equal to initial plateau stress in compression. This is in agreement with present compression tests on foam material and the compression and tensile test results provided by foam producer. Therefore, the plateau stress has been used as a critical principal stress. Also the results of axial compression and current bending tests on foam-filled tubes have been used to calibrate the material parameters.

Figure 5.4 and Figure 5.5 show the experimental and simulated deformation patterns of tests number (S-59) and (F-30) and the crush load-displacement curves of tests number (S-59), (S-60), (F-30) and (F-31). The typical bending deformation of the beam can be seen: an inward fold at the compression flange and two outward folds at the adjacent flanges. The formation of inward and outward folds as well as the rupture of the beam walls result in a decrease of the plastic resistance of the beam. It can also be seen that the deformation modes are well described by the simulations. The agreement between the crush load-displacement curves in the tests and simulations is acceptable. The simulated maximum force is a bit overestimated, while the curve after the peak load is underestimated. This is in agreement with Hanssen et al. (2002) [42] and Rayes et al. (2004) [83].

The energy absorption *E*, which is the area under the crush load-displacement curve, and the specific energy absorption *SEA*, which is the ratio of the absorbed energy and the crash mass of the structure, of the experimental tests are presented in Table 5.2. Here, for every identical test the averages of two repetitions are calculated. It can be seen that at the same test conditions, not only the foam-filled beams absorb more energy than empty beams but also they have higher specific energy absorption. This means more energy is absorbed with less weight.

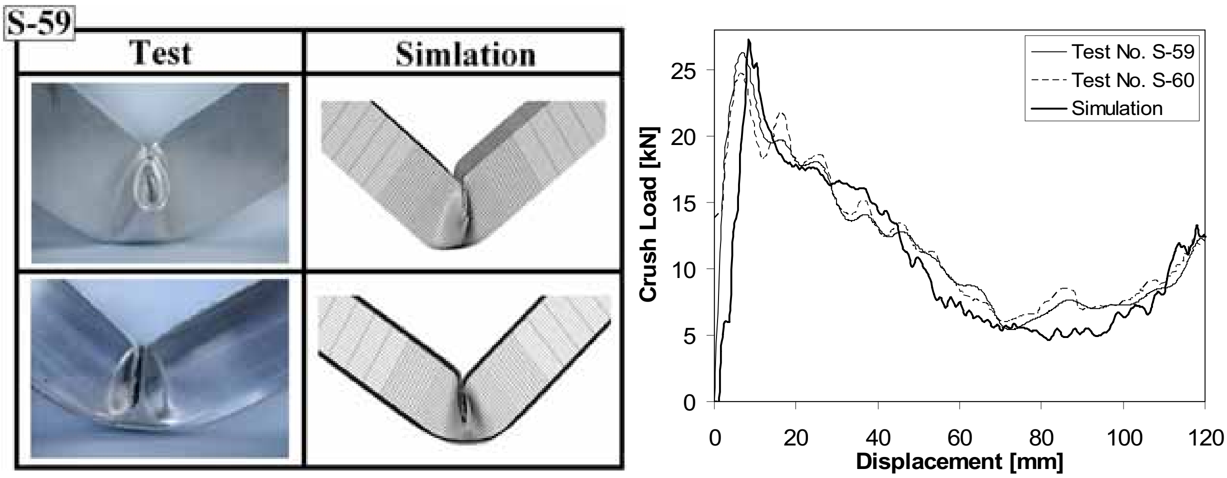

Figure 5.4: Experimental and numerical crush pattern (left) and crush load-displacement curves (right) of empty tube AlMgSi0.5F22

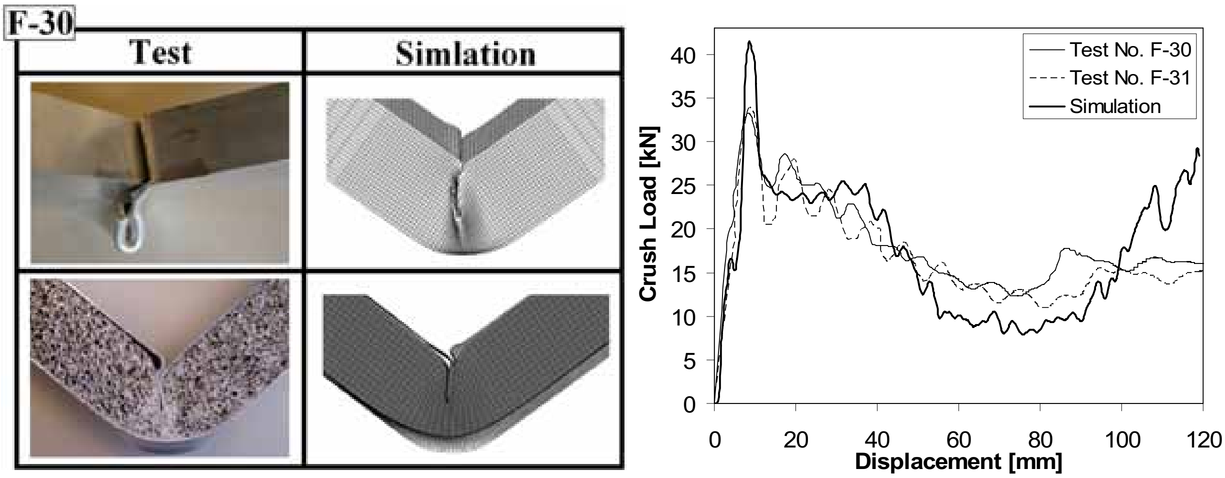

Figure 5.5: Experimental and numerical crush pattern (left) and crush load-displacement curves (right) of foam-filled tube AlMgSi0.5F22 and Alporas foam with relative density of 0.085

Table 5.2: Experimental energy absorption and specific energy absorption

Test No.	Filler type	E [J]	Increase	SAE [J/kg]	Increase [%]
Average of S59 and 60	-	864	-	1374	-
Average of F-30 and 31	Foam	1136	31.5	1409	2.6
Average of S-61 and 62	-	454	-	722	-
Average of F32 and 33	Foam	610	34.4	757	4.8
Average of S-63 and 64	-	936	-	1488	-
Average of F-34 and 35	Foam	1262	34.8	1566	5.2

5.4 Crashworthiness optimization of empty and filled beams under bending load

The implementation of the multi design optimization *MDO* in crashworthiness improvement of aluminum tubes under axial crush load has been already examined previously [125]. Here, in order to find the best tube dimensions, the optimization procedure is applied to maximize the specific energy absorption *SEA* of the square beams under bending load with a target energy absorption E_{goal}. The feasible range of the wall thickness t is between 0.5-3.5 mm, which is practical for aluminum automotive structures. Here, the target value E_{goal}= $3000 \pm 50\ J$ is selected for energy absorption. First the optimization procedure is applied to find the empty beam width and thickness that absorbed 3000 ± 50 J energy and has minimum weight. The optimization problem can be rewritten as follows

Minimize tube weight (Maximize the specific energy absorption *SEA*) Subjected to

$$\begin{aligned} & E \geq E_{goal}, \\ & 0.5 \text{ mm} \leq t \leq 3.5 \text{ mm}, \\ & 50 \text{ mm} \leq d \leq 120 \text{ mm}. \end{aligned} \tag{5-22}$$

The optimization procedure should be applied to find the optimum beam thickness and width. The design variables for beams are selected and impact simulations are performed. The *RSM* is used to approximate absorbed energy and the specific absorbed energy as non linear second order polynomials. Then the approximative subproblem is solved by a genetic algorithm optimization method which is provided in [75]. The optimization procedure shows that the tube thickness has the main effect on the energy absorption of the tubes while the tube width has lower influence. Taking into account the production costs, the thickness higher than 3.5 mm is not considered. The result of the final optimized beam that absorbs at least target energy and has minimum weight is presented in Table 5.3. Here, the optimum tube thickness is aligned with the upper limit of the optimization procedure. That means, although some damages are created in the beam walls, still tube thickness plays the most important role in the energy absorption of the beam.

Table 5.3: Optimized empty aluminum beam AlMgSi0.5F22

Tube type	d [mm]	t [mm]	P_{max} [kN]	E [J]	SEA [J/kg]
Optimum empty tube	77	3.5	50.9	3017	1949

To continue the optimization investigation, effort is done to find the optimum foam and beam combinations which absorb the same energy as the optimum empty beam and have minimum weight. Chen et al. (2002) [17] used their original developed formulas, Equations (5-7)-(5-16), to estimate the crush performance of empty and foam-filled tubes for relatively low bending rotation. Based on the predicted crush behavior, they found the optimum foam-filled combinations. Their optimum filled beam showed a thinner cross section in addition to less weight compared to the empty tube. The disadvantage of this method is the need to determine the flow stresses of the beam and foam materials and also the value of the ΔM has to be known. They used comprehensive finite element simulation to find the ΔM values for every foam density. But still their method can not predict the crush behavior of the tube for large bending rotation. These models are valid only for small rotation angles where no damage is created and no touching is taken place between the beam walls.

To find the exact optimum foam-filled combination under dynamic bending load and for the real word problems where the beam undergoes very high rotation angles, the same optimization procedure presented in section 2.7 is implemented to optimize the crush performance of the foam-filled beams. Since the foam gives additional support to the tube walls, at the same tube dimensions, the bending strength of the foam-filled would be higher than the empty tube. In the optimization procedure, the feasible range of the wall thickness t is between 0.5-3.5 mm. For the density of the foam, values between 50-540 kg/m^3 are used as new optimization parameter. The existing semi analytical formulas [33] are used to determine the foam properties for every foam density. The optimization procedure is applied to find the optimum foam-filled beam that absorbed the target energy and has minimum weight. Figure 5.6 shows the energy absorption and specific energy absorption of foam-filled beams in the last optimization iteration. This figure shows the variation of the energy absorption and specific energy absorption of the square aluminum beams against variation of the beam width and foam density. Here, the thickness of 3.5 mm is selected for the beams. It can be seen that a higher value of the beam width and foam density increase the energy absorption of the filled beam. The diagram of the specific energy absorption indicates that there is one optimum foam density. When the foam density lower or higher than this optimum value is selected, the specific energy absorption is decreased.

Finally, the optimization procedure is implemented and the optimum foam-filled beam is determined. Table 5.4 shows the results of optimum foam-filled beam. It can be seen that a th-

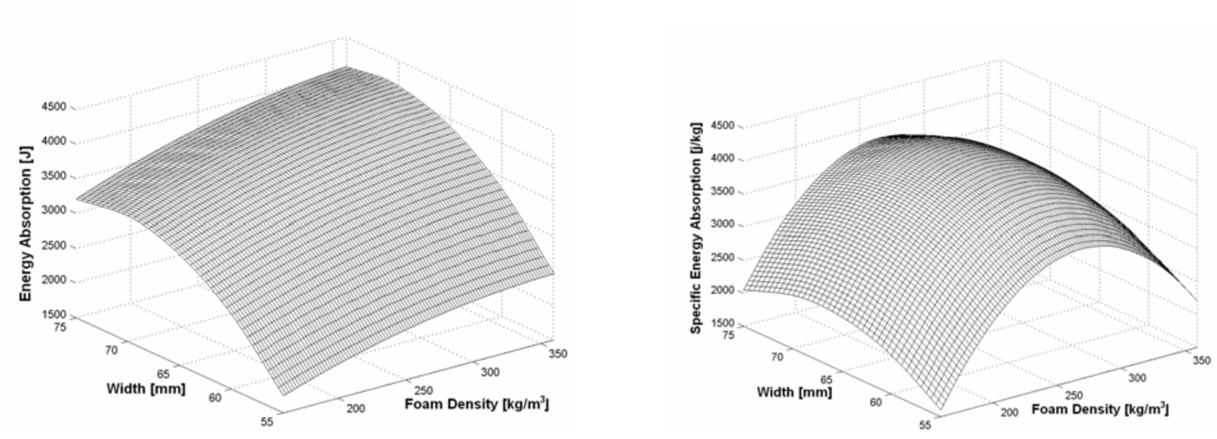

Figure 5.6: Approximative response surface of the energy absorption (left) and specific energy absorption (right) of the foam-filled beam with the thickness of 3.5 mm

-inner and smaller beam can be used in the case of foam-filled beams. The foam-filled beam absorbed the same energy as the optimum empty tube but it has 28.1 % lower weight. The comparison between maximum crush load P_{max} in the Table 5.3 and Table 5.4 shows that the optimum foam-filled beam has higher maximum crush load than the optimum empty beam. This increase is as a result of the extra support of foam filler to the beam [128].

Figure 5.7 shows the final crush pattern of optimum empty and foam-filled beams. Here, the empty beam has an inward fold at the compression side and two outward folds at the adjacent flanges, while the localized crushing is retarded as result of the presence of the foam filler in the filled beam.

As mentioned before, the fracture is modeled with the use of element elimination method in beam wall and foam. As the beam wall or foam material starts to fracture, their bending resistance decrease considerably. Here, more rupture can be seen in the tube walls in the optimum empty beam than filled one. From the figure of the optimum foam-filled beam it can be studied how the foam filler deforms and provides extra support to the tube walls.

Due to the localized behavior of the beams under bending load, the foam can be applied only at the crush zone. This concept was investigated numerically and experimentally by Santosa et al. [94]. They presented a formula to calculating the effective filling length l_f,

$$l_f = l\left(\frac{\eta_f - 1}{\eta_f}\right) - 2H. \tag{5-23}$$

Where $\eta_f = M_f/M$ is the ratio between the ultimate bending moment of the filled section and the empty section; H is the half wavelength. In the above optimization procedure the actual deformed length of the foams are considered as effective filling length.

Table 5.4: Optimum foam-filled square beam AlMgSi0.5F22 and Alporas foam

Tube type	d [mm]	t [mm]	ρ_f [kg/m^3]	P_{max} [kN]	E [J]	SEA [J/kg]	Increase [%]
Optimum Foam-filled	64	3.11	281	53.2	3028	2498	28.1

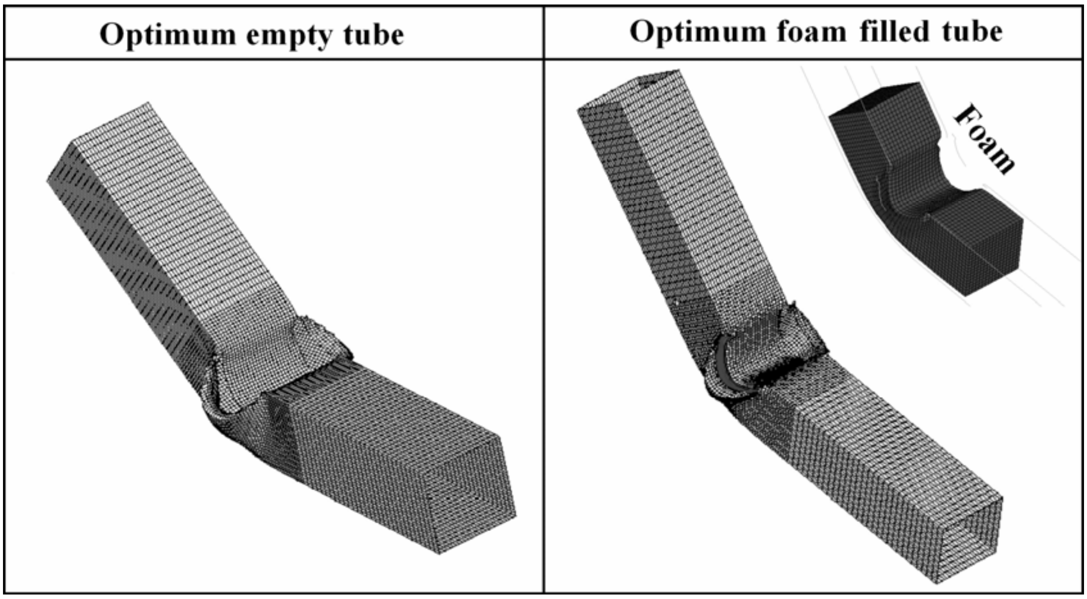

Figure 5.7: Crush patterns of the optimum empty and foam-filled tube AlMgSi0.5F22 and Alporas foam

6. Crashworthiness investigation and optimization of composite crash box

6.1 Introduction to the crush behavior of composite crash box

Metallic and composite columns are used in a broad range of automotive and aerospace applications and especially as crash absorber elements. In automotive application, crashworthy structures absorb impact energy in a controlled manner. Thereby, they bring the passenger compartment to rest without subjecting the occupant to high decelerations. Energy absorption in metallic crash absorbers normally takes place by progressive buckling and local bending collapse of columns wall. A distinctive feature of such a deformation mechanism is that the rate of energy dissipation is concentrated over relatively narrow zones, while the other part of the structure undergoes a rigid body motion. In comparison to metals, most composite columns crush in a brittle manner and they fail through a sequence of fracture mechanism involving fiber fracture, matrix crazing and cracking, fiber-matrix debonding, delamination and internal ply separation. The high strength to weight and stiffness to weight ratios of composite materials motivated the automobile industry to gradual replacement of the metallic structures by composite ones. The implementation of composite materials in the vehicles not only increases the energy absorption per unit of weight [82] but also reduces the noise and vibrations, in comparison with steel or aluminum structures [100]. The crashworthiness of a crash box is expressed in terms of its energy absorption *E* and specific energy absorption *SEA*. The energy absorption performance of a composite crash box can be tailored by controlling various parameters like fiber type, matrix type, fiber architecture, specimen geometry, process condition, fiber volume fraction and impact velocity. A comprehensive review of the various research activities have been conducted by Jacob et al. (2002) [50] to understand the effect of particular parameter on energy absorption capability of composite crash boxes.

The response of composite tubes under axial compression has been investigated by Hull (1982) [47]. He tried to achieve optimum deceleration under crush conditions. He showed that the fiber arrangement appeared to have the greatest effect on the specific energy absorption. Farley (1983) [24] and (1991) [25] conducted quasi-static compression and impact tests to investigate the energy absorption characteristics of the composite tubes. Through his experimental work, he showed that the energy absorption capabilities of Thornel 300-fiberite and Kevlar-49-fiberite 934 composites are a function of crushing speed. He concluded that strain rate sensibility of these composite materials depends on the relationship between the mechanical response of the dominant crushing mechanism and the strain rate. Hamada and Ramakrishna (1997) [38] also investigate the crush behavior of composite tubes under axial compression. Carbon polyether etherketone (PEEK) composite tubes were tested quasi-statically and dynamically showing progressive crushing initiated at a chamfered end. The quasi-statically tested tubes display higher specific energy absorption as a result of different crushing mechanisms attributed to different crushing speeds. Mamalis et al. (1997) [68] and (2005) [69] investigated the crush behavior of square composite tubes subjected to static and dynamic axial compression. They reported that three different crush modes for the composite tubes are included, stable progressive collapse mode associated with large amounts of crush energy absorption, mid-length collapse mode characterized by brittle fracture and catastrophic failure that absorbed the lowest energy. The load-displacement curves for the static testing exhibited typical peaks and valleys with a narrow fluctuation amplitude, while the curves for the dynamically tested specimens were far more erratic. Later Mamalis et al. (2006) [70] investigated the crushing characteristics of thin walled carbon fiber reinforced plastic CFRP tubular components. They made a comparison between the quasi-static and dynamic energy absorption capability of square CFRP.

The high cost of the experimental test and also the development of new finite element codes make the design by means of numerical methods very attractive. Mamalis et al. (2006) [70] used the explicit finite element code LS-DYNA to simulate the crush response of square CFRP composite tubes. They used their experimental results to validate the simulations. Results of experimental investigations and finite element analysis of some composite structures of a Formula One racing car are presented by Bisagni et al.(2005) [15]. Hörmann and Wacker (2005) [46] used LS-DYNA explicit code to simulate modular composite thermoplastic crash boxes. El-Hage et al. (2004) [20] used finite element method to study the quasi-static axial crush behavior of aluminum/composite hybrid tubes. The hybrid tubes contain filament wound E glass-fiber reinforced epoxy over-wrap around an aluminum tube.

This study deals with experimental and numerical crashworthiness investigations of square and hexagonal composite crash boxes. Drop weight impact tests have been conducted on composite crash boxes and finite element method used to find detail information about crush process.

6.2 Experimental and numerical results

Axial impact tests were conducted on square and hexagonal composite crash boxes. The nominal wall thicknesses of the composite tubes are 2 mm, 2.4 mm and 2.7 mm. Square tubes with length of 150 mm and hexagonal tube with the length of 91 mm are used, see Figure 6.1. The specimens are made from woven fiberglass/polyamide, approximately 50% volume fiber. Equal amount of fibers are in the two perpendicular main orientations. They are produced by Jacob Composite GmbH. Similar tubes are used in the bumper system of the BMW M3 E46 as well as E92 and E93 model as crash boxes.

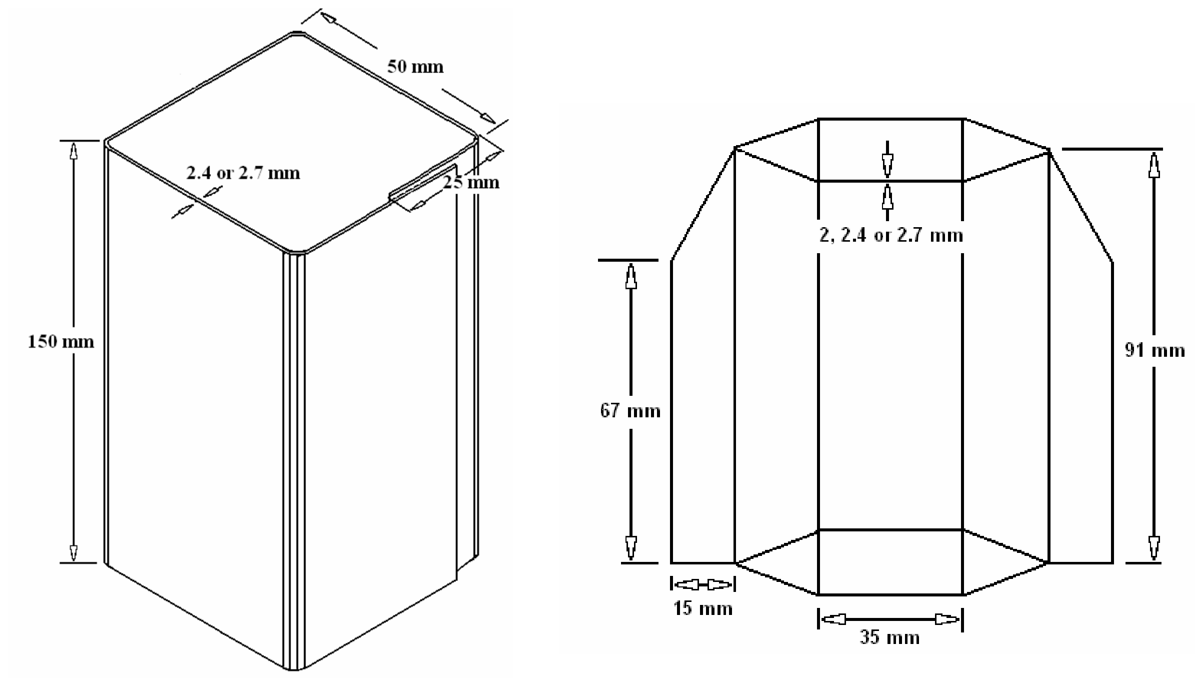

Figure 6.1: Square crash box (left) Hexagonal crash box (right)

A 45 degree trigger was created at the top end of the specimens. Generally injection moulding can be used to produce complex reinforced thermoplastics parts with low fiber length/fiber diameter aspect ratio. With increasing aspect ratio the crush performance increases but the flow ability of the material decreases. For this reason continuous reinforced thermoplastic have to be thermoformed. In this way and by using other post processing technologies like welding, complex composite parts with an excellent crush performance can be realized [46]. Here, the crash boxes are produced from thermoplastic plates by using thermoforming technique. The square specimens have overlap in one side and the overlaps have been glued by using a structural adhesive. The hexagonal crash boxes consist of two parts that are welded to each other.

The experimental tests were conducted on the drop test rig, see Figure 3.5. An impact mass of 92 kg was selected. The interest in this study is the mean crush load P_m and the energy absorption E.

Numerical simulations of crash tests are performed to obtain local information from the crush process. The modeling and analysis is done with the use of explicit finite element code, LS-DYNA. The column walls are built with the Belytschko-Tsay thin shell elements and solid elements are used to model the impactor. The contact between the rigid body and the specimen is modeled using a node to surface algorithm with a friction coefficient of $\mu = 0.2$. To take into account the self contact between the tube walls during the deformation, a single surface contact algorithm is used. The impactor has been modeled with the rigid material. The composite walls have been modeled with the use of material model #54 in LS-DYNA. This model has the option of using either the Tsai-Wu failure criterion or the Chang-Chang failure criterion for lamina failure. The Tsai-Wu failure criterion is a quadratic stress-based global failure prediction equation and is relatively simple to use; however, it does not specifically consider the failure modes observed in composite materials [67]. Chang-Chang failure criterion [16] is a modified version of the Hashin failure criterion [43] in which the tensile fiber failure, compressive fiber failure, tensile matrix failure and compressive matrix failure are separately considered. Chang and Chang modified the Hashin equations to include the non-linear shear stress-strain behavior of a composite lamina. They also defined a post-failure degradation rule so that the behavior of the laminate can be analyzed after each successive lamina fails. According to this rule, if fiber breakage and/or matrix shear failure occurs in a lamina, both transverse modulus and minor Poisson's ratio are reduced to zero, but the change in longitudinal modulus and shear modulus follows a Weibull distribution. On the other hand, if matrix tensile or compressive failure occurs first, the transverse modulus and minor Poisson's ratio are reduced to zero, while the longitudinal modulus and shear modulus remain unchanged. The failure equations selected for this study are based on the Chang-Chang failure criterion. However, in material model #54, the post-failure conditions are slightly modified from the Chang-Chang conditions. For computational purposes, four indicator functions e_f, e_c, e_m, e_d corresponding to four failure modes are introduced. These failure indicators are based on total failure hypothesis for the laminas, where both the strength and the stiffness are set equal to zero after failure is encountered,

(a) Tensile fiber mode (fiber rupture),

$$\sigma_{aa} > 0, \;\; and \quad e_f^2 = \left(\frac{\sigma_{aa}}{X_t}\right)^2 + \varsigma\left(\frac{\sigma_{ab}}{S_c}\right)^2 - 1\begin{cases} \geq 0 & \Rightarrow \text{failed,} \\ < 0 & \Rightarrow \text{elastic.}\end{cases} \tag{6-1}$$

Where ζ is a weighting factor for the shear term in tensile fiber mode and $0<\zeta<1$. $E_a = E_b = G_{ab} = \upsilon_{ab} = \upsilon_{ba} = 0$ after lamina failure by fiber rupture.

(b) Compressive fiber mode (fiber buckling or kinking),

$$\sigma_{aa} < 0, \;\; and \quad e_c^2 = \left(\frac{\sigma_{aa}}{X_c}\right)^2 - 1\begin{cases} \geq 0 & \Rightarrow \text{failed,} \\ < 0 & \Rightarrow \text{elastic.}\end{cases} \tag{6-2}$$

$E_a = \upsilon_{ab} = \upsilon_{ba} = 0$ after lamina failure by fiber buckling or kinking.

(c) Tensile matrix mode (matrix cracking under transverse tension and in-plane shear),

$$\sigma_{bb} > 0, \;\; and \quad e_m^2 = \left(\frac{\sigma_{bb}}{Y_t}\right)^2 + \varsigma\left(\frac{\sigma_{ab}}{S_c}\right)^2 - 1\begin{cases} \geq 0 \Rightarrow \text{failed,} \\ < 0 \Rightarrow \text{elastic.}\end{cases} \tag{6-3}$$

$E_b = \upsilon_{ab} = G_{ab} = 0$ after lamina failure by matrix cracking

(d) Compressive matrix mode (matrix cracking under transverse compression and in-plane shear),

$$\sigma_{bb} < 0, \ \ and \qquad e_d^2 = \left(\frac{\sigma_{bb}}{2S_c}\right)^2 + \left[\left(\frac{Y_c}{2S_c}\right)^2 - 1\right]\frac{\sigma_{bb}}{Y_c} + \left(\frac{\sigma_{ab}}{S_c}\right)^2 - 1 \begin{cases} \geq 0 \Rightarrow \text{failed,} \\ < 0 \Rightarrow \text{elastic.} \end{cases} \quad (6\text{-}4)$$

$E_b = \upsilon_{ba} = \upsilon_{ab} = 0 \rightarrow G_{ab} = 0$ after lamina failure by matrix cracking

In Equations (6-1)–(6-4), σ_{aa} is the stress in the fiber direction, σ_{bb} is the stress in the transverse direction (normal to the fiber direction) and σ_{ab} is the shear stress in the lamina plane *aa-bb*. The other lamina-level notations in Equations (6-1)–(6-4) are as follows: X_t and X_c are tensile and compressive strengths in the fiber direction, respectively. Y_t and Y_c are tensile and compressive strengths in the matrix direction, respectively. S_c is shear strength; E_a and E_b are Young's moduli in the longitudinal and transverse directions, respectively. Here, to model the trigger, two elements with progressively reduced thicknesses were placed in the triggers zone. The tied surface to surface contact algorithm has been used to glue the overlapping walls.

Tables 6.1 and 6.2 show the test results of the square and hexagonal composite tubes [129]. Here, the area under crush load-displacement curve is considered as energy absorption *E*. The maximum crush load P_{max} is a single peak at the end of the initial linear part of the load curve. The mean crush load P_m has been determined with the use of Equation (3-11). The maximum crush displacement S_{max} is the total displacement of the impactor after contact with the crash box. The values of specific energy absorption *SEA*, which is the energy absorption per crush weight, and the crush load efficiency η, which is the ratio of the mean crush load and maximum crush load, are also presented in these tables. Figure 6.2 shows the specimen (S-67) and (S-75) after crush, respectively. Relatively ductile crush mode can be recognized. The tubes are split at their corners. This splitting effect is initiated at the end of the linear elastic loading phase, when the applied load attains its peak value P_{max}. The splitting of the corners of the tube is followed by an immediate drop of the crush load, and propagation parallel to the tube axis results in splitting of the tube in several parts. Simultaneous of splitting, some of these parts are completely splayed into two fronds which spread outwards and inwards and some parts are split only partially. Subsequent to splitting, the external and internal fronds are bended and curled downwards and some additional transverse and longitudinal fracture happened. Photographs from high speed camera for different impact moments are presented in Figures 6.3 and 6.4. Here it can be seen that local matrix and fiber rupture results in a formation of pulverized ingredients material just after initial contact between impactor and crash boxes. As compressive loading proceeds, further fragments are detached from the crash box.

Furthermore, the crush performance of tests has been simulated with the use of LS-DYNA explicit code. Figure 6.5 shows the experimental and simulated crush load-displacement and energy absorption-displacement curves of tests (S-67) to (S-69). The same results for hexagonal crash boxes, tests (S-75) to (S-77), are presented in Figure 6.6. The crush-load displacement curves indicate that the mean crush load of simulation is obviously lower than experimental results. The numerical simulation can not cover the experiments very good.

Table 6.1: Experimental dynamic test on square composite tube

Test No.	V [m/s]	t [mm]	P_{max} [kN]	P_m [kN]	S_{max} [mm]	E [J]	SEA [J/kg]	η [%]
S-67	10.3	2.4	77.2	40.6	126.9	4956	41844	53
S-68	10.4	2.4	75.3	46.03	118.9	5053	45533	61
S-69	10.2	2.4	83.7	43.3	117.3	4923	44967	52
S-70	10.4	2.7	82.2	58.7	86.2	5075	55542	71
S-71	10.4	2.7	92.3	59.3	84.7	5024	55957	64

Table 6.2: Experimental dynamic test on hexagonal composite tube

Test No.	V [m/s]	t [mm]	P_{max} [kN]	P_m [kN]	S_{max} [mm]	E [J]	SEA [J/kg]	η [%]
S-72	7.3	2.0	51	42.6	72.8	3103	35681	83
S-73	7.3	2.0	55	45.5	68.3	3109	35750	83
S-74	7.3	2.0	46	37.9	78.2	2964	34083	82
S-75	8.4	2.4	72	53.7	76.95	4133	39604	75
S-76	8.4	2.4	81	69.4	61.03	4235	40582	86
S-77	8.9	2.4	72	65.6	71.4	4683	44875	91
S-78	8.3	2.7	83	66.9	59.96	4012	34173	81
S-79	8.3	2.7	80	68.4	58.6	4008	34139	86
S-80	8.8	2.7	84	58.8	75.5	4442	37836	70

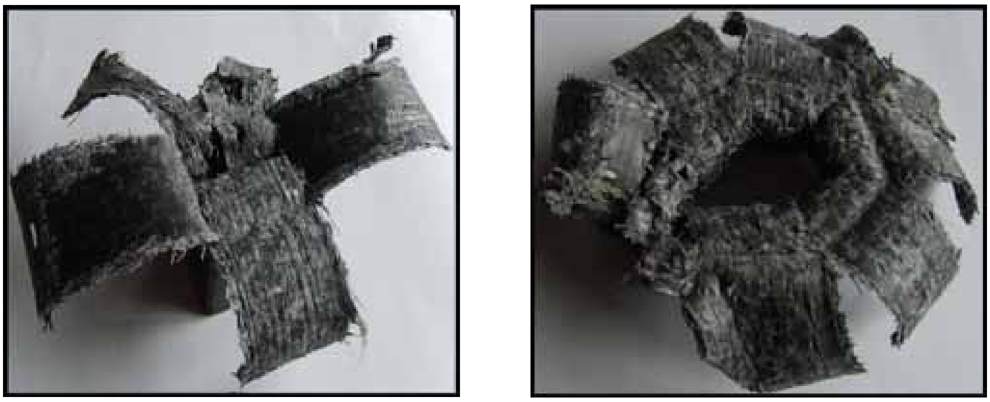

Figure 6.2: Crush pattern of square tube S-67 (left) and hexagonal tube S-75 (right)

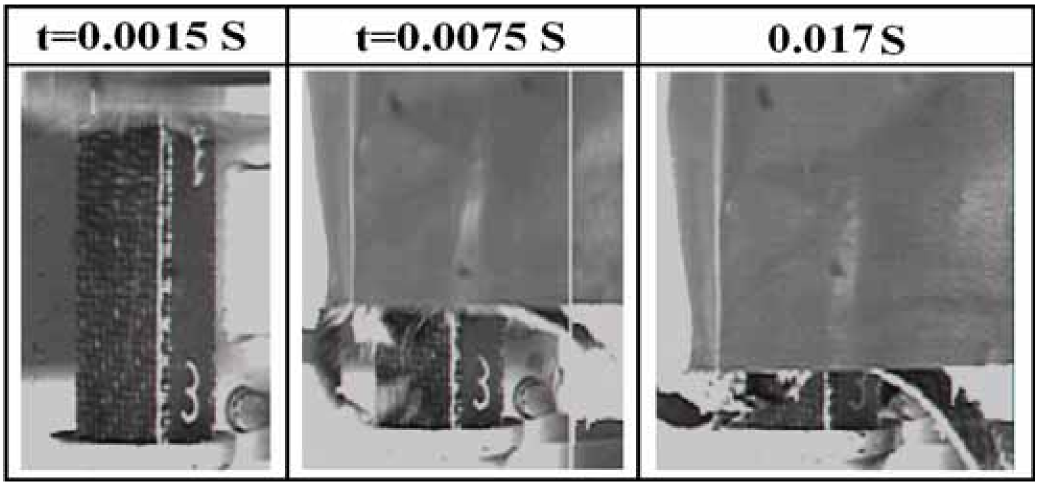

Figure 6.3: Crush pattern of a square composite tube (S-67) for different crush moments

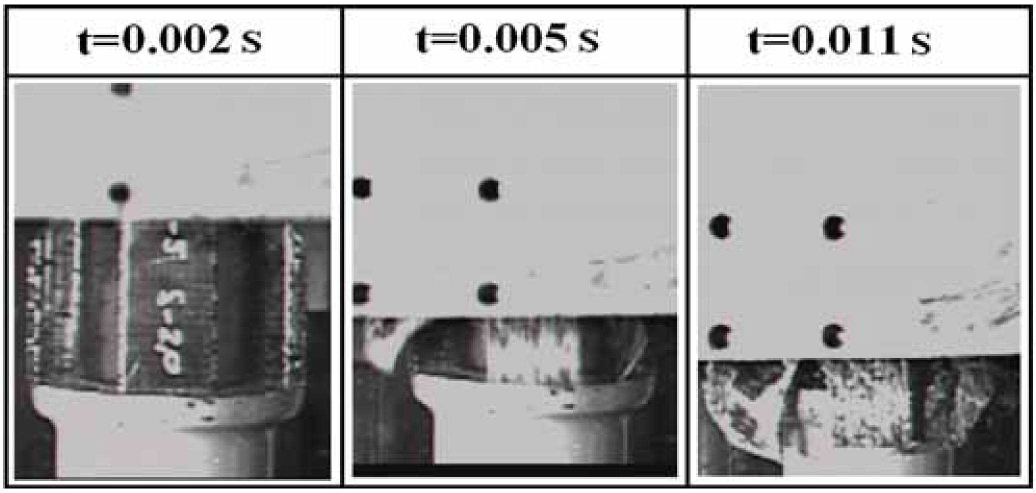

Figure 6.4: Crush pattern of a hexagonal composite tube (S-75) for different crush moments

The energy absorption *E* and specific energy absorption *SEA* of the experiments and simulations at the same crush length (80 mm for square tubes and 60 mm for hexagonal ones) are presented in Table 6.3. Here, index *S* indicates simulation results. Again, it can be seen that the numerical simulations highly underestimate the tube crush behavior. The numerical crush patterns show the tube experiences the progressive crushing with some damages in tube walls instead of splitting and spreading, see Figure 6.7 and 6.8. It is evident that the total energy absorption of the composite tube is the sum of the energy needed for splitting of the tube corners, delamination and spreading of tube walls into two inwards and outwards fronds, bending and curling of each fronds, fracture and damage created in fronds during bending, fragmentations of tube walls and friction between the impactor and inwards and outwards fronds. The single layer finite element model does not have the capability to consider all aspects of crushing damages observed experimentally. Therefore, a new finite element model has to be developed to overcome this problem.

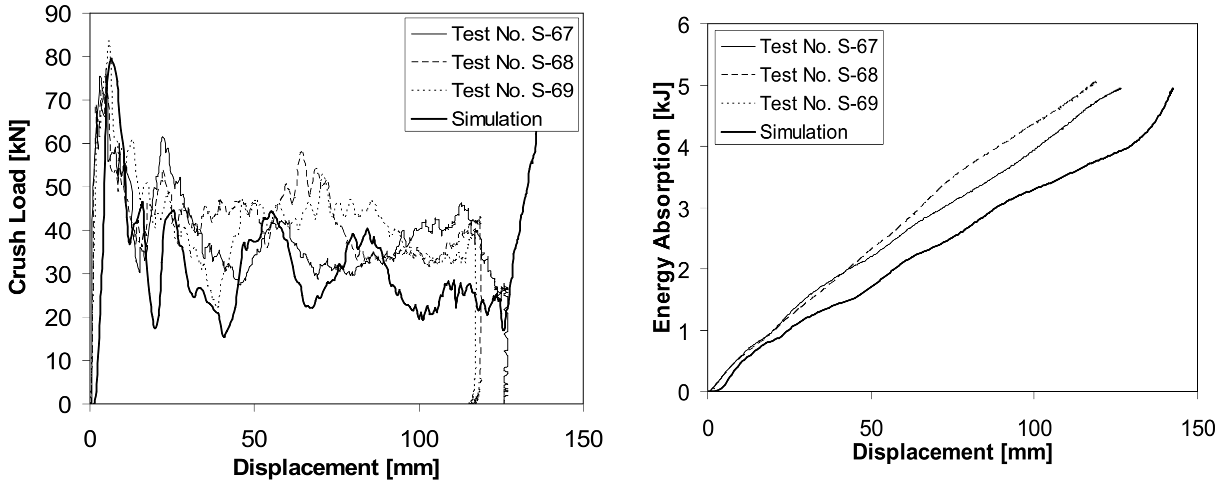

Figure 6.5: Comparison between experimental and numerical (single layer method) crush load-displacement curves (left) and energy absorption-displacement curves (right) of square composite tubes

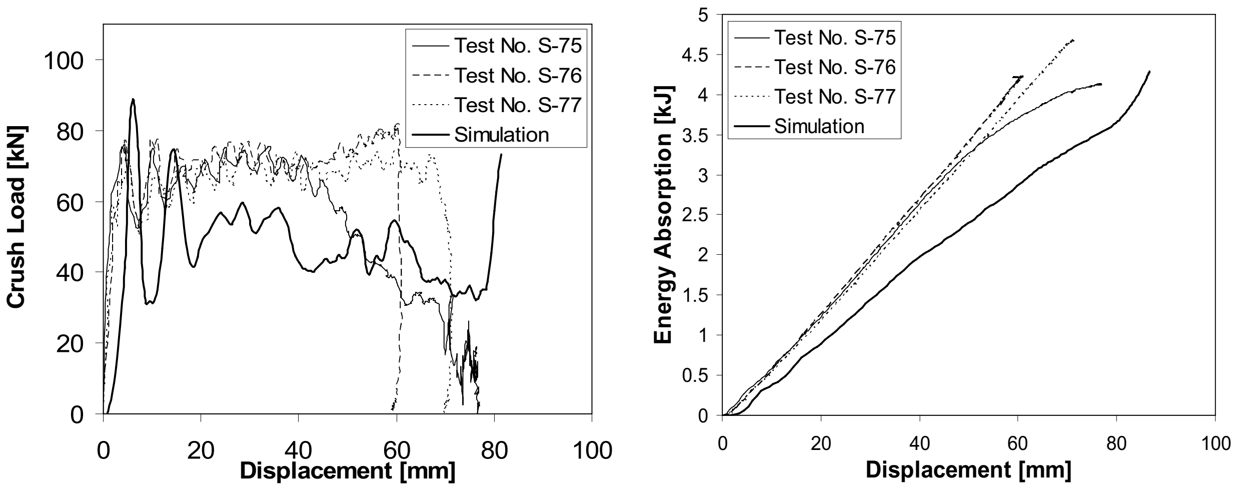

Figure 6.6: Comparison between experimental and numerical (single layer method) crush load-displacement curves (left) and energy absorption-displacement curves (right) of hexagonal composite tubes

Table 6.3: Comparison between experimental and numerical (single layer method) energy absorption and specific energy absorption of the square and hexagonal tubes

Test No.	E [J]	SEA [J/kg]	E_s [J]	SEA_S [J/kg]	Difference [%]
S-67	3259	43647	2686	35973	-17.6
S-68	3682	49313	-	-	-27.1
S-69	3520	47143	-	-	-23.7
S-75	3718	54035	2890	42002	-22.3
S-76	4170	60604	-	-	-30.7
S-77	3930	57116	-	-	-26.5

6.3 Advanced finite element model

The numerical crush behavior of the composite crash box are shown above for tube walls modeled with only one layer of shell elements, simulated crush pattern are quite different from experiment. The delamination, a main energy absorption source of composite crash boxes, can not be modeled and, therefore, the predicted energy absorption by the simulation is highly underestimated. Several methods have been used by the researchers to model the delamination growth in composite materials, including the virtual crack extension technique [26], stress intensity factor calculations [38], stresses in a resin layer [55], and, the virtual crack closure technique [30].

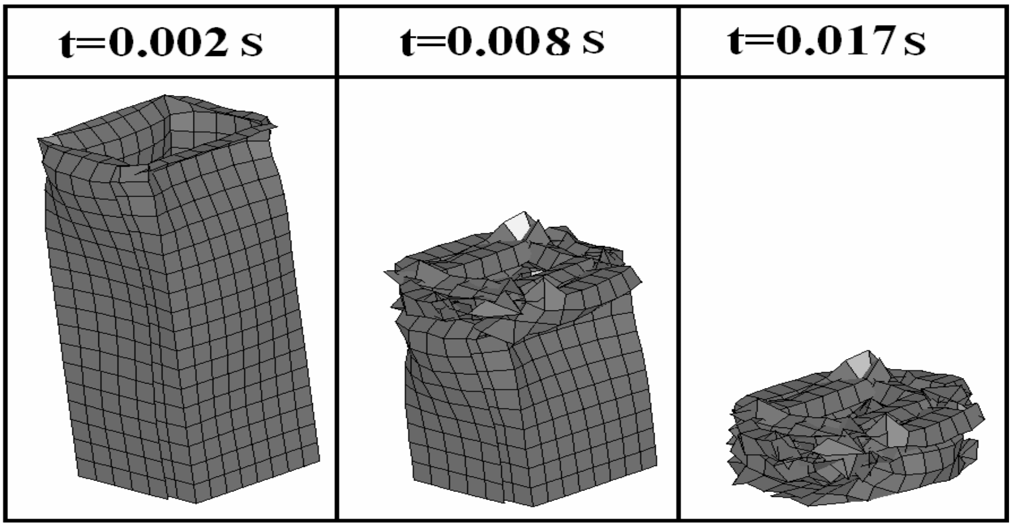

Figure 6.7: Crush pattern of single layer finite element model of square composite tube

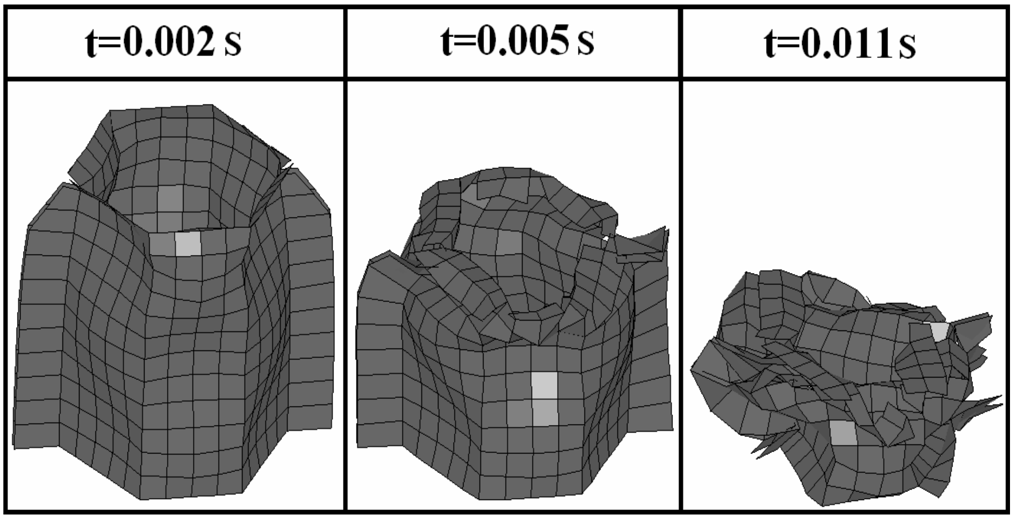

Figure 6.8: Crush pattern of single layer finite element model of hexagonal composite tube

However, choices for modeling delamination using conventional finite element crush codes are more limited. Good correlations are obtained in many cases using models that do not fully capture all aspects of crushing damage observed experimentally. They only provide sufficient attention to the aspects of crushing that mostly influence the response. Models of composite structures using in-plane damaging failure models to represent crushing behavior are used in [44], [51], [52], [56]. These models appear to be effective for structures whose failure modes are governed by large-scale laminate failure and local instability. However, crushing behavior in which wholesale destruction of the laminate contributes significantly to the overall energy absorption cannot be accurately modeled by this approach [31]. Further, if delamination or debonding forms a significant part of the behavior, specialized procedures must be introduced into the model to address this failure mechanism [56]. Kerth et al. (1996) [54] used tied connections with a force-based failure method to model the delamination in composite materials. By this method, nodes on opposite sides of an interface where delamination is expected are tied together using any of a variety of methods including spring elements or rigid rods. If the forces produced by these elements exceed some criterion, the constraint is released. The primary disadvantage of this method is that there is no strong physical basis for determining the failure forces. Reedy et al. (1997) [88] applied cohesive fracture model for the same reason. This method is similar to the previous method. However, instead of relying on simple spring properties the force-displacement response of the interfacial elements is based on classical cohesive failure behavior. Virtual crack closure technique is often used by researchers in the area of fracture mechanics. Energy release rates are calculated from nodal forces and displacements in the vicinity of a crack front. Although the method is sensitive to mesh refinement, but not so sensitive like the other fracture modeling techniques, those requiring accurate calculation of stresses in the singular region near a crack front. Further, the use of conventional force and displacement variables obviates the need for special element types that are not available in conventional crash codes.

In this study for the delamination, tube walls are modeled with two layers of shell elements. The thickness of each layer is equal to the half of the tube wall thickness [130]. To avoid tremendous increase of the required simulation time, a larger number of layers is avoided. The surface to surface tiebreak contact is used to model the bonding between the bundles of plies of the tube walls. In this contact algorithm the tiebreak is active for nodes which are initially in contact. Stress is limited by the perfectly plastic yield condition. For ties in tension, the yield condition is

$$\frac{\sqrt{\sigma_n^2 + 3\left|\sigma_s\right|^2}}{\varepsilon_p} \leq 1. \tag{6-5}$$

Where ε_p is the plastic yield stress and σ_n and σ_s are normal and shear stresses, respectively.

For ties in compression, the yield condition is

$$\frac{\sqrt{3|\sigma_s|^2}}{\varepsilon_p} \le 1. \tag{6-6}$$

The stress is also scaled by a damage function. The damage function is defined by a load curve with starts at unity for crack width of zero and decays in some way to zero at a given value of the crack opening [37], see Figure 6.9. The surface to surface tied contact is implemented between the overlapped walls and single surface contact is used for each layer. The node to surface contact is applied between rigid impactor and composite layers. To model the rupture at the corners of the tube, the vertical sides of the tube have offset 0.5 mm and deformable spot-welds are used to connect the nodes of the vertical sides. The spot-welds are defined by the use of material number #100 in LS-DYNA (MAT_SPOTWELD). Based on this material model, beam elements, based on Hughes-Liu beam formulation, are placed between the tube walls and contact-spotweld algorithm ties the beam elements to the tube shell elements. The normal strength of spot-welds is calculated from the transverse tensile strength of the composite material. To account for the reduced strength of the composite material at the corners, material strength is reduced by 50%. The shear strength is considered as half of the normal strength. In order to model the trigger, the length of the outer layer of the composite tube is a little bit smaller than the inner layer. The crush patterns of the multi layer square and hexagonal crash boxes are presented in Figures 6.10 and 6.11. Here it is possible to see the delamination which starts in some tube walls and propagates during the crush process. The Figures 6-12 and 6-13 left compare the crush load-displacement curves of experimental and numerical impact on square and hexagonal crash boxes, respectively. Acceptable correlations are reached between experiments and simulations. In addition the experimental and numerical energy absorption is presented in Figure 6.12 and Figure 6.13 right. The multi layers method can predict the energy absorption of the crash box very well.

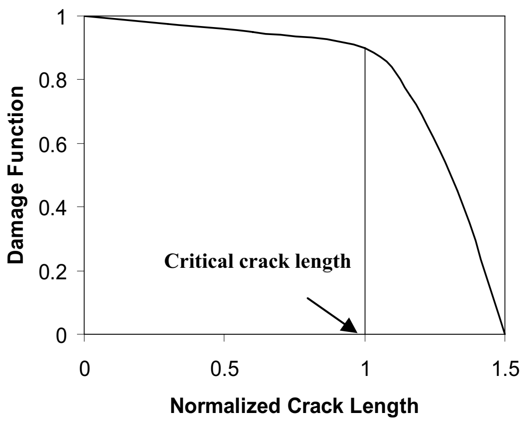

Figure 6.9: Variation of damage function

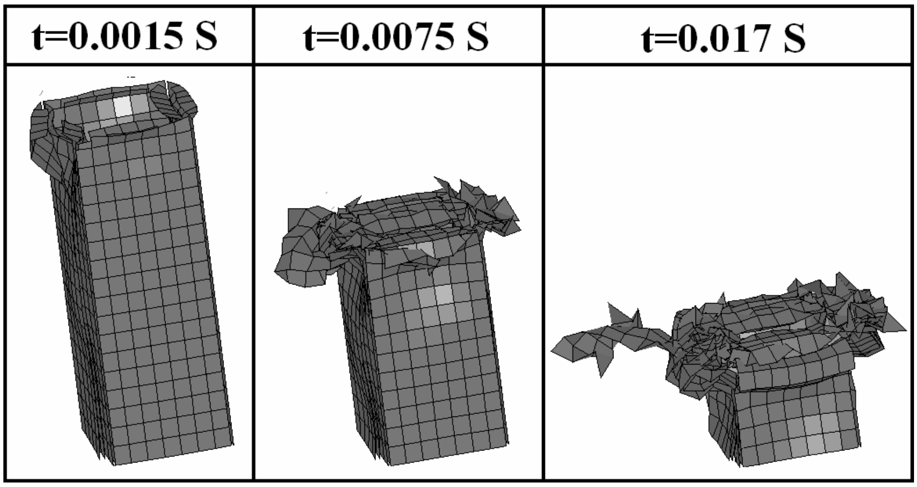

Figure 6.10: Crush pattern of multi layer finite element model of square compos ite tube

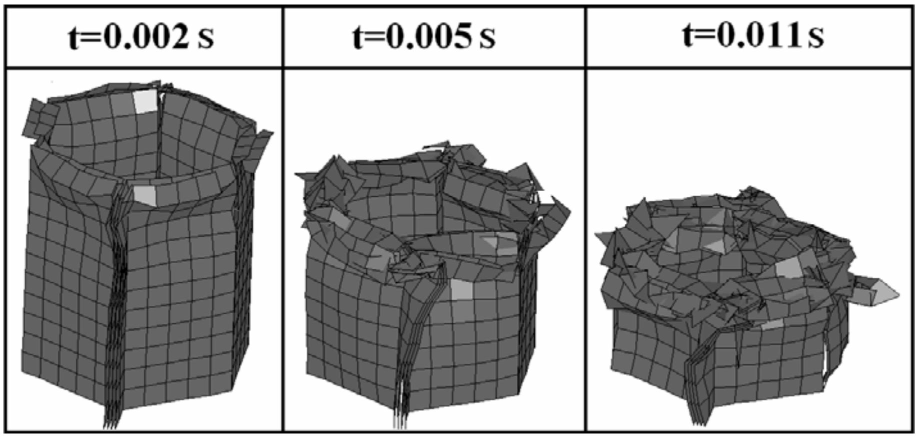

Figure 6.11: Crush pattern of multi layer finite element model of hexagonal composite tube

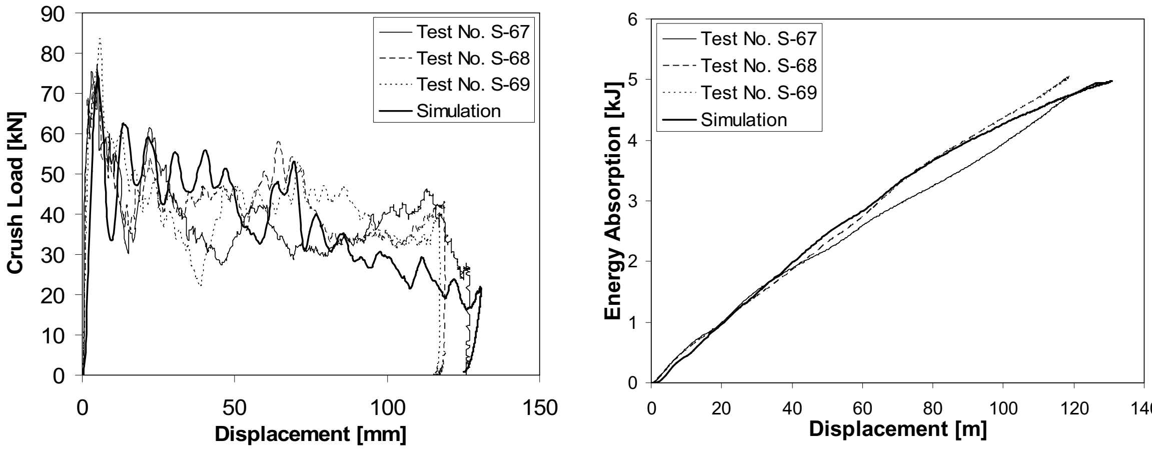

Figure 6.12: Comparison between experimental and numerical (multi layers method) crush load-displacement curves (left) and energy absorption-displacement curves (right) of square composite tubes

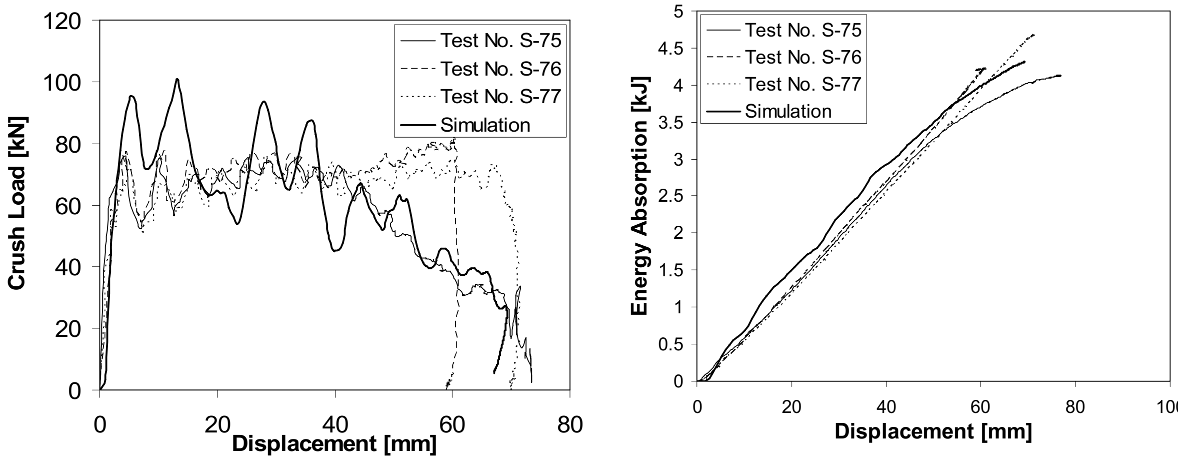

Figure 6.13: Comparison between experimental and numerical (multi layers method) crush load-displacement curves (left) and energy absorption-displacement curves (right) of hexagonal composite tubes

6.4 Multi design optimization of crush behavior of square composite crash box

There are high interests to find the effect of composite tube geometry on its energy absorption capability. Generally, variation in tube geometry influences the fracture mechanisms and, therefore, the energy absorption capability. Thornton and Edwards (1982) [108] investigated the crush performance of square, rectangular and circular composite tubes. They concluded that for a given fiber lay up and tube geometry, circular tubes have the highest specific energy absorption followed by square and rectangular tubes. Farley (1986) [27] investigated the effect of geometry on the energy absorption capability of the composite tubes. He conducted a series of quasi-static crash tests of Graphite/Epoxy and Kevlar/Epoxy composite tubes with the ply orientation of ±45 degree. He found that the tube diameter to wall thickness ratio *d/t* has significant effects on the energy absorption capability. The energy absorption was found to be a decreasing nonlinear function of tube *d/t* ratio. A reduction in *d/t* ratio increases the specific energy absorption of the tube. Similar result has been reported by Farley and Jones (1992) [28] for elliptical composite tubes.

The implementation of the *MDO* in crashworthiness improvement of aluminum tube was examined previously [125]. Here, the same optimization procedure is used to find optimum composite crash box [131]. The finite element method is used to calculate the absorbed energy and specific absorbed energy of the tubes. The design variables are the tube thickness (number of layers), width and length of the composite tubes. The composite tubes with the thickness between 1 mm and 4 mm are selected while the tube width is varied between 70 mm and 120 mm and the tube length between 100 mm and 350 mm. Here 0.5 mm thickness is considered for each layer of composite tube. To have acceptable crush performance in oblique crash conditions, the tube width lower than 70 mm is not considered. An impact force constraint is usually required to reduce the occupant injury when passenger vehicles are considered. Therefore, in the optimization process, the mean crush load P_m should not exceed the allowable limit P_{ma} i.e.:

$$g= P_m/P_{ma}-1\leq 0. \tag{6-7}$$

Where P_{ma}=68.5 kN is selected in this research. The optimization problem can be rewritten as follows

Maximize energy absorption E and specific energy absorption SEA of tube Subjected to

$$\begin{aligned} &0.5 \text{ mm} \leq t \leq 3.0 \text{ mm}, \\ &100 \text{ mm} \leq l \leq 350 \text{ mm}, \\ &50 \text{ mm} \leq d \leq 120 \text{ mm}, \\ &P_m \leq 68.5 \text{ kN}. \end{aligned} \tag{6-8}$$

The optimization procedure which is presented in section 2.7 is applied to the maximization of absorbed energy and specific absorbed energy of the composite tube under axial impact load. Since the interest is to find the crush behavior of tubes up to the final effective crush length, all tubes are encountered with a large amount of impact energy. Here 75 percent of tube length is considered as effective crush length. In order to reduce the optimization time, the single layer finite element models are used to find the energy absorption of composite tubes in every subproblem and the final optimum tube is modeled as a multi layer composite tube.

Table 6.4 shows the final optimum composite tube that absorbs maximum energy with minimum weight. Here it can be seen that the optimum tube thickness t is 3 mm (N_l=6 layers). The thicker tube will have mean crush load higher than allowable limit. The variable d coincides with the lower bound which shows an increase of the crashworthiness efficiency by reduction of tube width. But here values lower that 70 mm are not allowed to guarantee enough bending resistance of the composite crash box in oblique crash conditions. The tube length coincides with the upper bound but in order to avoid global buckling, longer tubes are not considered. Previously the *MDO* procedure was used to find optimum aluminum tubes. There, to avoid global buckling in the aluminum tubes the maximum allowed tube length to width ratio is set to $l/d\leq 3$ based on experimental observations [61], [39], [40]. In order to compare crashworthiness behavior of the optimum composite and aluminum crash boxes, this new optimization constraint is considered for composite crash tube. Table 6.5 shows the results of optimum composite and aluminum crash boxes. It can be seen that the composite tube absorbs about 17 percent more energy than aluminum crash box while it has about 27 percent lower weight.

Table 6.4: Optimum square composite tube

Tube type	T; N_l [mm; -]	d [mm]	l [mm]	E [J]	SEA [J/kg]
Square composite	3; 6	70	350	15316	35580

Table 6.5: Comparison between optimum composite and optimum aluminum crash boxes

Tube Type	t [mm]	d [mm]	l [mm]	E [J]	Increase [%]	SEA [J/kg]	Increase [%]
Square aluminum	2.1	70	210	7602	-	26124	-
Square composite	3	70	210	9198	17.4	35716	26.9

6.5 Crush performance investigation of foam-filled composite crash box

Here, Alporas aluminum foam with a relative density of 0.085 is used to produce foam filled square composite crash box. Dynamic compression tests were conducted on them. The composite square tubes with the dimensions which previously presented in Figure 6.1 are used. The nominal wall thickness of the composite tubes is 2.4 mm. Dynamic tests were done in drop weight test rig, see Figure 3.5. Simply support boundary conditions were applied for the tubes. Table 6.6 shows the results of experimental tests. The crush pattern of test number (F-37) is shown in the Figure 6.14. Here, similar to empty composite tubes, the tube is split from its corners. In comparison to the empty composite tubes, lower delamination area can be seen. The tube is ruptured from its corners and the foam filler is crushed progressively. Numerical simulations of crash tests are performed using the explicit finite element code LS-DYNA. The new developed finite element model in this study is used to describe the composite square tubes, see section 6.3. The foam filler is modeled with solid elements and rigid body elements are used to model the rigid impactor. The contact between the rigid body and the specimen is modeled using a node to surface algorithm with a friction coefficient of $\mu = 0.2$. To account for self contact between the tube walls during deformation, a single surface contact algorithm is used. The node to surface contact is implemented between tube walls and foam filler. The composite walls are modeled with the use of material model #54 in LS-DYNA The aluminum foam was modeled with the foam model of Dehspande and Fleck (2000) [19] material number #154 in LS-DYNA. Figure 6.15 shows that the predicted energy absorption by the simulation is in good agreement with the experimental one.

Table 6.7 shows a comparison between energy absorption E and specific energy absorption SEA of the empty and foam-filled composite square tubes at the 80 mm crash length. Here, it can be seen that the foam insertion of the composite tube results in higher energy absorption but unlike the aluminum foam-filled tubes, the specific energy absorption in the composite filled tubes is decreased in comparison with empty one. As mentioned in the chapter four, the benefit of using foam inside the crash absorbers is the interaction between foam and crash absorber walls during crush process. But as one can see in the Figure 6.14, in the foam-filled composite tubes, the composite tube is split into four parts and the tube and foam crushed independently. Here no interaction between tube and foam is taken place. From Figure 6.2 it can be seen that the empty composite tubes are split into several parts and each part is splayed into two fronds which spread outwards and inwards. From Figure 6.14 it is clear that the foam filler forced the tube parts outward during the crush process and prevent from splaying of the parts. Therefore no frond is created and delamination between the composite layers, which is one of the main energy absorption sources of the composite, is not taken placed. Therefore, the specific energy absorption of the filled composite tube is lower than empty tubes.

Another interesting result which is extracted from experimental results of dynamic tests on simple foam filler is that the energy absorption of foam filler is about 4950 J at 80 mm crash length. That means the some of the energy absorption of the empty composite tube alone and foam filler alone is higher than energy absorption of the foam-filled composite tube. In other word not only inserted foam plays no positive roll in the crush process of the filled composite crash box but also it has destructive effect.

Table 6.6: Experimental dynamic test on foam filed square composite tube

Test No.	V [m/s]	t [mm]	P_{max} [kN]	P_m [kN]	S_{max} [mm]	E [J]	SEA [J/kg]	η [%]
F-37	10.4	2.4	85.1	46.9	105.4	4994	34006	55.1
F-38	10.3	2.4	95.1	47.3	97.7	4890	35922	49.7
F-39	10.3	2.4	87.8	46.2	108.5	4954	32770	42.6

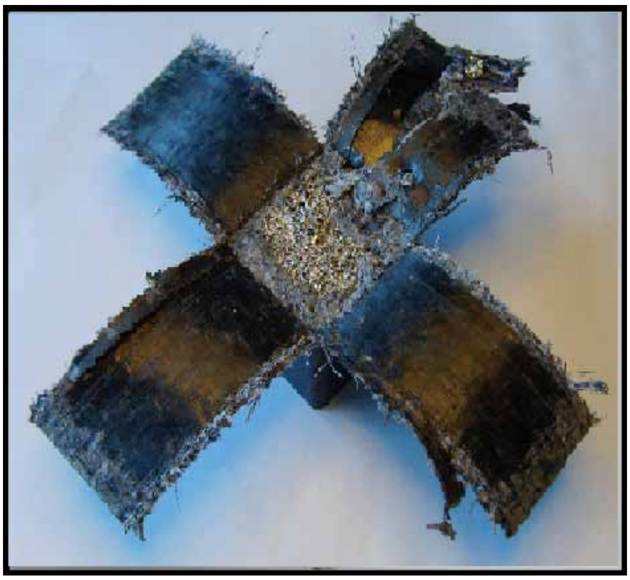

Figure 6.14: Crush pattern of foam-filled composite crash box

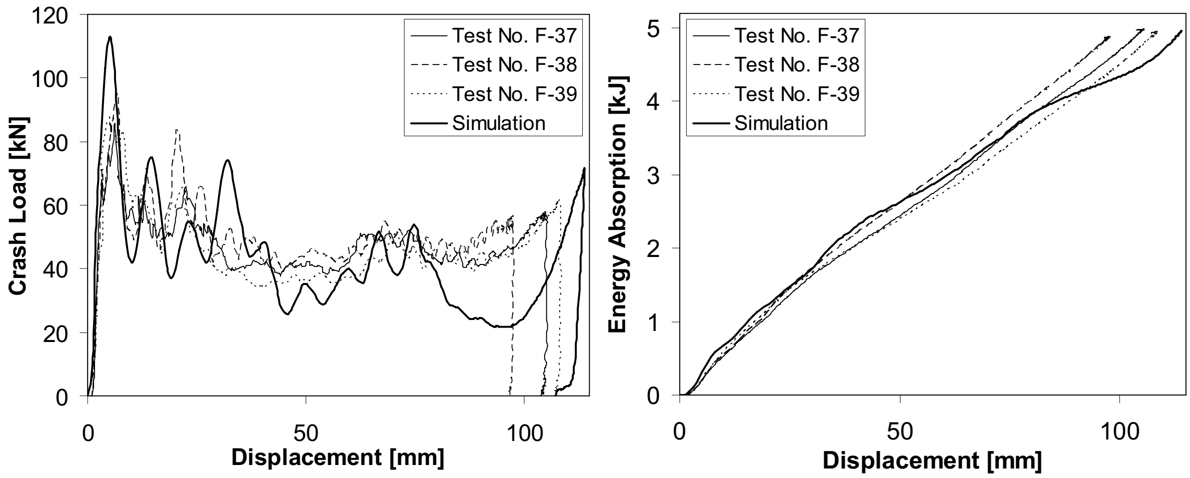

Figure 6.15: Comparison between experimental and numerical (multi layers method) crush load-displacement curves (left) and energy absorption-displacement curves (right) of square composite foam-filled tubes

Table 6.7: Comparison between empty and foam-filled composite tubes

Test No.	Filler type	*E* [J]	Increas e	*SEA* [J/kg]	Increas e
Average of S-67, S-68, S-69	-	3487	-	46701	-
Average of F-37, F-38-F-39	Foam	3832	9.0	34233	-26.7

7. Conclusion

In this study, a full vehicle finite element model was implemented to investigate the crush performance of a vehicle in a frontal crash condition. An optimization procedure was implemented to reduce the weight of the crash elements in such a way that safety requirements are still satisfied.

In order to study the crush performance of the vehicle, here, bumper beam and crash box were selected for a detailed study because of their high energy absorption capacity and high effective crush performance. Since normally aluminum tubes and beams are used as crash box and bumper beam in the vehicle's structure, experimental crash tests were done to investigate the crush performance of aluminum tubes under axial and oblique crush loads and aluminum beams under bending crush load. The finite element explicit crash code, LS-DYNA, was used to find more information about the crush process which can not be measured during the crash tests. In order to characterize the crush behavior of aluminum tubes and beams, the energy absorption *E* and specific energy absorption *SEA,* which is the energy absorption per crushed mass, were considered. The multi design optimization *MDO* procedure was implemented to find optimum tube and beam geometries that absorb the most energy while have maximum *SEA*.

For light weight crash box or bumper beam designs, low density metal fillers, such as aluminum honeycomb or foam, are superior to tubes and beams with thicker walls in terms of achieving the same energy absorption. Experimentally and numerically the crush response of honeycomb and foam-filled aluminum tubes under axial and oblique crash conditions and foam-filled beams under bending load were determined. The crush results showed that filler gives additional support to the tubes and beams and cause higher energy absorption and specific energy absorption in comparison with empty ones. Therefore, a study was performed to find the optimum foam-filled tube under axial crush load and beam under bending crush load which have maximum specific energy absorption and can absorb the same energy as the optimum empty ones. The result of the tube optimization showed that the foam-filled tube under axial crush load absorbs the same energy as the optimum empty tube but it has more than 19 percent higher *SEA*. The result of optimization of foam-filled beam under bending load showed that the optimum filled beam absorbs the same energy as the optimum empty tube but it has more than 28 percent higher *SEA*.

The existing analytical formulations for predicting the crush performance of the empty and filled tubes and beams under axial and bending crush loads were summarized. The experimental results were used to calibrate these expressions. These calibrated formulations can be used in the first design phase of the vehicle crash elements.

Experimental crash tests on square and hexagonal composite crash boxes showed that unlike metallic crash boxes which are crushed in a progressive buckling manner, the composite tubes are crushed in a progressive damaging manner. A new multi layer finite element model was developed to simulate the crush process of the composite crash box. The *MDO* procedure was used to find an optimum design of the composite crash box. The comparison between crashworthiness behavior of the optimum composite and aluminum crash boxes showed that the composite crash box absorbs about 17 percent more energy than the aluminum crash box while it has about 27 percent higher *SEA*. The crush performance of foam-filled square composite crash box was investigated experimentally and numerically. The results showed that the foam insertion results in higher energy absorption but unlike the aluminum foam-filled tubes, the specific energy absorption of the composite filled tubes is decreased in comparison with empty one.

One of the main results of this study was the development and implemention of a systematic numerical method which can be used to optimize vehicle crush behavior in frontal crash.

The other main result was to use a combination of experimental, numerical and analytical methods in order to investigate the crush behavior of vehicle crash box and bumper beam. Here, the experimental results were used as a reference point to validate the numerical simulations. Numerical simulations were used to find detailed information about the crush processes which are difficult to measure. Also the validated numerical simulation was used as a tool in the optimization procedure. Optimization of vehicle crash structures is not a new issue, but in this study with the use of a multi design optimization procedure, the energy absorption and specific energy absorption of the crash box and bumper beam were maximized simultaneously.

Using metal fillers does not always improve the crashworthiness behavior of structures. It has been shown that a correct selection of structure and filler is necessary in order to achive good crush performance. Therefore, the optimization procedure was implemented to optimize the crush performance of the filled crash box and bumper beam.

A new interesting method which was used in this study is to use calibrated analytical formulations which predict the crush behavior of the foams and apply them to estimate the needed foam material properties. Otherwise the mechanical properties of the foams had to be determined though experimental procedure. This estimation method was very helpful in the optimization of the filled structure where the foam density was an optimization parameter.

One other main result of this work was the investigation of the crush performance of the composite crash boxes and comparison of their energy absorption mechanisms with those of aluminum crash boxes. A comparison between optimum composite and aluminum crash boxes was also given.

With this research a versatile tool was created for the development of optimized frontal vehicle structure elements with different materials. It can be used from the first design phase using analytical expressions to final optimization phase using numerical optimization.

8. References

[1] Abramowicz, W.: The effective crushing distance in axially compressed thin–walled metal columns. Int. J. Impact. Engng. 1 (1983), pp. 309-317

[2] Abromowicz, W.; Jones, N.: Dynamic axial crushing of square tubes. Int. J. Impact Engng. 2 (1984), pp. 179-208

[3] Abramowicz, W.; Jones, N.: Transition from initial global bending to progressive buckling of tubes loaded statically and dynamically. Int. J. Impact Engng. 19 (1997), pp. 415–437

[4] Abramowicz, W.; Wierzbicki, T.: Axial crushing of multicorner sheet metal columns. J. Appl. Mech. 56 (1989), pp. 113–120

[5] Abramowicz, W.; Wierzbicki, T.: Axial crushing of foam-filled columns. Int. J. Mech. Sci. 34 (1988), pp. 263-271

[6] Akiyama, S.; Ueno, H.; Imagawa, K.; Kitahara, A.; Nagata, S.; Morimoto, K.; Nishikawa, T.; Itoh, M.: Foamed metal and method of producing same. US Patent 4,713,277, 1987

[7] Akkerman, A.; Thyagarajan, R.; Stander, N.; Burger, M.; Kuhn, R.; Rajic, H.: Shape optimization for crashworthiness design using response surfaces. Proceedings of the International Workshop on Multidisciplinary Design Optimization, Pretoria, South Africa (2000), pp. 270-279

[8] Alexander, J.M.: An approximate analysis of the collapse of thin cylindrical shells under axial loading. Quart. J. Mech. appl. Math. 13 (1960), pp. 10-15

[9] Andrews, K.R.F.; England, G.L.; Omani, E.: Classification of the axial collapse of cylindrical tubes under quasi-static loading. Int. J. Mech. Sci. 25 (1983), pp.687-696

[10] Ashby, M.F.; Evans, A.G.; Hutchinson, J.W.; Fleck, N.A.: Metal foams: A design guide. Version 4, Cambridge University Engineering Department, Cambridge, UK, 1998

[11] ASTM D1621-04a, Standard test method for compressive properties of rigid cellular plastics, 2004

[12] Banhart, J.; Baumeister, J.: Production methods for metallic foams. Materials Research Society Symposium Proceedings, on Porous and Cellular Materials for Structural Applications, Spring Meeting, San Francisco, CA, April 13-15, Materials Research

Society, Warrendale, PA (1998), pp. 121-132

[13] Banhart, J.; Baumeister, J.; Weber, M.: Powder metallurgical technology for the production of metal foam. Proceedings of the European Conference on Advanced PM Materials, Birmingham (1995), pp. 201-208

[14] Berstad, T.; Langseth, M.; Hopperstad, O.S.: Crashworthiness of aluminum extrusions: validation of numerical simulation, effect of mass ratio and impact velocity - Effect of inertia and elasticity. Int. J. Impact Engng. 22 (1999), pp. 829-854

[15] Bisagni, C.; Pietro, G.D.; Fraschini, L.; Terletti, D.: Progressive crushing of fiber-reinforced composite structural components of a formula one racing car. Comp. Struc. 68 (2005), pp. 491-503

[16] Chang, F.K.; Chang, K.Y.: Post-failure analysis of bolted composite joints in tension and shear-out mode failure. J. Comp. Mat. 21 (1987), pp. 809–833

[17] Chen, W.; Wierzbicki, T.; Santosa, S.: Bending collapse of thin-walled beams with ultralight filler: Numerical simulation and weight optimization. Acta Mech. 153 (2002), pp. 183-206

[18] Craig, K.J.; Stander, N.; Dooge, D.A.; Varadappa, S.: MDO of automotive vehicle for crashworthiness and NVH using response surface methods. AIAA Paper 2002-5607, 9th AIAA/ISSMO Symposium on Multidisciplinary Analysis and Optimization, Atlanta (2002), pp. 1930-1940

[19] Dehspande, V.S.; Fleck, N.A.: Isotropic models for metallic foams. J. Mech. Phys. Solids 48 (2000), pp. 1253-1283

[20] El-Hagel, H.; Mallick, P.K.; Zamani, N.: Numerical modeling of quasi-static axial crush of square aluminum-composite hybrid tubes. Int. J. Crash. 9 (2004), pp. 653-664

[21] Eskandarian, A.; Marzougui, D.; Bedewi, N.E.: Finite element model and validation of a surrogate crash test vehicle for impact with roadside objects. Int. J. Crash. 3 (1997), pp. 239-257

[22] Etman, L.F.P.: Optimization of multibody systems using approximation concepts. Ph.D. Thesis, Technical University Eindhoven, The Netherlands, 1997

[23] Etman, L.F.P.; Adriaens, J.M.T.A.; Van Slagmaat, M.T.P.; Schoofs, A.J.G.: Crashworthiness design optimization using multipoint sequential linear programming. Struc. Optim. 12 (1996), pp. 222-228

[24] Farley, G.L.: Energy absorption of composite materials. J. Comp. Mat. 17 (1983), pp. 267-279

[25] Farley, G.L.: The effects of crushing speed on the energy absorption capability of composite tubes. J. Comp. Mat. 25 (1991), pp. 1314-1329

[26] Farley, G.L.; Jones, R.M.: Prediction of the Energy absorption capability of composite tubes. J. Comp. Mat. 26 (1992), pp. 388–404

[27] Farley, G.L.: Effect of specimen geometry on the energy absorption capability of composite tubes. J. Comp. Mat. 20 (1986), pp. 390–400

[28] Farley, G.L.; Jones, R.M.: Crushing characteristics of composite tubes with near elliptical cross sections. J. Comp. Mat. 26 (1992), pp. 1741–1751

[29] Feillard, P.: Crush modeling of automotive structural parts made of composite materials. SAE Transactions: J. Mat. Manufacturing 108 (1999), pp. 200-208

[30] Fleming, D.C.; Vizzini, A.J.: Off-axis energy absorption characteristics of composites for crashworthy rotorcraft design. J. American Helicopter Society 41 (1996), pp. 239–246

[31] Fleming, D.C.: Delamination modeling of composite for improved crash analysis. J. Comp. Mat. 35 (2001), pp. 1777-1792

[32] Gadd, C.M.: Use of a weighted impulse criterion for estimating injury hazard. Proceedings of the 10th Stapp Car Crash Confrence, Society of Automotive Engineers, New York NY, pp. 164-174 (1966)

[33] Gibson, L.J.; Ashby, M.F.: Cellular solids: Structure and properties. Cambridge University Press, 2000

[34] Gu, L.: A comparison of polynomial based regression models in vehicle safety analysis. Proceedings of DETC'01 ASME 2001 Design Engineering Technical Engineering Conferences and the Computers and Information in Engineering Conference, Paper DETC2001/DAC-21063, Pittsburgh, PA (2001)

[35] Guillow, S.R.; Lu, G.; Grzebieta, R.H.: Quasi-static axial compression of thin-walled circular aluminum tubes. Int. J. Mech. Sci. 435 (2001), pp. 2103-2123

[36] Hallquist, J.O.: LS-DYNA Keyword User's Manual, Version 970, Livermore Software Technology Corporation, 2003

[37] Hallquist, J.O.: LS-DYNA Theoritical Manual, Livermore Software Technology Corporation, 1998

[38] Hamada, H.; Ramakrishna, S.A.: A FEM method for prediction of energy absorption capability of crashworthy polymer composite materials. J. Reinforced Plastic. Comp. 16 (1997), pp. 226-242

[39] Hanssen, A.G.; Langseth, M.; Hopperstad, O.S.: Static crushing of square aluminum extrusions with aluminum foam filler. Int. J. Mech. Engng. 41(1999), pp. 967-993

[40] Hanssen, A.G.; Langseth, M.; Hopperstad, O.S.: Static and dynamic crushing of square aluminum extrusions with aluminum foam filler. Int. J. Impact Engng. 24 (2000), pp. 347-383

[41] Hanssen, A.G.; Langseth, M.; Hopperstad, O.S.: Optimum design for energy absorption of square aluminum columns with aluminum foam filler. Int. J. Mech. Engng. 43 (2001), pp. 153-176

[42] Hanssen, A.G.; Hopperstad, O.S.; Langseth, M.; Ilstad, H.: Validation of constitutive models applicable to aluminum foams. Int. J. Mech. Sci. 44 (2002), pp. 359-406

[43] Hashin, Z.: Failure criteria for unidirectional fiber composites. J. Appl. Mech. 47 (1980), pp. 329–334

[44] Haug, E.; Fort, O.; Tramecon, A.; Watanabe, M.; Nakada, I.: Numerical crashworthiness simulation of automotive structures and components made of continuous fiber reinforced composite and sandwich assemblies. SAE Technical Paper Series 910152 (1991), pp. 245-258

[45] Holland, J.: Adaption in natural and artificial systems, University of Mochigan,1975

[46] Hörmann, M.; Wacker, M.: Simulation of the crush performance of crash boxes based on advanced thermoplastic composite. Proceedings of the 5th European LS-DYNA Users Conference, Birmingham, UK (2005), pp. 25-26

[47] Hull, D.: Energy absorption of composite materials under crush displacement variables obviates the need for special element types that are not available in crash codes. Proceeding of the 4th International Conference on Composite Materials: Progress in Science and Engineering of Composites held in Tokyo, Japan (1982), pp. 861-887

[48] Injuries in the European Union, Statistics summary 2002–2004, Featuring the EU Injury Database (IDB), 2006

[49] ISO 6892, Metalic materials- Tensile testing at ambient temperature. 1998 (E)

[50] Jacob, G.C.; Simunovic, J.F.S.; Starbruk, J.M.: Energy absorption in polymer composite for automotive crashworthiness. J. Comp. Mat. 36 (2002), pp. 813-850

[51] Johnson, A.F.; Kindervater, C.M.; Kohlgrüber, D.; Lützenburger, M.: Predictive methodologies for the crashworthiness of aircraft structures. Proceedings of the 52nd American Helicopter Society Annual Forum, Washington, DC (1996), pp. 1340–1352

[52] Johnson, A.F.; Kohlgrüber, D.: Modeling the crush response of composite structures. J. Phys. IV France, Colloque C3, Supplement au Journal de Physique III, (in English) 7 (1998), pp. C3-981–C3-986

[53] Kecman, D.: Bending collapse of rectangular and square section tubes Int. J. Mech. Sci. 25 (1983), pp. 623-636

[54] Kerth, S.; Dehn, A.; Ostgathe, M.; Maier, M.: Experimental investigation and numerical simulation of the crush behavior of composite structural parts. Proceedings of the 41st International SAMPE Symposium and Exhibition (1996), pp. 1397–1408

[55] Kindervater, C.M.: Crush resistant composite helicopter structural concepts thermoset and thermoplastic corrugated web designs. Proceedings of the American Helicopter Society, National Technical Specialists Meeting on Advanced Rotorcraft Structures, Williamsburg, VA (1995)

[56] Kohlgrüber, D.; Kamoulakos, A.: Validation of numerical simulation of composite helicopter subfloor structures under crush loading. Proceedings of the 54th American Helicopter Society Annual Forum, Washington DC (1998), pp. 340-349

[57] Koshal, R.S.: Application of the method of maximum likelihood to the improvement of curve fitting by the method of moments. J. Roy. Statistical Soc. Series A 96 (1993), pp. 303–313

[58] Kröger, M.: Methodische Auslegung und Erprobung von Fahrzeug Crash Strukturen. Ph.D Theses, Institute of Mechanics, University of Hannover, Germany, 2002

[59] Kröger, M.; Popp, K.: Comparison of the energy absorption by tapering of tubes with other forming processes. 30th ISATA Symposium on Automotive Technology and Automation – Road and Vehicle Safety (1997), pp. 445-452

[60] Langseth, M.; Hopperstad, O.S.; Hanssen, A.G.: Static and dynamic axial crushing of square thin-walled aluminum extrusions. Int. J. Impact Engng. 18 (1996), pp. 949-968

[61] Langseth, M.; Hopperstad, O.S.; Hanssen, A.G.: Crush behavior of thin-walled aluminum members. Thin-walled Struc. 32 (1998), pp. 127-150

[62] Lim, T.J.; Smith, B.; McDowell, D.L.: Behavior of a random hollow sphere metal foam. Acta Mater. 50 (2002), pp. 2867-2879

[63] Magee, C.L.; Thornton, P.H.: Design consideration in energy absorption by structural collapse. Warrendale, PA : Society of Automotive Engineers, 1978

[64] Mahmood, H.F.; Paluszny, A.: Axial collapse of thin wall cylindrical column. Proceeding of the Fifth International Conference on Vehicular Structural Mechanics,

Detroit, SAE Paper No. 840727, 1984

[65] Mahmood, H.F.; Paluszny, A.: Design of thin wall columns for crash energy management - their strength and mode of collapse. SAE Fourth International Conference on Vehicle Structural Mechanics, Paper No.811302 (1981)

[66] Mahmood, H.F.; Paluszny, A.: Stability of plate type box columns under crush loading. Computational Methods in Ground Transportation Vehicles 50 (1982), pp. 17-33

[67] Mallick, P.K.: Fiber reinforced composites. 2nd Edition, New York, Marcel Dekker, 1990

[68] Mamalis, A.G.; Manolakos, D.E.; Demosthenous, G.A.; Ioannidis, M.B.: The static and dynamic axial crumbling of thin-walled fiberglass composite square tubes. Comp. Part B: Engng. 28B (1997), pp. 439-451

[69] Mamalis, A.G.; Manolakos, D.E.; Ioannidis, M.B.; Papapostolou, D.P.: On the response of thin-walled composite tubular components subjected to static and dynamic axial compressive loading: Experimental. Comp. Struc. 69 (2005), pp. 407-420

[70] Mamalis, A.G.; Manolakos, D.E.; Ioannidis, M.B.; Papapostolou, D.P.: The static and dynamic axial collapse of CFRP square tubes: Finite element modeling. Comp. Struc. 74 (2006), pp. 2213-2250

[71] Marklund, P.O.: Optimization of a car body component subjected to impact. Linköping Studies in Science and Technology, Thesis No. 776, Department of Mechanical Engineering, Linköping University, Sweden, 1999

[72] Marklund, P.O.; Nilsson, L.: Optimization of a car body component subjected to side impact. Struc. Multidisc. Optim. 21 (2001), pp. 383-392

[73] Mechanical properties of Hexel honeycomb materials, Hexel cooperation, Dublin, CA., USA, Report No. Revised TSB 120, 1992

[74] Myers, R.H.; Montgomery, D.C.: Response surface methodology. New York: John Wiley & Sons Inc., 1995

[75] Nondifferentiable interactive multiobjective optimization system. http://nimbus.mit.jyu.f-i/info.html, 2007

[76] Otte, D.: Realitätsbezug von Crashbedingungen zu den Situation des realen Unfallgeschehens. Verkehrsunfall und Fahrzeugtechnik 29 (1991), pp. 329-336

[77] Papka, S.D.; Kyriakides, S.: Experiments and full-scale numerical simulations of in-plane crushing of a honeycomb. Acta Mater. 46 (1998), pp. 2765-2776

[78] Du Bois, P.; Chou, C.C.; Fileta, B.B., Khalil, T.B., King, A.I.; Mahmood, H.F.; Mertz, H.J.; Wismans, J.: Vehicle crashworthiness and occupant protection. Automotive Applications Committee, American Iron and Steel Institute, Southfield, Michigan, 2004

[79] Pugsley, A.G.: On the crumpling of thin tubular structures. Quart. J. Mech. appl. Math. 32 (1979), pp. 1-7

[80] Pugsley, A.G.; Macaulay M.R.: Large scale crumpling of thin cylindrical columns. Quart. J. Mech. appl. Math. 13 (1960), pp.1-9

[81] Raid, S.R.; Reddy, T.; Gary, M.D.: Static and dynamic axial crushing of foam-filled sheet metals tubes. Int. J. Mech. Sci. 28 (1986), pp. 285-322

[82] Ramakrishna, S.: Microstructural design of composite materials for crashworthy applications. Mat. Design 18 (1997), pp. 167-173

[83] Rayrs, A.; Hopperstad, O.S.; Hanssen, A.G.; Langseth, M.: Modeling of material failure in foam-based components. Int. J. Impact. Engng. 30 (2004), pp. 805-834

[84] Rechenberg, I.: Evolutionsstrategie: Optimierung technischer Systeme nach Prinzipien der biologischen Evolution. Stuttgart: Fromman-Holzboog, 1973

[85] Redhe, M.; Nilsson, L.: A method to determine structural sensitivities in vehicle crashworthiness design. Int. J. Crash. 7 (2002), pp. 179–190

[86] Redhe, M.; Forsberg, J.; Jansson, T.; Marklund, P.O.; Nilsson, L.: Using the response surface methodology and the D-optimality criterion in crashworthiness related problems –an analysis of the surface approximation error versus the number of function evaluations. Struct. Multidisc. Optim. 24 (2002), pp. 185–194

[87] Redhe, M.; Nilsson, L.: Using space mapping and surrogate models to optimize vehicle crashworthiness design. AIAA-Paper 2002-5536, Proceeding of the 9th AIAA/ISSMO Symposium on Multidisciplinary Analysis and Optimization, Atlanta, Georgia (2002)

[88] Reedy, E.D.; Mello, F.J.; Guess, T.R.: Modeling the initiation and growth of delaminations in composite structures. J. Comp. Mat. 31 (1997), pp. 812–831

[89] Reyes, A.; Langseth, M.; Hopperstad, O.S.: Square aluminum tubes subjected to oblique loading. Int. J. Impact Engng. 28 (2003), pp. 1077-1106

[90] Roux, W.; Stander, N.; Haftka, R.: Response surface approximations for structural optimization. Int. J. Numer. Meth. Engng. 42 (1998), pp. 517–534

[91] Santosa, S.P.; Wierzbicki, T.: Crash behavior of box columns filled with aluminum honeycomb or foam. Comp. Struct. 68 (1998), pp. 343–367

[92] Santosa, S.: Crashworthiness analysis of ultralight metal structures. PhD thesis, Massachusetts Institute of Technology, 1999

[93] Santosa, S.P.; Wierzbicki, T.: Effect of an ultralight metal filler on the bending collapse behavior of thin-walled prismatic columns. Int. J. Mech. Sci. 41 (1999), pp. 995–1019

[94] Santosa, S.P.; Banhart, J.; Wierzbicki, T.: Bending crush resistance of partially foam-filled sections. Advance Engng. Mat. 4 (2000), pp. 223–227

[95] Schramm, U.; Thomas, H.: Crashworthiness design using structural optimization. AIAA Paper 98-4729 (1998)

[96] Schramm, U.; Thomas, H.: Structural optimization in occupant safety and crash analysis. Design Optimization. 1(4) (1999), pp. 374–387

[97] Schramm, U.: Multi-disciplinary optimization for NVH and crashworthiness. Proceeding of the First MIT Conference on Computational Fluid and Solid Mechanics, Boston (2001), pp. 721-724

[98] Schramm, U.: Designing with structural optimization – A practical point of view. AIAA Paper 2002-5191, Proceeding of 9th AIAA/ISSMO Symposium on Multidisciplinary Analysis and Optimization, Atlanta, Georgia (2002)

[99] Shahbeyk, S.; Vafai, A.; Estekanchi, H.E.: A parametric study of the bending crush performance of empty and metal foam-filled box-beams. Int. J. Crash. 9 (2004), pp. 643-652

[100] Shin, K.C.; Lee, J.J.; Kim, K.H.; Song, M.C.; Huh, J.S.: Axial crush and bending collapse of an aluminum/GFRP hybrid square tube and its energy absorption capability. Comp. Struc. 57 (2002), pp. 279-287

[101] Simone, A.E.; Gibson, L.J.: The effects of cell face curvature and corrugations on the stiffness and strength of metallic foams. Acta Mat. 46 (1998), pp. 3929-3935

[102] Singac, A.A.; Elsobky, H.: Further experimental investigation on the eccentricity factor in the progressive crushing of tubes. Int. J. Solids Struc. 32 (1996), pp. 3589-3602

[103] Singace, A.A.: Axial crushing analysis of tubes deforming in the multi-lobe mode. Int. J. Mech. Sci. 41(1999), pp. 865-890

[104] Sobieszczanski-Sobieski, J.; Kodiyalam, S.; Yang, R.J.: Optimization of car body under constraints of noise, vibration, and harshness (NVH) and crash. AIAA Paper 2000-1521 (2000), pp. 295-306

[105] Stander, N.: Optimization of nonlinear dynamic problems using successive linear

approximations. AIAA Paper 2000-4798, 2000

[106] Sugimura, Y.; Meyer, J.; He, M.Y.; Bart-Smith, H.; Grenestedt, J.; Evans, A.G.: On the mechanical performance of closed cell foams. Acta Mater. 45 (1997), pp. 5245-5259

[107] European road statistics, Brussel 2007

[108] Thornton, P.H.; Edwards, P.J.: Energy absorption in composite tubes. J. Comp. Mat. 16 (1982), pp. 521–545

[109] Versace, J.: A review of the severity index. Proceedings of the 15th Stapp Car Crash Conference, Society of Automotive Engineers, New York, NY, pp. 771-796 (1971)

[110] Wierzbiki, T.; Bhat, S.U.: A moving hinge solution for axisymmetric crushing of tubes. Int. J. Mech. Sci. 28 (1986), pp. 135-151

[111] Wierzbiki, T.; Bhat, S.U.; Abramowicz, W.; Brodkin, D.: Alexander revisited - a two folding elements model of progressive crushing of tubes. Int. J. Solids Struc. 29 (1992), pp. 3269-3288

[112] Wierzbicki, T.; Abramowicz, W.: On the crushing mechanics of thin-walled structures. J. Appl. Mech. 50 (1983), pp. 727–734

[113] Wierzbicki, T.; Recke, L.; Abramowicz, W.; Gholami, T.; Huang, J.: Stress profiles in thin-walled prismatic columns subjected to crash loading- II Bending. Comp. Struc. 51 (1994), pp. 625-641

[114] Wierzbicki, T.: Crushing analysis of metal honeycombs. Int. J. Impact Engng. 1 (1983), pp. 157-174

[115] Yamazaki, K.; Han, J.: Maximization of the crushing energy absorption of tubes. Struc. Optim. 16 (1998), pp. 37-49

[116] Yang, R.J.; Wang, N.; Tho, C.H.; Bobineau, J.P.; Wang, B.P.: Metamodeling development for vehicle frontal impact simulation. Proceedings of DETC'01 ASME 2001 Design Engineering Technical Engineering Conferences and the Computers and Information in Engineering Conference, Paper DETC2001/DAC-21062, Pittsburgh, PA (2001)

[117] Yang, R.J.; Gu, L.; Tho, C.H.; Sobieszczanski-Sobieski, J.: Multidisciplinary design optimization of a full vehicle with high performance computing. AIAA Paper 2001-1273 (2001)

[118] Yang, R.J.; Tho, C.H.; Gu, L.: Recent development in multidisciplinary design optimization of vehicle structures. AIAA-paper 2002-5606, Proceeding of 9th AIAA/ISSMO Symposium on Multidisciplinary Analysis and Optimization, Atlanta,

Georgia (2002)

[119] Yang, R.J.; Gu, L.; Fu, Y.; Tho, C.H.: Experience with sequential stochastic design improvement methods. Proceedings of the Second MIT Conference on Computational Fluid and Solid Mechanics, Cambridge (2003)

[120] Zaouk, A.K.; Marzougui, D.; Bedewi, N.E.: Development of a detailed vehicle finite element model, Part I: Methodology. Int. J. Crash. 5 (2000), pp. 25–35

[121] Zaouk, A.K.; Marzougui, D.; Kan, C.D.: Development of a detailed vehicle finite element model, Part II: Material characterization and component testing. Int. J. Crash. 5 (2000), pp. 37–50

[122] Zarei, H.; Kröger, M.; Popp, K.: On the dynamic crash load efficiency of circular aluminum tubes. Proceeding of the 6th European Conference on Structural Dynamics, Paris (2005), pp. 1979-1984

[123] Zarei, H.; Kröger, M.: Experimental and numerical quasi-static crash investigation in empty and honeycomb-filled aluminum square. Int. J. Crash., Submitted for publication

[124] Zarei, H.; Kröger, M.: Crashworthiness optimization of empty and filled aluminum crash boxes. Int. J. Crash. 12 (2007), pp. 255-264

[125] Zarei, H.; Kröger, M.: Multiobjective crashworthiness optimization of circular aluminum tubes. Thin-Walled Struc. J. 44 (2006), pp. 301-308

[126] Zarei, H.; Kröger, M.: Optimum honeycomb-filled crash absorber design. J. Mat. Design 29 (2008), pp. 193-204

[127] Zarei, H.; Kröger, M.: Optimisation of the foam-filled tubes for crash box application. Thin-Walled Struc. J. 46 (2008), pp. 214-221

[128] Zarei, H.; Kröger, M.: Bending behavior of empty and foam-filled beams: Structural optimization. Int. J. Impact Engng. 35 (2008), pp. 521-529

[129] Zarei, H.; Kröger, M.; Albertsen, H.: Crashworthiness investigation of the composite thermoplastic crash box. Proceeding of the Sixth Canadian-International Composites Conference, Winnipeg 14-17 August (2007), pp. 1-14

[130] Zarei, H.; Kröger, M.; Albertsen, H.: An experimental and numerical crashworthiness investigation of the thermoplastic composite crash boxes. Comp. struc. J., In press 2007

[131] Zarei, H.; Kröger, M.; Albertsen, H.: Optimum composite thermoplastic crash box. Proceeding of the Sixth Canadian-International Composites Conference, Winnipeg 14-17 August (2007), pp. 1-13